Developing Piezoelectric Biosensing Methods

Ming-Liang Lai

Submitted in fulfilment of the requirements for the Degree of Doctor of Philosophy in Engineering

School of Engineering

College of Science and Engineering

University of Glasgow

Abstract

Biosensors are often used to detect biochemical species either in the body or from collected samples with high sensitivity and specificity. Those based on piezoelectric sensing methods employ mechanically induced changes to generate an electrical response. Reliable collection and processing of these signals is an important aspect in the design of these systems. To generate the electrical response, specific recognition layers are arranged on piezoelectric substrates in such a way that they interact with target species and so change the properties of the device surface (e.g. the mass or mechanical strain). These changes generate a change in the electrical signal output allowing the device to be used as a biosensor. The characteristics of piezoelectric biosensors are that they are competitively priced, inherently rugged, very sensitive, and intrinsically reliable. In this study, a compound label-free biosensor was developed. This sensor consists of two elements: a Love wave sensor and an electrochemical impedance sensor. The novelty of this device is that it can work in both dry and wet measurement conditions. Whilst the Love wave sensor aspect of the device is sensitive to the mass of adsorbed analytes under both dry and wet conditions with high sensitivity, the sensitivity coefficients in these two conditions may be different due to the different (mechanical) strengths of interaction between the adsorbed analyte and the substrate. The impedance sensor element of the device however is less sensitive to the mechanical strength of the bond between the analyte and the sensing surface and so can be used for in-situ calibration of the number of molecules bound to the sensing surface (with either a strong or weak link): conventional Love wave sensors are not sensitive to material loosely bound to the surface. Thus, a combination of results from these two sensors can provide more information about the analyte and the accuracy of the Love wave sensor measurements in a liquid environment. The device functions with label-free molecules and so special reagents are not needed when carrying out measurements. In addition, the fabrication of the device is not too complicated and it is

easy to miniaturise. This may make the system suitable for point-of-care diagnostics and bio-material detection.

The substrate used in these sensors is 64°Y–X lithium niobate ($LiNbO_3$) which is a kind of piezoelectric material. On the substrate, there is a pair of interdigital transducers (IDTs) which are composed of 100 Ti/Au split-finger pairs with a periodicity (λ) of 40μm. The acoustic path length, between both IDTs, is 200λ and the aperture between the IDTs is 100λ. On top of the substrate and IDTs, there is a PMMA guiding layer with an optimised thickness ranging from 1000 nm to 1300 nm. In addition, a gold layer with thickness 100 nm is deposited on the guiding layer to act as the electrodes for the electrochemical impedance sensor.

The biosensor in this study has been used to measure Protein A, IgG, and GABA molecules.

Protein A is often coupled to other molecules such as a fluorescent dye, enzymes, biotin, and colloidal gold or radioactive iodine without affecting the antibody binding site. In addition, the capacity of Protein A to bind antibodies with such high affinity is the driving motivation for its industrial scale use in biologic pharmaceuticals. Therefore, measuring Protein A binding is a useful method with which to verify the function of the biosensor.

IgG is the most abundant antibody isotype found in the circulation. By binding many kinds of pathogens including viruses, bacteria, and fungi, IgG protects the body from infection. Also, IgG can bind with Protein A well so the biosensor here could also measure IgG after a Protein A layer is immobilised on the sensing area.

GABA is the main inhibitory neurotransmitter in the mammalian central nervous system. It plays an important role in regulating neuronal excitability throughout the

nervous system. The conventional method to measure concentrations of GABA under the extracellular conditions is by using liquid chromatography. However, the disadvantages of chromatographic methods are baseline drift and additions of solvent and internal standards. Therefore, it is necessary to develop a simple, rapid and reliable method for direct measurement of GABA, and the sensor here is an attractive choice.

When the Love wave sensor works in the liquid media, it can only be used to measure the mass of analytes but does not provide information about the conditions of molecules bound with the sensing surface. In contrast, electrochemical impedance sensing based on the diffusion of redox species to the underlying metal electrode can provide real-time monitoring of the surface coverage of bound macromolecular analytes regardless of the mechanical strength of the analyte-substrate bond: the electrochemical impedance measurement is sensitive to the size and extent of the diffusion pathways around the adsorbed macromolecules used by the redox species probe i.e. it is sensitive to the physical area of the surface covered by the macromolecular analyte and not to the mass of material that is sensed through a mechanical coupling effect (as in a Love wave device). Although electrochemical impedance measurements under the dry state are quite common when studying batteries and their redox/discharge properties, these are quite different sorts of systems to the device in this study. Therefore, integrating these two sensors (Love wave sensor and electrochemical impedance sensor) in a single device is a novel concept and should lead to better analytical performance than when each is used on their own. The new type of biosensor developed here therefore has the potential to measure analytes with greater accuracy, higher sensitivity and a lower limit of detection than found when using either a single Love wave sensor or electrochemical impedance sensor alone.

Key words: biosensor, Love wave sensor, impedance sensor, piezoelectric sensing, label-free, IDTs, Protein A, IgG, Anti-GABA, GABA.

Table of Content

List of Tables

List of Figures

Author’s Declaration

I declare that the work presented in this thesis is entirely my own with all exceptions being clearly indicated or/and properly cited in the context, and all citations have been provided in the reference list.

Signature: Ming-Liang Lai

Abbreviations

SAW	surface acoustic wave
IDTs	interdigital transducers
IgG	immunoglobulin G
GABA	gamma-Aminobutyric acid
PMMA	Polymethylmethacrylate
MIR	mid-infrared
NIR	near- infrared
QCM	quartz crystal microbalance
SPR	surface plasma resonance
FET	field effect transistor
RI	refractive index
IF	intermediate frequency
RF	radio frequency
FITC	fluorescein isothiocyanate
RITC	rhodamine isothiocyanate
SSBW	surface skimming bulk wave
STW	surface transverse wave
SH-SAW	shear horizontal surface acoustic wave
CMOS	complementary metal-oxide-semiconductor
TCD	coefficient of delay
LSAW	leaky surface acoustic wave
PSAW	pseudo surface acoustic wave
ADC	Analog-to-digital converter
DSP	digital signal processing
S-parameters	scattering parameters
Y-parameters	admittance parameters
Z-parameters	impedance parameters
H-parameters	hybrid parameters
ABCD matrix	Ray transfer matrix
DUT	device under test
TRL	thru-reflect-line
LCD	liquid crystal display
VUV	vacuum ultraviolet
MMR	measles, mumps, and rubella
PBS	phosphate buffered saline
D.I. water	deionized water
λ	wave length

Hz	hertz
MHz	mega hertz
KHz	kilo hertz
mm	millimetre
µm	micrometre
nm	nanometre
µg	microgram
ng	nanogram
pg	picogram
mV	millivolt
ml	millilitre

Acknowledgement

First of all, I would like to express my highest gratitude to my supervisors Professor Jonathan Cooper and Dr. Andrew Glidle for their support and guidance from the initial to the final level in my course of study. I truthfully appreciate the opportunity to participate in this interesting and challenging project. I still remember in September 2010, the first time I visited University of Glasgow, I actually couldn't expect what is waiting for me for the next several years at that time. Without Jon and Andrew, I have no idea how I can reach this final stage of my PhD. Sincerely from the bottom of my heart, thank you very much.

I would like to thank both Dr. Rab Wilson and Dr. Julien Reboud, who have greatly contributed to my thesis. This work would not be attainable without the acoustics studies and biochemical experiments they carried out. To Dr. Yi Zhang and Dr. Yannyk Bourquin, thank you for sharing scientific knowledge and discussing projects with me. I would also like to thank people who work in the Rankine building and James Watt Nanofabrication Centre (JWNC) with me: David Gourlay and Thomas Reilly for the technical support in operating instruments in the clean room and provide smart suggestions for my thesis. I am also grateful to the Ministry of Education Taiwan for providing the opportunity, funds and support for this study.

Finally, I will deeply appreciate my parents, sister, and brother for encouraging and support me in the past years. I am particularly grateful to my wife and son. Thank you for your unconditional love and accompany me when I am in the hard time during my study.

Chapter 1 Introduction

1.1 The classification of biosensors

Biosensors can be used to detect biochemical signals in the body with high sensitivity and specificity. In 2013, Ngoepe *et al.* illustrated the functions of biosensors in detail [1] and their report is cited in this thesis. Biosensors can provide a powerful opportunity in early diagnosis and treatment of illness. Early detection and diagnosis can greatly reduce the cost of patient's medical care, associated with advanced stages of many diseases and far better can prevent a disease before it becomes a serious problem. From a diagnostics view point, accuracy of the diagnosis is vital in terms of the kind of therapy to be used. The major concern in diagnosis is patient compliance where invasive samples (blood and tissue) are routinely taken to analyse the severity of the disease. Prognosis only can estimate the probable result of a single patience's disease, so there are limitations in general treatments. Both these affect disease management since dosage and period of treatment influence the level of disease, patient compliance and medical costs. Therefore, for chronic disease, continuous medical intervention is required to allow changing of the dosage and treatment period. This may evidently be observed in diabetes management where treating hyperglycemia can lead to hypoglycemia. Imbalances of glucose and cholesterol are a major concern because these two elements are the major reasons of fatal diseases. Glucose imbalance causes diabetes, which increases the risk of heart diseases, kidney failure, and/or blindness [2]. Both, high and low levels of glucose can result in disability or death. From the diagnosis and management point of view, diabetes mellitus requires a continuous monitoring of blood glucose levels. In 2012 glucose biosensors accounted for approximately 85% of the world market for biosensors [3]. Millions of people who suffer from diabetics test their blood glucose levels daily, thus making glucose the most commonly tested analyte. In 1962, the research group of Clark and Lyons [4] invented the first biosensor which successfully detected the glucose levels of the blood. This journal

paper indicated that glucose oxidase enzyme was entrapped on an oxygen electrode over a semi-permeable dialysis membrane. Glucose levels were indirectly measured by monitoring the amount of oxygen consumed by the enzyme. In 1973, Guilbault and Lubrano designed an amperometric (anodic) sensor to monitor the hydrogen peroxide, a glucose degradation byproduct [5].

Prior to any major impacts, an illness can lead to serious problems to the patient such as neuropathy or retinopathy in terms of diabetes because there are a number of physiochemical changes which occur. Diabetic retinopathy which occurs due to low sugar levels in the eyes can cause blindness as the new capillaries that deliver blood to the eye are frail [6]. For cholesterol, there are a variety of physiochemical changes that take place before signifying future damage. The occurrence of stroke is usually due to blood clogging that causes the interference of blood flow near the nervous system. Prognosis of any illness plays a main role in illness management. However, through the process of diagnosis, chronic illnesses will require continuous monitoring for efficient management. The costs and patients compliance are highly affected by these processes. It is observed that self-monitoring of sugar levels has benefited patients in terms of costs and disease management. Design of self-monitoring devices for glucose levels such as SensoCard Plus (BBI Healthcare) and AccuCheck Compact (Roche) has assisted patients to monitor their glucose concentrations in order to delay or even prevent the progression of microvascular and macrovascular complications [7]. If patients feel comfortable to monitor analyte concentration daily and the processes of monitor are convenient, the patients' willingness to conduct self-monitoring will increase substantially. For a better illness management, non-invasive/continuous sampling is required for optimum medical intervention. There are different kinds of glucose sensors which can be divided into two groups; enzymatic (finger-prick glucometer and urine dipstick), and continuous (non-invasive, minimally invasive and invasive). For continuous invasive sensors, these can be intravenous,

implantable, microdialysis (glucose oxidase electrochemical sensor) and subcutaneous sensors (enzyme electrodes-redox reaction analysis), while for minimally invasive ones, micropore or microneedle (collection of interstitial fluid for enzyme based electrode sensor) can be used [8].

For cholesterol monitoring, it has been shown that accumulative treatment discontinuations among long-term regimens of all types of drugs is about 50% of patients during first year and 85% of patients in the second year of treatment [9]. Similar to diabetes, cholesterol is detected by means of using immobilized enzymes (CholesTrak® , AccuTech, LLC). The enzyme cholesterol oxidase breaks down cholesterol into hydrogen peroxide and cholest-4-en-3-one in the presence of oxygen [10]. The level of cholesterol is then measured by an amperometric sensor that can detect hydrogen peroxide through redox mediator [11]. The methods that utilise enzymes for detection of any analyte have disadvantages such as short lifetime and lower sensitivity. This can be avoided by using two or more enzymes. In the case of cholesterol, cholesterol oxidase and cholesterol esterase can be used in combination [12]. Future cholesterol monitoring devices may include non-invasive mode of cholesterol level detection as in quantifying the levels of isoprene in human breath [13].

For non-invasive sensors the mode of detection can be either optical or via transdermal analysis. For transdermal analysis, impedance spectroscopy (dielectric properties of a tissue), skin suction blister technique (vacuum application on the skin to obtain fluid for analysis), reverse iontophoresis (low electric current application) and sonophoresis (use ultrasound on the skin) may be used [14, 15]. For optical analysis the following methods may be employed; kromoscopy (electromagnetic radiation), photoacoustic spectroscopy (increased ultrasound pulse generated during absorption of light when there is high glucose levels), optical coherence tomography (tomographic imaging), scattering (relative refractive indices of a particle), occlusion spectroscopy

(produce high systolic pressure to occlusion of arterial flow), polarimetry (substances which can rotate the plane of polarized light), thermal infrared (glucose concentration correlates to temperature variation and mid-infrared, MIR, light scattering on the skin), fluorescence (light emission from molecules in different states), MIR spectroscopy (wavelength variations due to stretching and bending of molecules), near-infrared (NIR) spectroscopy (absorption based on molecular structure) and Raman spectroscopy (rotational or vibrational energy states within a molecule) [16].

Biosensors are of interest within the field of modern analytical chemistry and pharmaceutics. There are many published journal papers which displayed the diversity of approaches and techniques applied. This is due to new demands and opportunities that are appearing particularly in clinical diagnostics, environmental analysis, food analysis and production monitoring [17-19]. A biosensor can be defined as a device which can generate a signal that is proportional to the concentration of a particular biomaterial or chemicals in the presence of a number of interfering species [20]. This is accomplished by means of utilising biological recognition elements such as enzymes, antibodies, receptors, tissues and microorganisms as sensitive materials because of their selective functionality for target analytes. To develop a universal biosensor is very difficult, because it is impossible to discover an all-inclusive parameter estimation algorithm that would provide as much as information about material properties in all applications. Each application requires a unique choice of sensor design and associated parameter estimation algorithms. As a sensor system develops, the requirements for each element become clearer and affect the requirements for each element of the trinity displayed in figure 1.1. Sensors can be divided into various groups based on the mode of function in terms of sensing region and transduction.

There are many classifications for biosensors. In the following sections, different types of biosensors are described in turn, according to the type of physical transduction

given in table 1.1. There are six main kinds of physical transductions: optical, thermal, mass, surface acoustic wave, conductance, and impedance.

Table 1.1 Groups of biosensors based on transduction signal, their mode of detection and applications.

Transduction	Mode of Detection	Application
Optical	Surface Plasmon Resonance: immobilizes antibodies/ ligands/ receptors. The analyte concentration is measured upon adsorption	Hand held refract meter (Rhino Series, Reichert, Inc., USA). Detect analytes in urine
	Image-based method: fluorescence is generated with chemical, enzymatic and cellular changes by means of probing	Fluorescence Resonance Energy Transfer-Protein and nucleic acid analysis (Invitrogen, USA)
Thermal	Calorimetric: measures a change in temperature in the solution containing specific analyte and converts it into concentration	Auto-iTC$_{200}$ system (GE Healthcare, USA) and DSC used for characterizing molecular interactions/ enzyme kinetics
Mass sensitive	Quartz crystal microbalance: consists of a thin quartz disk with electrodes plated on it. Measures a mass per unit area by measuring the change in frequency of a quartz crystal resonator	QCM200, Stanford Research Systems, Inc., USA; Attana Cell 200. Measure specific analyte concentration
Surface acoustic wave	Surface acoustic wave: generate and detect acoustic waves using inter-digital transducers. This will detect changes on the surface, such as mass loading, viscosity and conductivity changes	VaporLab, Microsensor Systems, USA. Gas analysis on film swelling results in electrical signal. Breath analysis of volatiles
Conductance	Conductive properties of medium between two electrodes (ionic strength changes)	Enzymatic reactions yielding charged substances. Enzyme field-effect transistor (EnFET); Nanowires
Impedance	Measure both resistance and reactance (change from weak or non-charge substances to highly charged)	IQ Scientific Instruments, Inc. Field-effect Transistor (FET). Drug effects on cell based ionic signatures.

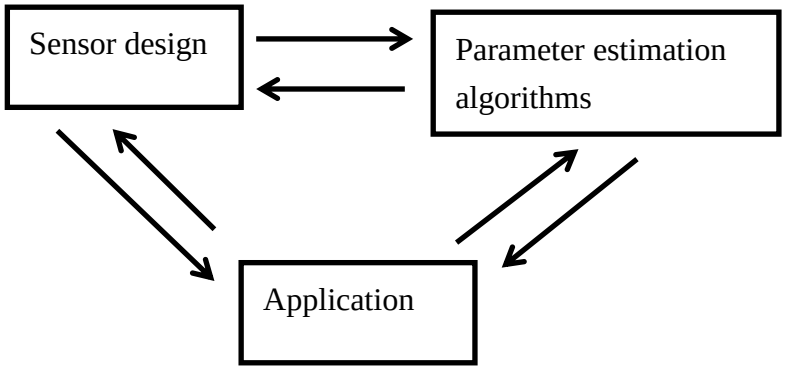

Figure 1.1 Every sensing application requires an optimum combination of inherently dependent elements of the measurement system comprising sensor design and parameter estimation algorithms.

1.1.1 Optical Biosensors

Two major kinds of biosensors using optical transduction method to detect analytes are surface-plasmon resonance (SPR) technology and imaging-based methods.

SPR is a phenomenon which uses visible or near-infrared radiation from a monochromatic light source via a hemispherical prism to irradiate a metallic surface to generate an electromagnetic (optical) evanescent wave. A detector is setup at an angle related to the refractive index (RI). In the evanescent wave, the oscillation of free electrons generates a surface plasmon which can resonate and absorb light. The specific wavelength/angle at which this occurs is a function of the RI in the proximity of the metallic surface and relates to the type and amount of material on the chip surface. A change in this material (e.g. the amount adsorbed, or a mass change) will lead to a refractive index change and a shift in the resonance to a longer wavelength (if the refractive index increases). Such a change in mass can result from the immobilisation of a ligand and, subsequently, further interactions which take place when analytes are passed over the modified sensor surface [21].

A large selection of commercially available SPR optical biosensors can be used for pathogen detection. Wei *et al.* applied the SPREETA™ SPR system (Texas Instruments) to measure *Campylobacter jejuni* [22]. Here, biotinylated leporine polyclonal antibodies were immobilised directly on the sensor surface and the assay had a sensitivity of 1×10^3

CFU/ml. Barlen *et al.* chose the Plasmonic SPR device (Plasmonic Biosensoren) for the detection of *Salmonella typhimurium* and *S. enteritidis* [23]. *Salmonella typhimurium* in milk was also successfully measured by the team of Mazumdar with the same SPR optical biosensor [24]. A range of other optical sensor platforms, including the ProteOn XPR36 (Bio-Rad) and SensíQ (Nomadics) and Biacore™ also have the potential to be applied for pathogen monitoring. Oh *et al.* utilised a SPR-based protein chip assay format with immobilised monoclonal antibodies against *S. typhimurium*, *E. coli* O157:H7, *Yersinia enterocolitica* and *Legionella pneumophila*. 1×10^5 CFU/ml of each pathogen could be specifically measured with their respective antibody [25].

Imaged-based optical biosensors are based on image recognition and technology has been developed which is particularly useful for cancer diagnosis and treatment. There are many problems in traditional methods to diagnose or cure cancer such as surgery, chemotherapy and radiation therapy. There are limitations and disadvantages to these modes of treatments due to the difficulty of getting early diagnoses, nonspecific drug distribution, systemic toxicity and unpredictable pharmacodynamics and pharmacokinetics [47]. When performing an operation, imaging would allow tracing cancer cells that are still localised in the body, and this can even be useful during biopsy investigations. For chemotherapy, carrier functionality would be beneficial as it offers target specificity and controlled drug release. Before the radiation therapies, imaged-based sensor can aid to identify the target region. Nanoparticle imaging would prevent radiation damage from harming other tissues around the target area, thus providing better therapeutic targeting. Targeting and controlled drug release will improve disease management by interfering with disease progression, while the use of biosensors will affect disease diagnosis and prognosis [48]. A fundamental method in some imaged-based sensors is using specific fluorescence molecules to conjugate with target cells or proteins. Then image recognition technology can be used to detect the bright parts in the image.

Aside from the use of conventional fluorescence microscopy, optical imaging based

on bioluminescent bio-reporters carrying the bacterial lux gene cassette has been well established for the sensing and monitoring of select chemical agents. Their ability to generate target specific visible light signals with no requirement for extraneous additions of substrate or other hands-on manipulations affords a real-time, repetitive assaying technique that is remarkable in its simplicity and accuracy. The team of Steven Ripp *et al.* exploited bioluminescent assays for detecting Escherichia coli O157:H7 [40]. Organic dye doped nanoparticles made of silica, poly or PLGA and doped with dyes such as IRG-023 Cy5, fluorescein isothiocyanate (FITC) and rhodamine B isothiocyanate (RITC) can also be used in image-based biosensors. Quantum dots are semiconductor crystals composed of elements from groups II to VI, III to IV or IV to VI from the periodic table while up-conversion nanoparticles are synthesized from LaF_3, YF_3, Y_2O_3, $LaPO_4$, $NaYF_4$ co-doped with trivalent rare earth ions such as Yb_3+, Er_3+ and Tm_3+ [47]. Other groups of imaging biosensors involve multifunctional nanoparticles which can be divided into metallic nanoparticles such as paramagnetic nanoparticles used in cancer therapy, liposome and dendrimers used in cancer and HIV therapy [49].

1.1.2 Thermal biosensors

The working theory of thermal biosensors is to detect the heat from biological reactions. These reactions (which adsorb or evolve heat) cause changes in the temperature within the reaction medium. In earlier studies on calorimetry the change in heat was directly monitored to calculate the extent of reaction or structural dynamics of biomolecules in the dissolved state [21]. With the development of thermometric devices, researchers began to use these devices in the field of biosensors. These predominantly measure the changes in temperature of the circulating fluid following the reaction of a suitable substrate with the immobilized enzyme molecules.

Thermometry basically means measurement of temperature. The essential version of such a device is a thermometer, which is routinely used for measurement of body or

ambient temperature. Based on similar principles, in thermometric devices the heat is measured using sensitive thermistors. Such devices are popularly referred to as an enzyme thermistor. Calorimetric devices for routine use were limited by cost of operation and relatively long experimental procedures. However, the invention of the enzyme thermistor based on flow injection analysis in combination with an immobilized biocatalyst and heat-sensing element, circumvented several of these shortcomings [26].

The thermometric technique has been used to select *Trigonopsis variabilis* strains for high cephalosporin-transforming activity by the team of Gemeiner [27]. Similarly, the cephalosporin-transforming activity of d-amino acid oxidase isolated from yeast was also identified. The adaptation of the thermal biosensor to enzyme linked immunosorbent assay has also been reported by Birnbaum *et al.*, for the determination of hormones, antibodies and other biomolecules generated during the fermentation process [28]. In addition, genetically engineered enzyme conjugates were used for the measurement of insulin or proinsulin with thermal biosensor (Mecklenburg *et al.*, 1993) [30]. Alkaline phosphatase was used as the enzyme label for such studies and the team of Danielsson detected insulin separation with a thermal biosensor [31].

1.1.3 Mass sensitive biosensors

Mass sensitive biosensors operate on the principle that a change in mass, resulting from the bio-molecular interaction (combination between an antibody and its relative antigen) can be determined [21]. A well-known example of mass sensitive biosensor is the micro-cantilever system. By coating a recognition receptor layer over the upper side of a micro-cantilever beam can form a biosensor. Due to its label free detection principle and small size, this type of biosensor has applicable advantages in diagnostic applications, disease monitoring and research in genomics and proteomics [34]. A micro-cantilever biosensor functions by means of transduction of the molecular interaction between analyte and capturing molecule, immobilized as a layer on one surface of a cantilever.

Biomolecular interactions taking place on a solid-state interface leads to a mass increase [35]. This process results in bending of the cantilever. The capturing molecules are immobilized onto the cantilever by means of direct absorption or by means of covalent attachment to the surface modified with functional groups [36]. In the static mode of operation, the sensor response is represented by the beam bending with respect to a reference micro-cantilever. Alternatively, micro-cantilever biosensors can be operated in the dynamic mode. In this case, the beam vibrates at its resonance frequency and a variation in this parameter indicates the concentration of the analyte. Another example to use a micro-cantilever system as biosensor is setting a mesoporous polymer on the device surface. When an analyte of interest enters into the polymer nanopore, analyte particles will block the ion current, resulting in a downward current-pulse. Through this mechanism, analytes detection can be achieved by monitoring the blockage of nanopores before and after an immunological reaction as the current-pulse frequency is proportional to the concentration of the analyte [38].

Another kind of mass sensitive biosensors is quartz crystal microbalance (QCM) system, which mass changes result in alterations in resonance frequency [21]. Quartz is one kind of piezoelectric crystal. The QCM consists of a thin piezoelectric plate with electrodes evaporated onto both sides. Due to the piezoelectric effect, an AC voltage across the electrodes induces a shear deformation and vice versa. The electromechanical coupling provides a simple way to detect an acoustic resonance by electrical means. The electrodes at the front and the back of the crystal usually are key-hole shaped; thereby making the resonator thicker in the centre than at the border, and the overlapping perimeters of the metallic electrodes confines the displacement field to the centre of the crystal by a mechanism called energy trapping. The quartz crystal turns into an acoustic lens and the wave is focused to the centre of the crystal. Altering the thickness of the crystal can change oscillation frequency of QCM. During normal operation, all the other influencing variables remain constant. When mass is deposited on the surface of the crystal, the increased

loading leads to the frequency of oscillation decreasing from the initial value. Therefore, the QCM can be used to investigate interactions between biomolecules by arranging a recognition receptor layer on the surface.

1.1.4 Surface acoustic wave biosensors

Surface acoustic wave (SAW) devices were firstly used as filters and resonators in electronics and communications. Because the acoustic energy of these devices is confined at their surface, SAW devices are sensitive to any changes occurring on the substrate surface, such as mass loading, conductivity, and variations of viscosity [43]. This characteristic has attracted researchers to investigate and develop sensing applications. In the 1980's, researchers tried to use a Rayleigh wave, which is one kind of SAW, to develop biosensors. They could successfully apply it to gas sensing but faced a serious problem when operating these devices in a liquid environment. This is because particle displacements in Rayleigh waves are normal to the surface of the device, which radiates compressional waves into the liquid and causes severe attenuation and high insertion losses. In order to avoid the high damping caused by the aqueous environment, the acoustic waves must be shear horizontally polarized in the liquid. The first successful approaches to use SAW devices sensing in liquid environment were Flory's group and Moriizumi's group, respectively, in 1987 [44]. Their SAW biosensors operated with shear horizontal polarized waves. Nowadays, SAW biosensors can be used to detect proteins, DNA, viruses, bacteria and cells [45].

There are some kinds of SAW suitable to use in biosensing applications which require fluid immersion. One of these types is based on leaky-SAW waves, where the wave is only partially confined to the surface. The leaky-SAW mode is mainly shear horizontal but not purely shear horizontal and consequently suffers extra attenuation under fluid immersion. Another type uses surface transverse waves (STW) which originate from a surface skimming bulk wave (SSBW) that travels very close to the surface but not exactly along it.

A metal strip grating located in the surface of the devices between the input and output IDTs produces a slowing effect on the wave propagation velocity and traps the energy of the wave in the surface of the device enhancing its surface mass sensitivity [44]. Love waves are another kind of shear-horizontal SAW that can be used for biosensing. Love wave devices are comprised of a substrate that primarily excites a SSBW, which is subsequently confined by a thin guiding layer located on the top of the substrate and IDTs. The condition for the existence of Love wave modes is that the shear velocity of the overlay material is less than that of the substrate [46]. The waveguide layer confines the wave energy keeping it near the surface and slowing down the wave propagation velocity. The sensitivity of a sensor is determined by the degree of wave confinement. If the wave is trapped tightly, it will be strongly perturbed by surface changes, yielding high sensitivity. Love wave biosensors can operate efficiently in both gas and liquid media. The parameters that determine the resonance frequency are the spacing of IDTs and the thickness of the wave guiding layer [44].

1.1.5 Conductance biosensors

The concept of designing a conductance biosensor comes from monitoring electrical conductivity changes during biological reactions [21]. There are two major methods to realise conductance measurement. One method is to convert biological signals to electrical signals via a conductive polymer. The team of Hoa applied the method of conductance detection to measure *E. coli* and *Salmonella spp* [32]. A biological signal is successfully converted to an electrical signal via a conductive polymer. The materials of conductive polymer were polyacetylene, polypyrrole, and polyaniline, respectively. Muhammad-Tahir and Alocilja designed a conductance biosensor incorporating a polyclonal antibody-based sandwich assay format in which the detection antibody was labelled with polyaniline. The sensitivity of the sensor could reach to 79 CFU/ml and 83 CFU/ml of *E. coli* O157:H7 and *Salmonella spp.*, respectively.

Another way is to use specific nanoparticles to capture analytes. These were subsequently bound on an electrode. Conductance measurements were facilitated through the application of an alternating-current voltage. Hnaiein *et al.* applied this method to design a conductance immunosensor for *E. coli* [37]. A biotinylated polyclonal antibody was captured on streptavidin-coated magnetite nanoparticles. These were subsequently bound on an electrode through the use of glutaraldehyde coupling. Conductance measurements were facilitated through the application of an alternating-current signal. The incorporation of nanoparticles facilitated an increase in conductivity, enabling 0.5 CFU/ml to be detected.

1.1.6 Electrochemical impedance biosensors

Electrochemical impedance biosensors can be based on the fact that the metabolic redox reactions of microorganisms are detectable and quantifiable when performed in the presence of a suitable mediator [39]. Radke *et al.* used a high-density microelectrode array to develop an impedance biosensor for measurement of *E. coli* O157:H7. The sensitivity of the sensor could reach to 10^7 CFU/ml with coating a goat anti-IgG polyclonal antibody layer to capture targets [41]. An impedance sensor to measure *internalin B* was developed by the team of Tully in 2008 [42]. A biotinylated leporine polyclonal antibody and a L. monocytogenes cell-surface protein were applied in this platform. When captured on avidin-coated planar carbon electrodes modified with a conductive polymer (polyaniline), the limit of detection for *internalin B* was found to be 4.1 pg/ml

1.2 The motivation of this research

Piezoelectric biosensing methods are usually used on the applications of acoustic wave sensor and have a number of advantages. For example, compare with the optical biosensing methods, piezoelectric biosensing methods can be operated with simple and cheap electronic components. The cost per additional sample channel is low on acoustic

wave sensors. This allows the creation of cost-effective sensor arrays of a single device. Acoustic wave sensors are extremely versatile sensors that are just beginning to realize their commercial potential [50]. They are competitively priced, inherently rugged, very sensitive, intrinsically reliable, and offer the additional benefit of being passively wirelessly interrogated. Wireless sensors are beneficial when monitoring parameters on moving objects, such as tire pressure on cars or torque on shafts. Sensors that require no operating power are highly desirable in remote locations, making these sensors ideal for remote chemical vapour, moisture, and temperature sensors. As a result of their mass sensitivity, they can be used in numerous physical, chemical, and biological applications [50-52]. Other applications include measuring force and acceleration, shock, angular rate, viscosity, displacement, flow, and film characterization. The sensors also have an acoustoelectric sensitivity, allowing the detection of pH levels, ionic contaminants, and electric fields. SAW sensors have proven to be the most sensitive sensors in general, as a result of their larger energy density on the surface.

For liquid sensing, a special class of SH-SAW sensors, called Love wave sensors, have been proven to be the most sensitive [50]. Furthermore, Love wave devices are attractive for biosensor application owing to providing a simplicity, small size, and real-time solution. However, there are some problems with the conventional measurement of Love wave biosensors. In the past, researchers usually used micro-channels or micro-chambers system to input and output the test specimens [58-62]. These methods were suitable for liquid sensing because it was easy to control the flow. But after the test specimens were loaded onto the platform, the residues of the test specimens can be found to be difficult to remove. Previous studies did not verify that the residues could be totally removed in the platforms with micro-channels or micro-chambers. Hence, it is doubtful whether the Love wave biosensors with micro-channels or micro-chambers is a suitable format for a reusable device. In this study, a droplet based technique was used to replace micro-channels or micro-chambers platform. After each measurement, the sensing area

could be treated with plasma to clean and remove all particles on the platform. This method has been verified as being useful for platforms that need to be reused several times.

Another problem of the application of Love wave sensors is restricted to a single phase (gas, liquid, solid etc.). Consequently, researchers usually design the sensing film on the sensor to measure targets under specific conditions. If targets need to be observed and detected in the liquid phase as the first step, then removing the solution from the sensing area and measuring the immobilised particles in dry state, the traditional Love wave sensors do not readily satisfy this demand. In addition, the measurable parameter for a Love wave sensor is the mass change following target immobilisation. This leads to a problem, which is that the sensor can only measure the quantity of targets but cannot distinguish the elements of targets. In order to solve this problem, it is necessary to add another sensor to work with the Love wave sensor and provide an additional parameter to aid the identification of targets and/or calibrate the Love wave sensor response. The aim of this research is to develop a biosensor by employing a Love wave device and an electrochemical impedance sensor to solve the above problems.

1.3 Literature review of Love wave biosensors

The report published by Gaso *et al.* in 2013 was a detailed review about SAW biosensors [51]. According to this report, early studies in the 1980s that attempted to transfer the simple method of SAW gas sensing into a biosensor were not successful. This is because the researchers used Rayleigh Waves, which is a kind of SAW that includes both longitudinal and transverse motions. In these devices the signal attenuated sharply when immersed in liquids [45]. Early successful approaches using horizontally polarized shear wave (HPSW) on quartz devices in a delay line configuration could only be obtained in nonpolar liquid [113]. If immersed in water, such devices also suffered from higher attenuation. The reason to serious signal attenuation was from significant dielectric mismatch between the liquid and the substrate (dielectric constant of water is about 78, but

the dielectric constant of quartz is about 4). The team of Flory used a new acoustic wave type called surface transverse waves (STW) to design a biosensor [45]. This type of wave propagates on the surface of the device by a periodic mass grating with a periodicity of λ/2, where λ is the wavelength of the SAW. This way provided better energy confinement on the crystal surface than a pure HPSW traveling along the open surface of a crystal. Although this type of surface wave was more suited to applications in liquids, the substrate material was still quartz so the problem of dielectric mismatch still existed [45]. In order to operate efficiently in applications which require fluid immersion, the Shear Horizontal Surface Acoustic Wave (SH-SAW) sensor was developed. Researchers tried to find substrates that can generate SH-SAW, and they investigated the materials such as 36° Y–X $LiTaO_3$ and 64° Y–X $LiNbO_3$. Although the pure shear horizontal waves could not be generated in these substrates, another kind of SAW, leaky-SAW, was found in these materials. The leaky-SAW is mainly shear horizontal but not purely shear horizontal. Moreover, this wave extends several wavelengths into the device. But the dielectric constant of $LiTaO_3$ and $LiNbO_3$ are 47 and 85, respectively, which are closer to the dielectric constant of the water and lessen the effect of mismatch of dielectric constant [103]. The major disadvantage of leaky-SAW devices is that the IDTs are directly exposed to aqueous media, so the lifetimes of such devices are not long due to corrosion [103]. In order to prevent IDTs from corrosion in liquid, other scientists covered a thin polymer layer on the devices and another kind of SAW, a Love wave device, was generated when some particular conditions were met. The condition for the existence of Love wave modes is that the shear velocity of the overlay material is less than that of the substrate and the thickness of guiding layer is less than the wavelength of the shear wave [51]. The guiding layer confines the wave energy keeping it near the surface and slows down the wave propagation velocity. Because the Love wave is trapped tightly in the guiding layer, it is strongly perturbed by surface changes, yielding high sensitivity. This device operates with a surface wave with shear horizontal particle displacements. As a result, it can operate

efficiently in both gas and liquid media [103].

The first two research teams took advantages of Love wave devices for biochemical sensing were Kovacs et al. [52] and Gizeli et al. [53] in 1992. They demonstrated how to use such devices as mass sensing biosensors in liquids. After that, in 1997, Love wave devices were employed to detect real-time antigen-antibody interactions in liquid media [54]. In 1999, a contactless Love wave device was developed in order to protect electrodes from the conductive and chemically aggressive liquids used in biosensing [55]. The advantage of this technique is that no bonding wires are required. One year later, a dual channel Love wave device was used as a biosensor to simultaneously detect Legionella and E. coli by Howe and Harding [56]. In this approach a novel protocol for coating bacteria on the sensor surface prior to addition of the antibody was introduced. Quantitative results can reach to 106 cells/ml, which were obtained from both species within 3 hours. In 2003, a Love wave immunosensor was designed as a model for virus or bacteria detection in solution by Tamarin *et al.* [57]. They grafted a monoclonal antibody (AM13 MAb) against M13 bacteriophage on the device surface (SiO_2) and detected the M13 bacteriophage/AM13 immunoreaction. The authors suggested the potentialities of such acoustic biosensors for biological detection. The same year, it was shown that mass sensitivity of Love wave devices with ZnO layer was larger than that of sensors with SiO_2 guiding layers and the researchers monitored the adsorption of rat immunoglobulin G, obtaining mass sensitivities as high as 950 cm^2/g [58]. They pointed out that such a device was a promising candidate for immunosensing applications. An aptamer-based Love wave sensor which allowed the detection of small molecules was developed by Schlensog et al. in 2004 [59]. This biosensor provides an advantage over immunosensors because it does not require the production of antibodies against toxic substances. A Love wave biosensor for the detection of pathogenic spores at or below inhalational infectious levels was reported by Branch *et al.* in 2004 [60]. A monoclonal antibody with a high degree of selectivity for anthrax spores was used to capture the non-pathogenic simulant Bacillus

thuringiensis B8 spores in aqueous conditions. Moreover, the Branch team stated that Love wave biosensors have widespread application for whole-cell pathogen detection. Moll *et al.* invented a new method with a Love wave biosensor to detect E. coli in 2007 [61]. This sensor consisted of grafting goat anti-mouse antibodies (GAM) onto the sensor surface and introducing E. coli bacteria mixed with anti-E. coli MAb in a second step. The sensor response time was shorter when working at 37°C, providing results in less than 1 hour with a detection threshold of 10^6 bacteria/ml. More recently, the same group described a multipurpose Love wave immunosensor for the detection of bacteria, virus and proteins [62]. They successfully detected bacteriophages and proteins down to 4 ng/mm^2 and E.coli bacteria up to 5.0×10^5 cells in a 500 μL chamber, with good specificity and reproducibility. In addition, Moll *et al.* indicated that whole bacteria can be detected in less than one hour [62]. Andrä *et al.* used a Love wave biosensor to investigate the mode of action and the lipid specificity of human antimicrobial peptides [63]. They analysed the interaction of those peptides with model membranes. These membranes mimic the cytoplasmic and the outer bacterial membrane when attached to the sensor surface. In 2008, Bisoffi *et al.* [64] employed a Love wave biosensor to detect Coxsackie virus B4 and Sin Nombre Virus (SNV), a member of the Hantavirus family. They described a biosensor with working frequency at 325MHz, which has the specificity provided by monoclonal and recombinant antibodies for the detection of viral agents. Rapid detection (within seconds) for increasing virus concentrations was reported. The biosensor was able to detect SNV at doses lower than the load of virus typically found in a human patient suffering from Hantavirus cardiopulmonary syndrome. In 2009, it was shown the possibility to graft streptavidin-gold molecules onto a Love wave sensor surface in a controlled way and was demonstrated the capability of the sensor to detect nano-particles in liquid by Fissi *et al.* [65]. In 2010, a complementary metal-oxide semiconductor CMOS structure combined with a Love wave biosensor for breast cancer biomarker detection was presented by Tigli *et al.* [66]. This biosensor was fabricated by using CMOS technology and used gold as

guiding layer and as interface material between the biological sensing medium and the transducer. Love wave devices were used as sensors for okadaic acid immono-detection through immobilized specific antibodies by Fournel *et al.* [67]. They obtained three times higher frequency shifts with the okadaic acid than with an irrelevant peptide control line. A Love wave device based bacterial biosensor for the detection of heavy metal in aqueous media was reported in 2011 by Gammoudi *et al.* [68]. Whole bacteria (E. coli) were fixed as bioreceptors onto the acoustic path of the sensor coated with a polyelectrolyte multilayer using a layer by layer electrostatic self-assembly procedure. Changes of bacteria viscoelastic equivalent parameters in presence of toxic heavy metals were observed. A Love wave-based wireless biosensor for the simultaneous detection of anti-Dinitrophenyl-KLH (anti-DNP) immunoglobulin G (IgG) was presented by Song *et al.* in 2011 [69]. They used poly (methyl-methacrylate) (PMMA) guiding layer and two sensitive films (Cr/Au). A Love wave biosensor which has phase shifts as a function of the immobilized antibody quantity, combined with an active acoustic mixing device, was reported by Kardous *et al.* [70] in 2011. They evaluated that mixing at the droplet level increases antibodies transfer to a sensing area surface and raised the reaction kinetics by removing the dependency with the protein diffusion coefficient in a liquid, while inducing minimum disturbance to the sensing capability of the Love wave device. Love wave biosensors have been also used to investigate the properties of protein layers [71], DNA [72] and detect the adsorption and desorption of a lipid layer [73]. In 2013, Matatagui *et al.* used electrospinning technique to set sensitive layers on Love wave sensors to form a sensor array [74]. This gas sensor can detect very low concentrations of target, such as 0.2ppm of DMMP and 1ppm of DPGME. In 2014, Mitsakakis *et al.* integrated Love wave sensors with microfluidics to implement multi-sample sensing [75]. They demonstrated the quantitative correlation of the acoustic signal with the molecular weight of surface bound proteins under several binding conditions. Four cardiac marker proteins (from 86 kDa to 540 kDa) have been measured by their sensors successfully and their results emphasized

the quantitative nature of the phase of the acoustic signal in determining mass of the bound proteins.

Currently, the commercial Love wave biosensor system available in the market is SAW instruments GmbH, which is a German company started as an R&D-project at the Centre for Advanced European Studies and Research in Bonn in 2000. The sensor system can achieve a limit of detection of 0.05 ng/cm^2 with a sample volume of 40-80 μL. Another France company, Mougins, has a commercially available microbalance development kit (SAW-MDK1) which consists of a two-channel Love wave delay lines. Generally speaking, Love wave biosensors have not been very well recognized by both the scientific community and the market [76]. This might be due to the technical hindrances found for applying this device as biosensor, since it is sensitive to changes in the viscoelastic properties of the coating, which complicates the results interpretation. Reports about applications where mass alterations are separated from viscoelastic effects can enhance the acceptance of Love wave biosensors and this point of view will be applied in this study.

Chapter 2 Methods and Materials

2.1 Selection of piezoelectric materials

Piezoelectricity was discovered in 1880 by two brothers, Jacques and Pierre Curie, who observed some crystals such as quartz, Rochelle salt and tourmaline which generate spontaneous polarization when mechanical stress are applied to these materials [50] and vice versa. There are two types of piezoelectric effect: 1) one is direct piezoelectric effect; 2) the other is converse piezoelectric effect. When a mechanical stress is applied to the piezoelectric material, an opposite polarization occurs, and can be changed by inverting the direction of applied stress, as shown in Figure 2.1(a). This phenomenon is called the direct piezoelectric effect. The converse piezoelectric effect is opposite to the direct piezoelectric effect. When an electric field is applied to the piezoelectric material, the stress on the substance would be changed as function of the strength of the electric field, as shown in Figure 2.1(b). The transformation of the electric energy to the mechanical stress is called converse piezoelectric effect [77].

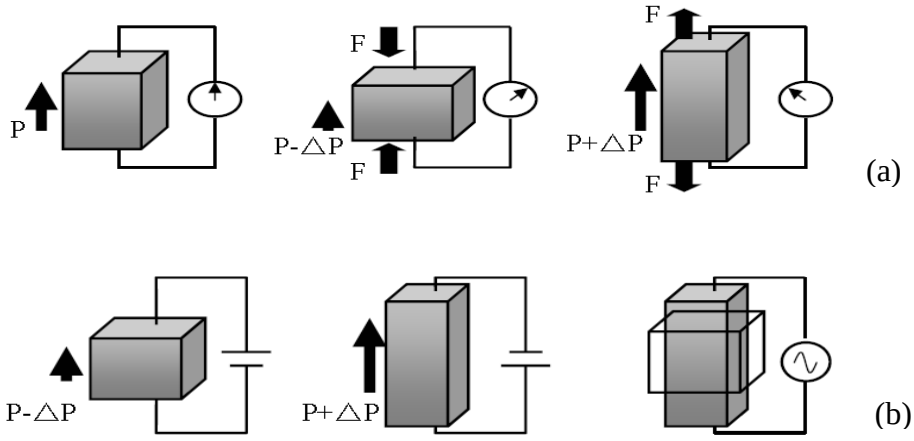

Figure 2.1 P is the electrical potential. ΔP is the change of the electrical potential. (a) Direct piezoelectric effect. F is the stress applied on the material. (b) Converse piezoelectric effect. The change of the electrical potential deforms the shape of piezoelectric material.

Many different types of acoustic waves can propagate in solid materials, and Love waves are particularly investigated in this study [78]. The subject of surface acoustic wave (SAW)

devices is concerned with all types of surface waves that can propagate on a half-space, making use of piezoelectricity [79]. It will be seen that this includes piezoelectric Rayleigh waves, leaky surface waves, surface transverse waves (STWs), Bleustein-Gulyaev waves and, in layered systems, layered Rayleigh waves and Love waves. The key point to know how Love waves can be excited and propagate is to find solutions from wave equations. Let us consider a half-space of material covered by a layer of another material, with layer thickness d as displayed in Figure 2.2. If the layer thickness is small than the wavelength of the Love wave, the solutions that will be similar to the Rayleigh wave for a half-space and can be described as 'layered Rayleigh waves'. The solutions may be found by summing partial waves. The layer material is taken to have plane-wave velocities V_l and V_t. In addition to layered Rayleigh waves, the layered system can also support surface waves with the displacements normal to the sagittal plane (x_1, x_3). These are known as Love waves [80]. In this case the partial waves are shear waves, with wave vectors $\mathbf{k_t} = (\beta, 0, \pm T)$ in the layer and $\mathbf{k_t'} = (\beta, 0, \pm T')$ in the half-space. Thus the displacements in the layer can be written [79]:

$$u_t = \mathrm{A}(0,1,0)\exp(-jTx_3) + \mathrm{B}(0,1,0)\exp(jTx_3) \tag{2.1}$$

and the displacement in the half-space is [79]:

$$u_t' = \mathrm{C}(0,1,0)\exp(-jT'x_3) \tag{2.2}$$

where A, B and C are constants. The boundary conditions are the same as for the Rayleigh-wave case, which there should be no forces on the free surface at x_3 =0, and applying these gives the dispersion relation [79]:

$$\tan(Td) = \mathrm{j}\mu'T'/(\mu T) \tag{2.3}$$

where μ and μ' are respectively the rigidities of the layer material and the half-space material. Solving for β gives in general a number of modes. Solutions are obtainable only for $V_t < V_t'$, and the solutions must have velocities less than V_t', so that T' is imaginary and the displacement decays in the half-space. At zero frequency the Love-wave solution

becomes identical to the SH plane-wave solution for a half-space. Thus Love waves can be regarded as modified forms of the SH plane wave, where the presence of a layer with low acoustic velocity converts the plane wave into a surface wave and causes dispersion.

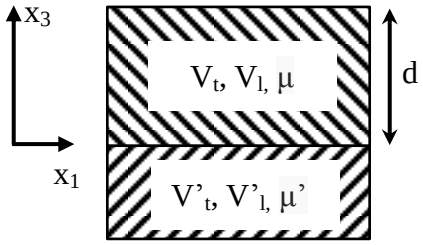

Figure 2.2 The structure of a half-space of material covered by a layer of another material, with layer thickness d. V_t and V'_t is the phase velocity for shear waves, respectively. V_l and V'_l is the phase velocity for longitudinal waves, respectively.

The effects associated with crystal symmetry can be summarized as follows (the reference coordinates is as shown in figure 2.2) [81]:

(a) If the sagittal plane (x_1, x_3) is a plane of mirror symmetry of the crystal, then the transverse displacement u_2 is decoupled from u_1, u_3 and Φ. In this case, there may be a piezoelectric Rayleigh-wave solution with **u** in the sagittal plane.

(b) If the sagittal plane is normal to an even-order axis of the crystal, then the components u_1 and u_3 are decoupled from u_2 and Φ. In this case, there may be a non-piezoelectric Rayleigh wave with **u** confined to the sagittal plane, and possibly also a Bleustein–Gulyaev-wave solution.

These solutions are called ‘pure’ modes. They have the property that the wave velocity in the (x_1, x_2) plane is symmetric about the x_1 direction, and therefore it has a maximum or minimum in this direction. The Rayleigh-wave and the Bleustein-Gulyaev-wave solutions are strongly related to the Rayleigh- and the SH-wave solutions for an isotropic half-space, and these are in turn related to the solutions for a layered half-space. These relationships are summarized in Table 2.1.

The piezoelectricity can only be present in the anisotropic materials. Moreover, its properties vary with direction in relation to the internal structure [82]. The requirements for

surface-wave devices have led to a very substantial search for suitable materials, a complex topic because for each potential material it is necessary to assess the relevant properties for all crystal orientations. Important properties are the wave velocity, piezoelectric coupling, temperature effects, diffraction, attenuation and the level of unwanted bulk-wave generation. It was found that on some crystals the surface-wave propagation was almost ideal.

Table 2.1. Summary of wave types.

Isotropic half-space		Anisotropic half-space
Non-layered	Layered	
Rayleigh wave	Rayleigh wave (dispersive)	Rayleigh wave Leaky surface wave
SH plane wave	Love wave SH (dispersive)	Bleustein–Gulyaev wave

However, even small imperfections can be relevant when exact requirements are to be met, and temperature effects always need to be considered. Since the material properties vary with direction, it is essential to quote the orientation when specifying a material. For example, a general case is 64°Y–X lithium niobate ($LiNbO_3$). This is a rotated Y-cut. The surface normal makes an angle 64° with the crystal *Y*-axis and the wave propagates in the crystal *X*-direction as shown in Figure 2.3. This case has strong piezoelectric coupling, but the temperature stability is poor. The reverse is the case for ST–X quartz (SiO_2). This is a 42.7° rotated Y-cut, with wave propagation along X. It has good temperature stability, as quantified by the temperature coefficient of delay (TCD). TCD is the change rate of the velocity of acoustic waves with the variation of the temperature. The delay is maximized at 21℃, where the TCD is zero, and for practical purposes the delay is a quadratic function of temperature. Many of the surface-wave properties of a material can be deduced by calculating the wave velocity, which is a complex calculation because it involves anisotropy and piezoelectricity. The wave velocities for a free surface and a metallized

surface are denoted by v_f and v_m, respectively. In the latter case, the surface has an idealized metal coating which shorts out the parallel component of electric field at the surface, but is too thin to have any mechanical effect. The fractional difference between these velocities, $\Delta v/v$, characterizes the piezoelectric coupling to the wave. It is also common to define a coupling constant K^2 as twice this value, therefore [81]

$$\frac{\Delta v}{v} \equiv \frac{v_f - v_m}{v_f} \equiv \frac{K^2}{2} \tag{2.4}$$

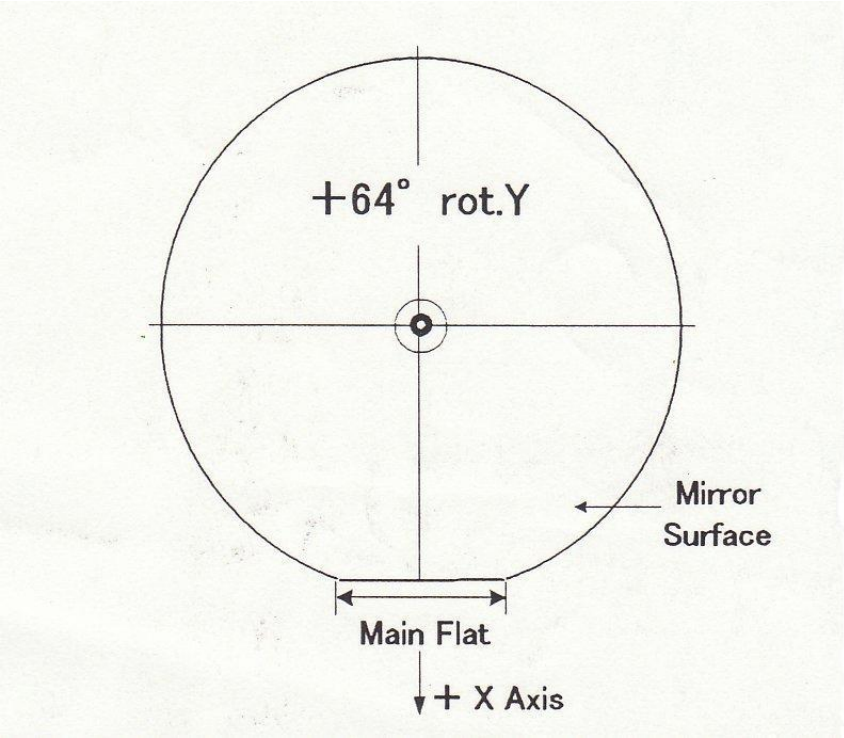

Figure 2.3 The orientation of the 64°Y–X $LiNbO_3$. *Y*-axis is the normal direction of the cut face. *X*-axis is the direction of SAW propagation.

Surface-skimming bulk waves (SSBW) is a kind of leaky surface in an isotropic material [83]. It is a plane shear horizontal (SH) bulk wave, which can propagate parallel to the surface without violating the boundary conditions, so it has no associated stress on the surface. Related cases occur in anisotropic materials, for example in quartz [84]. In particular orientations, the boundary condition is almost satisfied and low-loss propagation between two transducers can be obtained. Such waves can have high velocities, making them attractive for high-frequency devices. An example is 36°Y–X+90° quartz, which

gives a velocity of 5100 m/s and a temperature coefficient of delay (TCD) of zero. The delay is a quadratic function of temperature and the constant c is about 60×10^{-9} $(°C)^{-2}$. Propagation is normal to the X axis. This case also gives zero piezoelectric coupling to a Rayleigh-type surface wave. Similar behaviour is found in 64°Y–X lithium niobate ($LiNbO_3$) and in 36°Y–X lithium tantalate ($LiTaO_3$). These orientations support leaky waves.

If the analogy of an SH bulk wave is accepted, it might be expected that the amplitude of an SSBW will not be much affected by the presence of the surface. Thus, as for a cylindrical bulk wave in an infinite medium, an amplitude variation as $x^{-1/2}$ is expected. This is indeed found experimentally when a transducer generates SSBWs in quartz [84]. In the above orientations of $LiNbO_3$ and $LiTaO_3$, amplitude variations as $x^{-1/2}$ and $\exp(-\alpha x)$ have both been reported [85]. These can be interpreted as SSBWs and leaky waves, respectively. Hashimoto gives a theoretical interpretation by making the approximation that the material has 6 mm symmetry, showing that both types of x variation can occur. The theory shows that the SSBW amplitude falls as $x^{-1/2}$ at small x and as $x^{-3/2}$ at large x [86]. Auld also showed that, in an isotropic material, a bulk SH wave can be guided along the surface by an array of grooves parallel to the wave front [87]. This concept can be applied to the SSBW in 36°Y–X+90° quartz, in which the wave can be trapped at the surface by the metal strips comprising reflecting gratings and single-electrode transducers. When used in this way, the wave is known as a surface transverse wave (STW) [88]. The SSBW orientations do give normal modes with low loss. Generally, the solution gives velocity higher than that of the slowest bulk wave, satisfying the boundary conditions but with some attenuation due to radiation of energy into the bulk. At particular orientations the attenuation may become insignificant because of decoupling between the wave and the lowest-velocity bulk wave, and then the wave may be suitable for practical devices. The term ‘leaky surface acoustic wave’ (LSAW), or ‘pseudo surface wave’ (PSAW), is used for

such cases when the attenuation is small or zero. In contrast, Rayleigh waves generally exist for all orientations. A wide variety of leaky-wave cases have been found, including the above orientations of quartz, $LiNbO_3$ and $LiTaO_3$ [89]. Generally, the solutions of wave equations of LSAW can have the following characteristics:

(a) Low attenuation only at one specific orientation (at neighbouring orientations, the attenuation increases).
(b) High velocity, higher than that of the slowest bulk wave, attractive for high frequency applications.
(c) A grating is often necessary to trap the wave at the surface.
(d) Piezoelectric coupling higher than that of surface waves, dependent on the grating thickness.
(e) Temperature stability similar to that of surface waves, or better.

Table 2.2 displays the properties of leaky waves on uniform metallized surfaces for several piezoelectric materials. The coupling constant of 64°Y-X $LiNbO_3$ is the highest among these materials and it indicates the highest efficiency of the energy transformation from surface waves to electrical signals. Although the TCD of 64°Y-X $LiNbO_3$ is a little high, this problem can be solved by temperature compensation through appropriate system design. A dual channel system is usually used to overcome the problem [51]. In this system, two delay lines are installed on the same substrate. The sensing area is set up on the one of them and the other is a reference channel. When conducting experiments, the substrate is arranged on a temperature-control plate to maintain the temperature constant. The interferences of measurement which is generated by TCD in the sensing channel can be neutralised by the measurement in reference channel [51]. As a result, I have chosen 64°Y-X $LiNbO_3$ as substrate in this study.

Table 2.2. Properties of leaky surface waves on uniform metallized surfaces [79].

Material	Velocity(m/s)	K^2(%)	TCD (ppm/°C)	Attenuation(dB/λ)
36° Y-X $LiTaO_3$	4109	5.6	32	0
Quartz, ST-X	5078	0.03	0	0.008
Y-Z $LiNbO_3$	7178	3	94	1.5
64° Y-X $LiNbO_3$	4450	10.2	81	0.004

An introduction of the nature of $LiNbO_3$ is reported in the following paragraph. Lithium Niobate ($LiNbO_3$, LN), is an artificial, negative, uniaxial, non-centrosymmetric, ferroelectric crystal. $LiNbO_3$ is a widely used crystal in different fields of science and technology. As matter of fact, $LiNbO_3$ is characterised by large pyroelectric, piezoelectric, nonlinear and electro-optic coefficients and it is also employed for applications in which acoustic and acousto-optic properties are required. The preferred method to growth this crystal is the Czochralski technique. Figure 2.4 shows the typical setup employed in this method [90] and an example of single crystal of $LiNbO_3$ [91]. $LiNbO_3$ is grown from pure powders of lithium carbonate (Li_2CO_3) and niobium pentoxide (Nb_2O_5) that are melted in a platinum crucible. The following chemical reaction regulates the crystal growth:

$$Li_2CO_3 + Nb_2O_5 \rightarrow 2\ LiNbO_3 + CO_2$$

The reaction occurs in the platinum crucible that is placed inside a furnace. The reactants are heated to the melting point, and then they kept in the liquid phase. Then a seed attached to the end of a pull rod is brought close to the melt surface, and heated to a temperature near the melting point of $LiNbO_3$ (1250°C) [92]. After that, the pulling rod is lowered to get into contact with the melt surface, so that the reaction at the solid–liquid interface takes place. At the right temperature, just above the melting point of $LiNbO_3$, atoms from the liquid will adhere to the seed. At higher temperatures, the seed melts while on the contrary at lower temperatures the melt freezes locally around the seed. During the growth of the crystal, the rod is kept in rotation in order to guarantee homo-geneity and to avoid thermal gradients in the crystal.

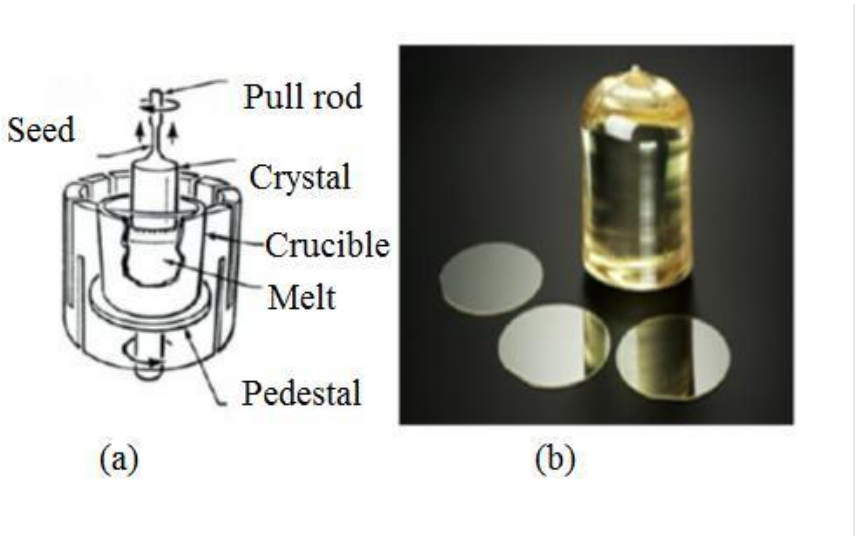

Figure 2.4 (a) Setup view for the growth by using Czochralski technique [90]. (b) Single Crystal of $LiNbO_3$ [91].

The diameter of the crystal boule is kept constant during the growth until the desired length is reached. The control of boule dimensions is achieved by setting the choosing the diameter of the crucible, the rotation and the pulling rate. The crystal is finally separated from the melt by increasing the temperature and raising the rod. After the separation, the growth chamber is cooled down to room temperature. The crystal is then cut and polished. $LiNbO_3$ can be grown in a wide range of compositions. The composition exactly matching the chemical compound $LiNbO_3$, having a ratio of [Li]:[Nb]:[O] of 1:1:3 is commonly referred as Stoichiometric Lithium Niobate (SLN). However, due to the volatility of the Li ions and their consequent deficiency in the crystal, the growth of the stoichiometric composition is quite challenging. The composition that is commonly used and is easiest to grow with a good uniformity is the congruent one (C-$LiNbO_3$). Historically, $LiNbO_3$ has been prepared in both stoichiometric and congruent composition. The latter is now the preferred one because of its highest optical quality and uniformity. Figure 2.5 shows the phase diagram for $LiNbO_3$ [93]. There is a unique point called congruent point, at which both the solid and the liquid phase can co-exist and it corresponds to the highest point on the melting temperature line.

$LiNbO_3$ belongs to the perovskite crystal family. The crystal structure that consists of planar sheets of oxygen atoms in a distorted hexagonal close-packed configuration is shown in Figure 2.6 [94]. The interstices of the oxygen octahedra are filled one-third by lithium ions, one-third by niobium and one-third is vacant. In z direction, the atoms are placed in the interstices in the following order: Nb, vacancy, Li [95].

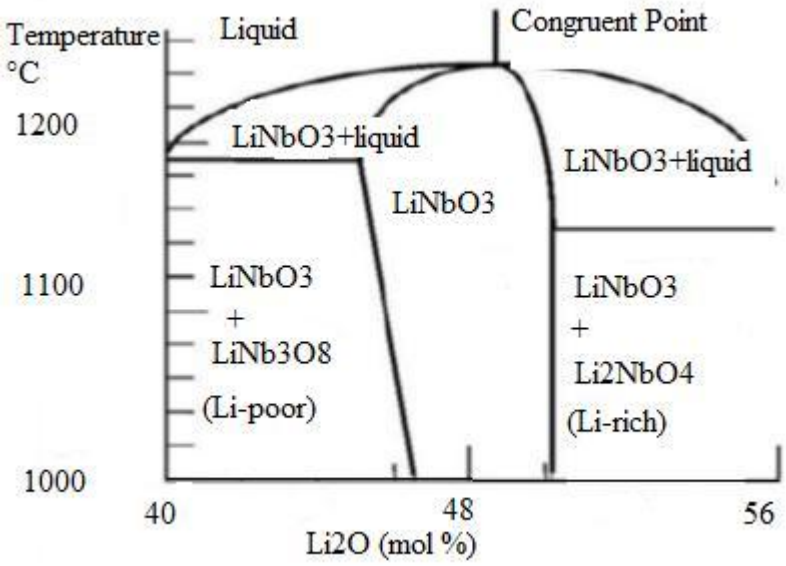

Figure 2.5 Li_2O-Nb_2O_5 equilibrium temperature-composition phase diagram of $LiNbO_3$ [93].

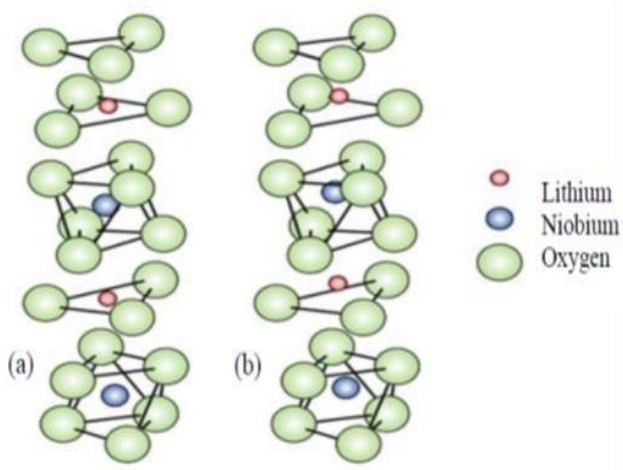

Figure 2.6 (a) Paraelectric phase $LiNbO_3$ (b) Ferroelectric phase $LiNbO_3$ [94].

$LiNbO_3$ is a trigonal crystal since it exhibits three-fold rotation symmetry around the c-axis. It exhibits mirror symmetry of three planes lying 60° apart and forming a threefold rotation axis, as shown in Figure 2.7. These two symmetries classify $LiNbO_3$ as a member

of the 3m point group it also belongs to the R3c space group [96]. $LiNbO_3$ is ferroelectric below the Curie temperature (1140℃) whereas when above (but below the melting temperature) the displacement of the Li and Nb ions in respect to the oxygen planes vanishes and therefore the spontaneous polarization vanishes too, then the paraelectric phase arises.

The orientation of the c-axis is given by the position of two neighbour lithium and niobium atoms, as well as of the vacancies with respect to the closed-packed oxygen planes. The two atoms are displaced slightly away from the octahedra centre along c-axis, which arising a spontaneous polarization aligned along this axis. These pairs can work as individual axis and they can be aligned either up or down indicating the domain polarizations. The standard methods to determine the c-axis orientation is to compress the crystalline in the c-axis direction. The c^+ face (the positive end of the ferroelectric dipole) will exhibit a negative charge under compression, when the niobium and the lithium ions move closer to their paraelectric position, thus reducing the dipole, while the c^- face (the negative end of the dipole) exhibits a positive charge under compression.

The unit cell type of $LiNbO_3$ in this study is showed in Figure 2.7. This is a hexagonal structure. In this structure, the z-axis is chosen to be parallel to the c-axis of the crystal. The y-axis is chosen to be parallel to one of the mirror plane, and the x-axis chosen so to form a right-handed system [97]. This conventional hexagonal unit cell contains six formula weights (147.843 amu). The three covalent bonds in the hexagonal unit cell are 120 degree apart and lie in a plane normal to the c-axis. These axes are chosen to be perpendicular to the mirror planes (a_1 and a_2 are shown in Figure 2.7). It is conventional to take in this hexagonal unit cell the Nb as the origin, for the congruent compounds $LiNbO_3$ unit cell length a, are a_H = 5.1536 Å. While in the other type rhombohedra unit cell, a_R 5.474 Å and the angle α between these three axes are 56.180 degree [98].

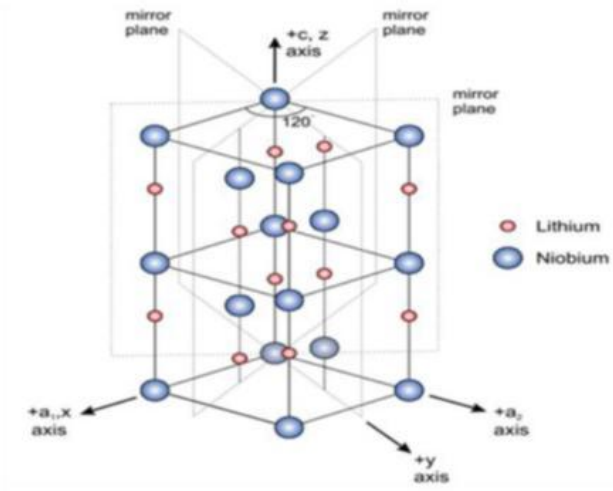

Figure 2.7 $LiNbO_3$ symmetry mirror phase [97].

2.2 Using interdigital transducers to generate surface acoustic waves on piezoelectric materials

In this section, the theory of electrical excitation by interdigital transducers and the effective permittivity for a piezoelectric half-space are discussed [99]. The method was first developed by Ingebrigtsen [100] on the situation of electrostatic case for a non-piezoelectric material. Afterwards, Greebe *et al.* [101] and Milsom *et al.* [102] applied it to analyse the electrical excitation on piezoelectric substrates. Other approaches are the perturbation theory [103] and normal mode theory [104]. They generated results which are basically the same as the method used here. Coordinate axes are defined as in Figure 2.8.

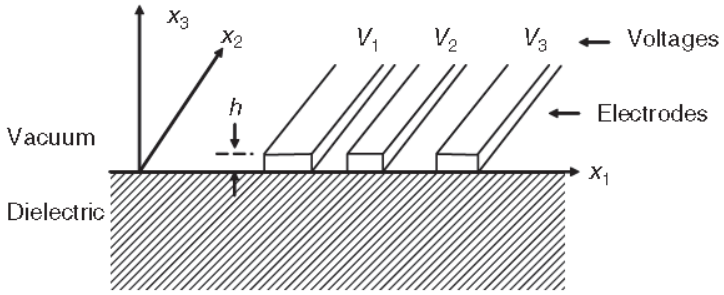

Figure 2.8 General configuration of electrodes on a dielectric substrate. Fields are independent of x_2, and the waves propagate in $\pm x_1$ directions.

It is assumed that the variables (surface particles' displacements) are proportional to $\exp(j\omega t)$, with the positive frequency ω. Initially a harmonic solution with variables

proportional to $exp(j\beta x_1)$, with β real, and generalize later using Fourier synthesis. Let us consider partial waves in which the displacements **u'** and potential ∅' have the form [99]:

$$\mathbf{u}' = \boldsymbol{u}'_0 exp(j\gamma x_3) exp[j(\omega t + \beta x_1)] \quad (2.5)$$
$$\emptyset' = \emptyset'_0 exp(j\gamma x_3) exp[j(\omega t + \beta x_1)]$$

Where $\mathbf{u}'_0$ and $\emptyset'_0$ are constants and γ is the x_3 component of the wave vector, which by definition has no x_2 component. These expressions are required to satisfy the equation of motion in an infinite medium with the material tensors rotated into the frame of the axes x_1, x_2, x_3 as follows [99],

$$\rho \frac{\partial^2 u_i}{\partial t^2} = \sum_j \sum_k \left\{ e_{kij} \frac{\partial^2 \emptyset}{\partial x_j \partial x_k} + \sum_l C^E_{ijkl} \frac{\partial^2 u_k}{\partial x_j \partial x_l} \right\} \quad (2.6)$$

Substitution into equations (2.6) gives four linear homogeneous equations in the four variables $\mathbf{u}'_0$ and $\emptyset'_0$. Because they do not correspond to excitation at the surface, four of the roots are not acceptable. It is necessary to choose reasonable roots carefully to have a surface-wave solution. If the imaginary part of γ is negative, complex or imaginary values are acceptable so that $\mathbf{u}'_0$ and $\emptyset'_0$ decay away from the surface. Real values of γ provide plane waves, and these are acceptable only if they carry energy away from the surface. Usually this requires γ to have its sign opposite to β. The four acceptable partial-wave solutions are written as [99]:

$$\boldsymbol{u}'_m = \boldsymbol{u}'_{0m} exp(j\gamma_m x_3) exp[j(\omega t + \beta x_1)] \quad (2.7)$$
$$\emptyset'_m = \emptyset'_{0m} exp(j\gamma_m x_3) exp[j(\omega t + \beta x_1)]$$
$$m = 1, 2, 3, 4$$

The total solution in the half-space has displacements $\tilde{\boldsymbol{u}}$ and $\tilde{\emptyset}$, where the tilde indicates a harmonic solution with variables proportional to $exp(j\beta x_1)$. The total solution is taken as a linear combination of the partial waves, so that [99]:

$$\tilde{\boldsymbol{u}} = \sum_{m=1}^{4} A_m \boldsymbol{u}'_m \quad (2.8)$$

$$\tilde{\emptyset} = \sum_{m=1}^{4} A_m \emptyset'_m$$

The mechanical boundary conditions require that there are no forces on the surface, so that T_{13}= T_{23}= T_{33}=0 at x_3=0, with the strain T_{ij}. T_{ij} can be written as the linear relation [99]:

$$T_{ij} = \sum_k \sum_l C^E_{ijkl}\, S_{kl} - \sum_k e_{kij}\, E_k \tag{2.9}$$

Here, the superscript on C^E_{ijkl} identifies this as the stiffness tensor for constant electric field; that is, this tensor relates changes of T_{ij} to changes of S_{kl} when E is held constant. Therefore there are three homogeneous equations (2.5, 2.7, 2.8) relating the four (m=1,2,3,4) constants A_m, and the relative values of these constants can be found. The relative values of $\widetilde{\boldsymbol{u}}$ and $\widetilde{\emptyset}$ can be calculated from equation (2.8), giving a solution for any value of β. The surface boundary conditions concern the potential and the displacement $\widetilde{\boldsymbol{D}}$**.** The latter can be calculated from $\widetilde{\boldsymbol{u}}$ and $\widetilde{\emptyset}$ by means of the following equation [99]:

$$D_i = \sum_j \varepsilon^S_{ij} E_j + \sum_j \sum_k e_{ijk} S_{jk} \tag{2.10}$$

Here ε^S_{ij} is the permittivity tensor for a constant strain. At the surface, the value of $\widetilde{\boldsymbol{D}_3}$ is denoted by $\widetilde{\boldsymbol{D}_{3-}}$ on the piezoelectric side, and $\widetilde{\boldsymbol{D}_{3+}}$ on the vacuum side. The surface potential is $\widetilde{\emptyset}(x_1) \equiv \widetilde{\emptyset}(x_1, 0)$**.** The ratio between $\widetilde{\boldsymbol{D}_{3-}}$ and $\widetilde{\emptyset}(x_1)$ is determined by the above solution, and in general it is a function of β.

In the vacuum $x_3 > 0$, the potential satisfies Laplace's equation $\nabla^2\widetilde{\emptyset} = 0$. Since $\widetilde{\emptyset}$ is proportional to $exp(j\beta x_1)$ and it must vanish for $x_3 \to \infty$, the x_3 dependence is $exp(-|\beta|x_3)$, and so $\widetilde{\emptyset}(x_1, x_3) \equiv \widetilde{\emptyset}(x_1)\exp(-|\beta|x_3)$. It follows that [99]:

$$\widetilde{D_{3+}} = \varepsilon_0|\beta|\widetilde{\emptyset}(x_1) \tag{2.11}$$

At the surface, the discontinuity in $\widetilde{\boldsymbol{D}_3}$ is related to the potential by the effective permittivity $\varepsilon_s(\beta)$, defined by [99]

$$\varepsilon_s(\beta) = \frac{\widetilde{D_{3+}} - \widetilde{D_{3-}}}{|\beta|\widetilde{\emptyset}(x_1)} \tag{2.12}$$

The effective permittivity thus gives the electrical behaviour of the interface between

the vacuum and the piezoelectric half-space. If the $\widetilde{\boldsymbol{D}_{3+}}$ and $-\widetilde{\boldsymbol{D}_{3-}}$ differ, there must be free charges present at the surface, implying the presence of electrodes. The charge densities on the upper and lower sides are respectively $\widetilde{\boldsymbol{D}_{3+}}$ and $-\widetilde{\boldsymbol{D}_{3-}}$**.** Hence, if the total charge density is $\tilde{\sigma}(x_1)$, equation (2.12) becomes [99]

$$\varepsilon_s(\beta) = \frac{\tilde{\sigma}(x_1)}{|\beta|\widetilde{\emptyset}(x_1)} \tag{2.13}$$

Where $\tilde{\sigma}(x_1)$ and $\widetilde{\emptyset}(x_1)$ are both proportional to *exp*[*j*(ωt+βx_1)]. This corresponds to the electrostatic case and the total charge density can be presented as the following equation [99]:

$$\tilde{\sigma}(x_1) = \widetilde{\sigma_+}(x_1) + \widetilde{\sigma_-}(x_1) = (\varepsilon_0 + \varepsilon_p)|\beta|\widetilde{\emptyset}(x_1) \tag{2.14}$$

In the above equations the potential $\widetilde{\emptyset}(x_1)$ and charge density $\tilde{\sigma}(x_1)$ are proportional to *exp*($j\omega t$), and the frequency ω was taken to be a constant throughout. If ω is changed the value of $\varepsilon_s(\beta)$ changes, so $\varepsilon_s(\beta)$ is a function of ω as well as β. However, $\varepsilon_s(\beta)$ is essentially the ratio of $\widetilde{\boldsymbol{D}_3}$ to $\widetilde{\boldsymbol{E}_1}$**,** as displayed by eq. (2.12), and it can be seen that it remains unchanged if ω and β are changed in proportion. Consequently, $\varepsilon_s(\beta)$ is a function of the normalized quantity β/ω. It has dimensions the same as the reciprocal of velocity. This method of analysis applies for a constant frequency, and the effective permittivity is written as $\varepsilon_s(\beta)$ without showing the frequency dependence definitely. A more general solution in terms of charge density $\sigma(x_1)$ and surface potential $\emptyset(x_1)$ is readily obtained by Fourier synthesis. Equation (2.13) can be solved and a general solution is given as [99],

$$\varepsilon_s(\beta) = \frac{\bar{\sigma}(\beta)}{|\beta|\bar{\emptyset}(\beta)} \tag{2.15}$$

Where $\bar{\sigma}(\beta)$ and $\bar{\emptyset}(\beta)$ are respectively the Fourier transforms of $\sigma(x_1)$ and $\emptyset(x_1)$**.** Thus, given a generic potential function $\emptyset(x_1)$**,** the relates charge density may be obtained by transforming it to $\bar{\emptyset}(\beta)$, and with a $\varepsilon_s(\beta)$ to obtain $\bar{\sigma}(\beta)$, and then transforming back to the x_1 domain. For the general solution the potential $\emptyset(x_1)$ and charge density $\sigma(x_1)$

are proportional to $exp(j\omega t)$, with the frequency ω regarded as a constant in the equation (2.15). In solving a particular problem it is usually found that the potential and charge density are functions of frequency, so their transforms $\bar{\sigma}(\beta)$ and $\overline{\emptyset}(\beta)$ will also be functions of frequency. In the Fourier transform, the frequency ω is held constant during the integration. The relationship given by the effective permittivity, equation (2.15), applies for all values of ω.

The above theory proves that surface acoustic wave (SAW) can be excited on the piezoelectric crystal or piezoelectric thin film by using the interdigital electrode pattern, or interdigital transducers (IDTs). This theory has been employed to design the mask of IDTs as show in figure 2.9. Adding electric potential between alternate connected electrodes causes a periodic electric field to be stimulated on the substrate. When applying the alternate voltage, a periodic strain filed is generated in the piezoelectric crystal so that produces a standing surface acoustic wave. Meanwhile, the wave front is parallel to the transducer fingers. The transducer operates most efficiently as the quarter SAW wavelength (λ_T) matches the periodic distance "d" of electrode. This happens when the transducer is excited at the synchronous frequency.

The relation of the velocity of the SAW (v_0) and the excited working frequency (f_0) is given by following equation [85]:

$$f_0 = \frac{v_0}{\lambda_T} = \frac{v_0}{4d} \tag{2.16}$$

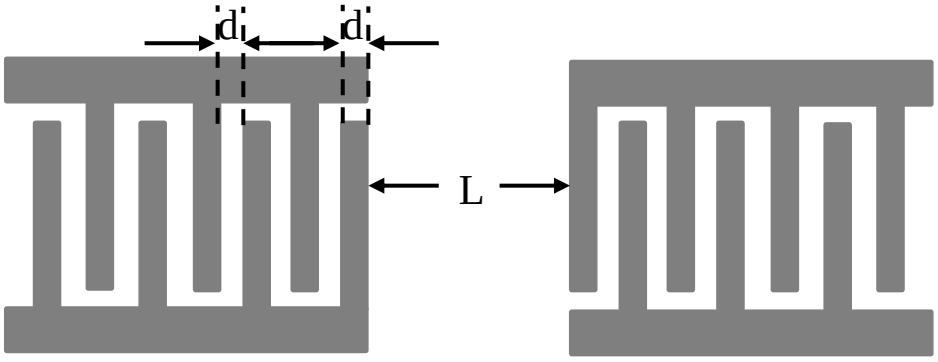

Figure 2.9 The design of IDTs mask. L is the propagation length and d is the width of

electrode and distance between two electrodes.

In addition, the propagation length (L) between two centres of the IDT pairs is called delay line. L influences the magnitude of the transmission power. The attenuation of the transmission power would rise with increasing L, so that shorter delay lines would prevent more power loss from transmitting signal. However, noise levels are reduced by increasing L. Φ_E is the related phase shift of the electronic circuit and $\omega L/v$ is the phase shift associated with the acoustic wave. Since the main source of the random noise is the small phase shift ($\delta\Phi_E$) in the electric circuit, the received signal frequency deviation can be expressed as [85]:

$$\frac{\delta f}{f} = -\frac{\lambda \delta \Phi_E}{2\pi L} \tag{2.17}$$

Each transducer finger may be considered to be a discrete source for the generation of surface acoustic wave in a piezoelectric medium because the piezoelectric stress varies with the position near each transducer finger. When the wave enters the receiving transducer, this potential induces a current flow in each transducer electrode. The combined current flow is detected by the external circuit. In relation to the bandwidth of an IDT frequency response, this will be narrower when increasing the number of finger pairs N. However, there is a limitation in the maximum N recommended, due to the fact that, in practice, when N exceeds 100, the losses associated with mass loading and the scattering from the electrodes increase [105]. This neutralizes any additional advantage associated with the increase of the number of the finger pairs.

2.3 Sensing theory of Love wave biosensors

In acoustic-wave sensor applications, one typically detects the change of wave velocity v and/or attenuation α that is induced as the device interacts with the surroundings [106, 107]. Changes in wave velocity and attenuation can be basically related to changes in wave energy density and power dissipation, respectively. With regard to wave velocity

changes, the power density P (power/area) carried by a wave correlates closely with the wave energy density U (energy/volume) stored in a lossless medium. Considering a wave propagates across a unit cube, the time for the wave through the cube is $\tau = 1/v$ (figure 2.10).

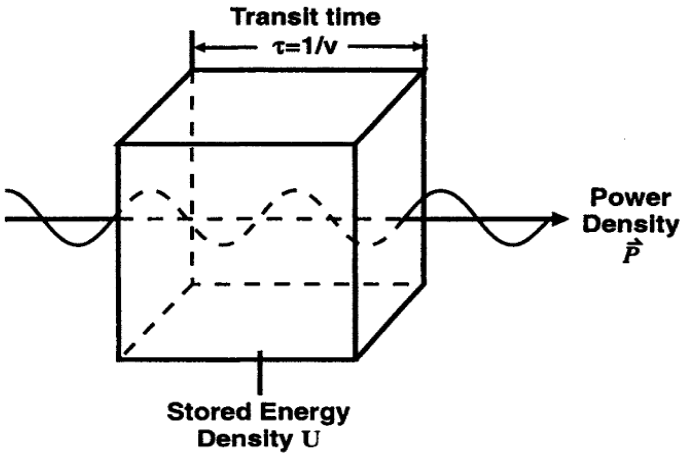

Figure 2.10 Energy stored per unit volume is dependent upon incident power flow and propagation velocity.

When the wave travels through the cube, the energy density in the cube increases by the incident power times the transit time: $U = P\tau = P/v$. Hence [107],

$$P = Uv \tag{2.18}$$

This relation can be used to explain how changes in wave energy density affect changes in wave velocity in a lossless medium; i.e., one in which P is constant. By differentiating equation (2.18) one obtains [107]:

$$\frac{\Delta v}{v_0} = \frac{-\Delta U}{U_0} \tag{2.19}$$

Where v_0 and U_0 indicate unperturbed propagation velocity and energy density respectively. Equation (2.19) represents an essential relation between wave velocity and energy density for a system excited at a given frequency: the fractional variation in wave velocity is equal to the negative of the fractional variation in wave energy density. It is reasonable if considering that in a system excited at a given frequency, the wave length alters so that the kinetic energy equals the peak potential energy of the wave. The effect is

that changes of the medium that influence the wave energy density will cause changes of the wave velocity. From equation (2.19), the fractional change is minus the fractional changes in mass density of the medium [107]:

$$\frac{\Delta v}{v_0} = \frac{-\Delta \rho}{\rho_0} \tag{2.20}$$

Because of a change of the wave velocity, the signal transit time through the sensing surface is altered and it leads to frequency or phase shift. Therefore, detecting signal frequency or phase shift can be used to measure the quantity of change on the sensing surface.

2.4 Fabrication of Love wave biosensors

Love wave sensors designed and realised in this work are constituted by a piezoelectric substrate (64°Y-X $LiNbO_3$), interdigital transducers (IDTs, 100pairs), a guiding layer (PMMA, thickness is 1156nm) and a rectangular sensing region (gold, thickness is 20nm, length is 5mm and width is 2mm, area is 10mm^2). The orientation angle of $LiNbO_3$ is 64° and refers to the sliced angle of the original wafer after a crystal is grown. Because different sliced angles will give a different atomic arrangement of the substrate (from the viewpoint of the Cartesian coordinate system), the resulting piezoelectric effect will not be the same. The sign "64°Y-X" means that the acoustic wave propagates along the x axis and the wafer sliced angle is 64° that is rotated from the y axis. The leaky SAW only can be excited at specific orientation angle of the lithium niobate crystal. In addition, the velocities of acoustic waves are not equal when they propagate at different orientation angles. The type of SAW and the velocity of acoustic waves are two major parameters when designing a Love wave biosensor. Therefore, it is important to use the correct orientation angle of the lithium niobate crystal and position the IDTs exactly. IDTs were deposited by lift-off photolithography in order to generate pure shear horizontal acoustic

waves propagating perpendicular to the X crystallographic axis. IDTs were composed of 100 Ti/Au (thickness are 10/100nm) split-finger pairs with a periodicity (λ) of 40μm. The acoustic path length, between both IDTs, was 200λ and the IDTs aperture was 100λ (4mm). The detail fabrication steps of the sensor were as following described [59].

(1) In order to ensure the surface of the substrate is clean and prevent small particles contaminate the element, substrate has to be cleaned at the first step. Typically contaminants are generated from these sources: dust from scribing or cleaving, atmospheric dust, abrasive particles, lint from wipers, photoresist residue from previous photolithography, bacteria or solvent residue. The standard cleaning process involves the following steps: i) the substrate was immersed in acetone with ultrasonic agitation for 5 minutes. ii) Then it was soaked in methanol with ultrasonic agitation for 5 minutes. iii) to immerse the substrate in DI water (deionized water) with ultrasonic agitation for 5 minutes. iv) after that, the substrate was rinsed under free flowing DI water then used clean nitrogen (N_2) stream to blow off dry for tools and the substrate. If the standard cleaning process cannot remove all contaminants on the substrate, RCA cleaning processes are considered to employ [108]. First step of RCA cleaning processes was to immerse the substrate in the special solution, which was composed of 5 parts of deionized water, 1 part of aqueous NH_4OH (ammonium hydroxide, 29% by weight of NH_3), and 1 part of aqueous H_2O_2 (hydrogen peroxide, 30%), at 75℃ for 10 minutes. This base-peroxide mixture removed organic residues and was also very effective in removing particles from the surface. However, this treatment resulted in the formation of a very thin oxide layer (about 10 Å) on the substrate surface, along with a certain degree of metallic contamination that shall be removed in subsequent steps. The second step was a short immersion in a 1:50 solution of HF + H_2O at 25℃ for about 15 seconds, in order to remove the thin oxide layer and some fraction of ionic contaminants. The third step was performed with a solution, which was composed of 5 parts of deionized water, 1 part of aqueous HCl (hydrochloric acid, 39% by

weight), and 1 part of aqueous H_2O_2 (hydrogen peroxide, 30%), at 75℃ for 10 minutes. This treatment effectively removed the remaining traces of metallic (ionic) contaminants, some of which were introduced in the first step. The last step was to rinse the substrate under free flowing DI water for 5 minutes then used clean nitrogen stream to blow off dry for tools and the substrate [109].

(2) The next step was to bake the sample at 95℃ for 3 minutes to remove moisture content on substrate surface to improve the adhesion of the photo resist.

(3) Then the sample was held on a spinner chuck by vacuum and coated the prepared sample with S1818 positive photoresist layer with the spinner rotating rate of 4000 rpm for 30 seconds. The reasons to use S1818 are: i) this kind of positive photoresist provides high resolution in photolithography technology and has been engineered to satisfy the microelectronics industry's requirements for advance device fabrication. The adhesion and coating uniformity were excellent; ii) it was optimized for G-Line exposure and was suitable for operating by Suss MA6 contact mask aligner. The thickness of the photoresist could be measured by surface profilometry Dektak 6. The result was a uniform thickness of 1.9μm S1818 layer attached on the substrate.

(4) The next process was soft bake, which was used to evaporate the coating solvent and to densify the resist after spin coating. The sample was baked on hot plate at 95℃ for 10 minutes. Hot plating the resist was usually faster, more controllable, and does not trap solvent like convection oven baking.

(5) Before exposure process, the sample was soaked in standard developer (Microposit developer MicroDEV concentrate: H_2O 1:1) for 60 seconds [110]. According to the previous investigations [111, 112], this process modified the top surface of the photoresist by removing short-chain molecules and forming long-chain, high molecular weight

molecules. It could increase hydrophobicity of the near-surface layer imparted by alkaline based developer incorporation. This treatment reduced development rate of the surface layer, whilst the resist beneath developed at the normal rate, therefore resulting in an undercut profile after development. This method was experimentally proven to increase the yield of qualified devices. Then the sample was loaded into mask aligner (MA6) which was mounted the photo mask (the IDTs patterns were on the chrome mask, which was Cr on soda lime glass) to expose the sample for 5 seconds.

(6) After that, the sample was developed in the standard developer solution for 75 seconds. Subsequently, the sample was immersed under D.I. water for 60 seconds to fix the pattern. Then the sample was dried by clean nitrogen (N_2) stream. The surface profile of the sample after development was observed by Dektak 6 and displayed in figure 2.11.

(7) The next step was to evaporate metal layer on the sample. The gold (Au) was chosen for the main material to construct the IDTs patterns due to its high conductivity and is one of the least reactive chemical elements, which can prevent reaction with target specimens in biosensor application. Because the adhesion between gold and lithium niobate is not very good, thin titanium (Ti) layer should be deposited first on the substrate to increase the adhesion of metal IDTs on the lithium niobate substrate. The deposition thickness of Ti and Au were 10nm and 100nm, respectively. This process was operated by the metallization system (Plassys MEB 550S Electron Beam Evaporator).

(8) Then the sample was soaked in acetone for 30 minutes to lift off the undesired metal on the substrate and the sample is dried by N_2 stream again. The profile of the sample after metallization and lift off was also observed by Dektak 6 and displayed in figure 2.12.

(9) Then a PMMA layer was coated on the substrate as a “Love wave” guiding layer for the sensor. The thickness of the PMMA layer was controlled by the spin coating between

1μm and 1.5μm to optimize the sensitivity of the device. Another important issue was to open the window (remove partial PMMA) on the signal metal contact pad for signal wire connection.

(10) The next step was to establish a sensing area on the devices. A gold thin film with thickness 20nm was deposited upon the PMMA layer between IDTs pairs and its area was 10mm^2 (its length is 5mm and its width is 2mm). A narrow gap with 100μm width on the gold sensing area between IDTs was also arranged to provide another function to detect the impedance of specimen.

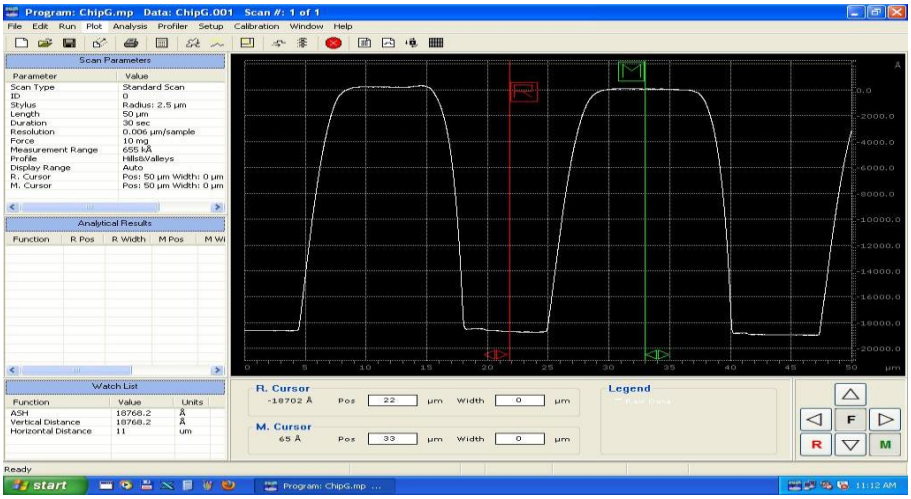

Figure 2.11 The surface profile of the sample after development. The interdigital patterns are shown as periodical gaps in the profile and their width are about 10μm. The thickness of residual photoresist is approximately 1.9μm.

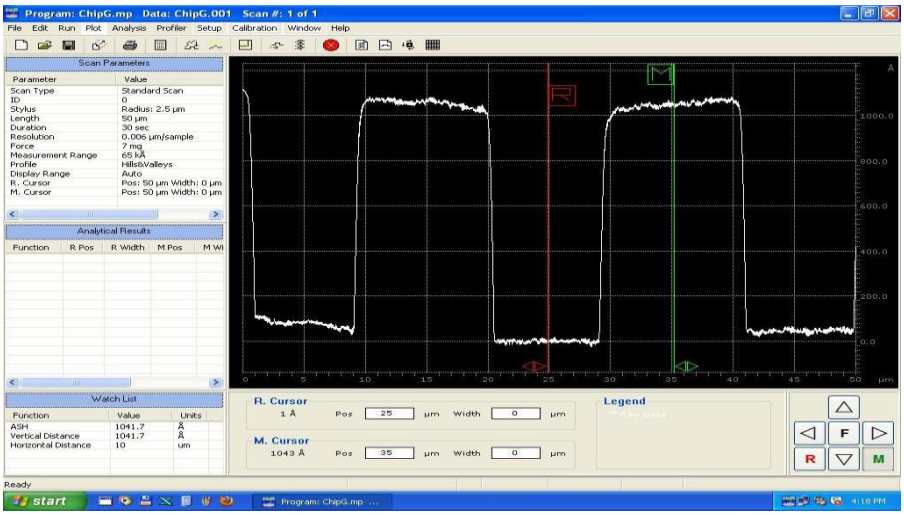

Figure 2.12 The profile of the sample after metallization and lift off. The interdigital patterns are shown as periodical gaps in the profile and their width are about 10μm. The thickness of the metal IDTs is approximately 104nm.

From the effectively performed processing, two critical points were discovered and are briefly summarized here. They are partially base on the pictures taken during the processing and reported in figure 2.13. One critical point is the cleaning of the substrate. Although residues from the cleaning are scarce, their influence on the production process is dramatic and generally results in the discard of the processed wafer. The other critical point is that without the treatment of soaking samples in the standard developer before exposure and it causes some problems at the edges of patterns when gold lift-off. The realized Love wave sensor is displayed in figure 2.14. The flow chart of manufacture process of the sensor is shown in figure 2.15.

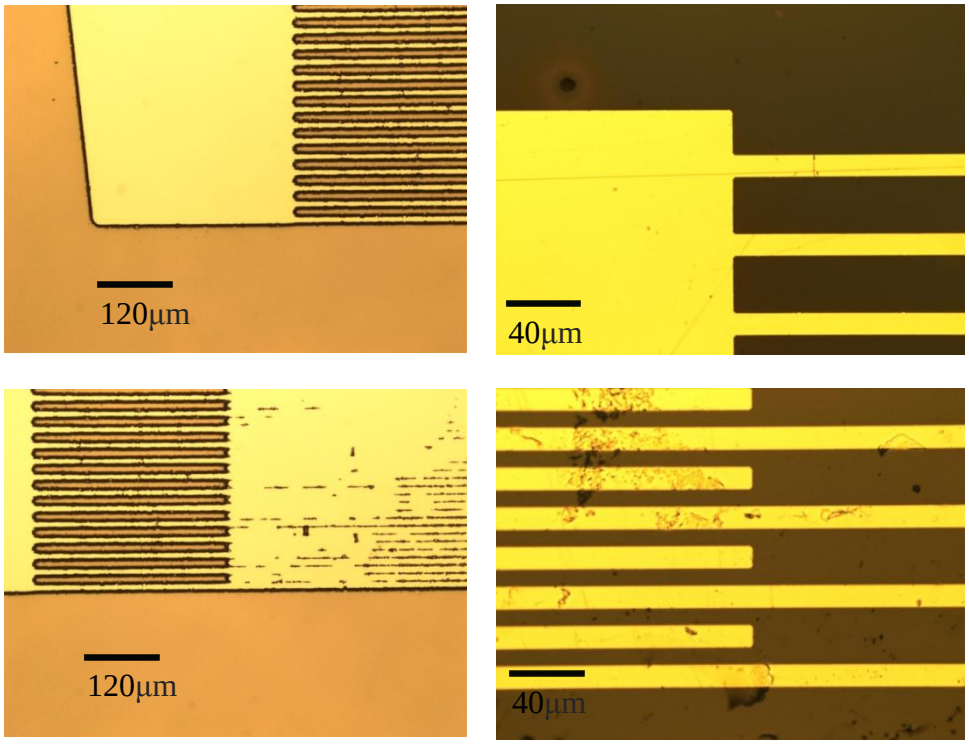

Figure 2.13 (Left) the resist can stick to the mask (hard-contact photolithography) and damage the patterns. Without treatment of pre-soaking samples in the standard developer causes some problems at the edges of patterns when gold lift-off. (Right) Well patterned structures have the same width and are equally spaced.

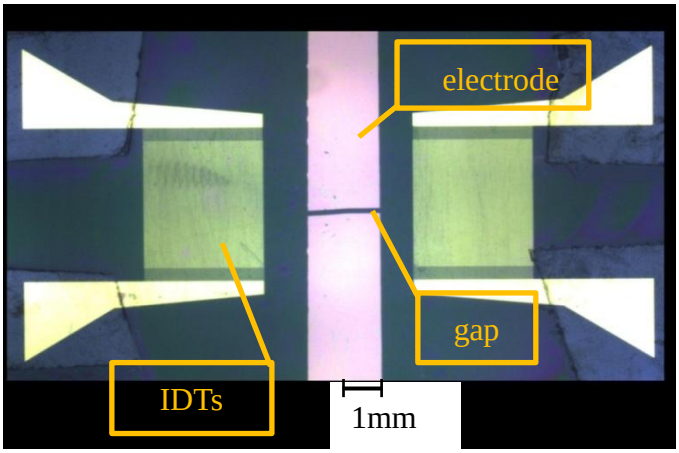

Figure 2.14 The picture of the realized Love-wave sensor in this study.

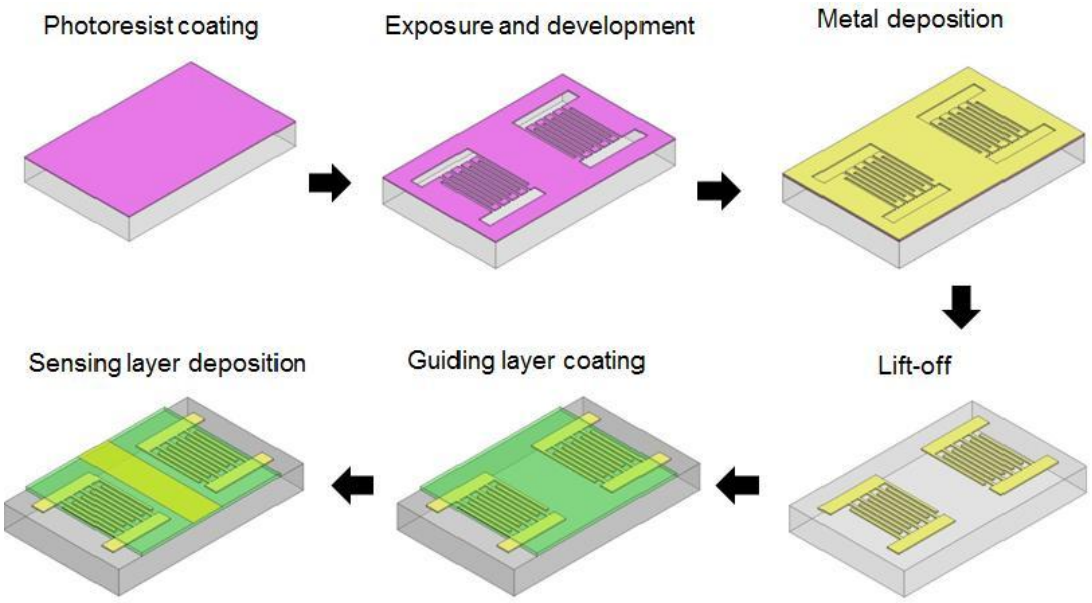

Figure 2.15 The flow chart of manufacture processes of the sensor.

2.5 Measurement Setup

The basic configuration of a two-port Love-wave sensor is illustrated in figure 2.16 [51]. This structure operates as an electronics delay line device. D is the distance between input and output IDT. L is the centre-to-centre distance between the IDTs. W is the length of the electrodes in the IDTs. Thus, the sensor is a transmission line which transmits a mechanical signal (acoustic wave) launched by the input port (input IDT) due to the applied radio frequency (RF) electrical signal. After a time delay the traveling mechanical wave is converted back to an electric signal in the output port (output IDT). In general,

changes in the coating layer and/or in the semi-infinite fluid medium produce variations in the acoustic wave properties (wave propagation velocity, amplitude or resonant frequency). These variations can be measured comparing the input and output electrical signal, since phase V_{in} remains unchanged, while phase V_{out} changes. Consequently, from an electric point of view, a Love-wave delay line can be defined by its transfer function $H(f) = V_{out}/V_{in}$, which represents the relationship between input and output electrical signal. $H(f)$ is a complex number which can be defined as $H(f)=Ae^{j\Phi}$, being A the amplitude ($|V_{out}/V_{in}|$) and Φ the phase shift between V_{in} and V_{out}. For biosensors application, biochemical interactions at the sensing area will modify the thickness and properties of the coating, and therefore variations in the amplitude and phase of the electrical transfer function can be measured. These variations can be monitored in real time, which provides valuable information about the interaction process.

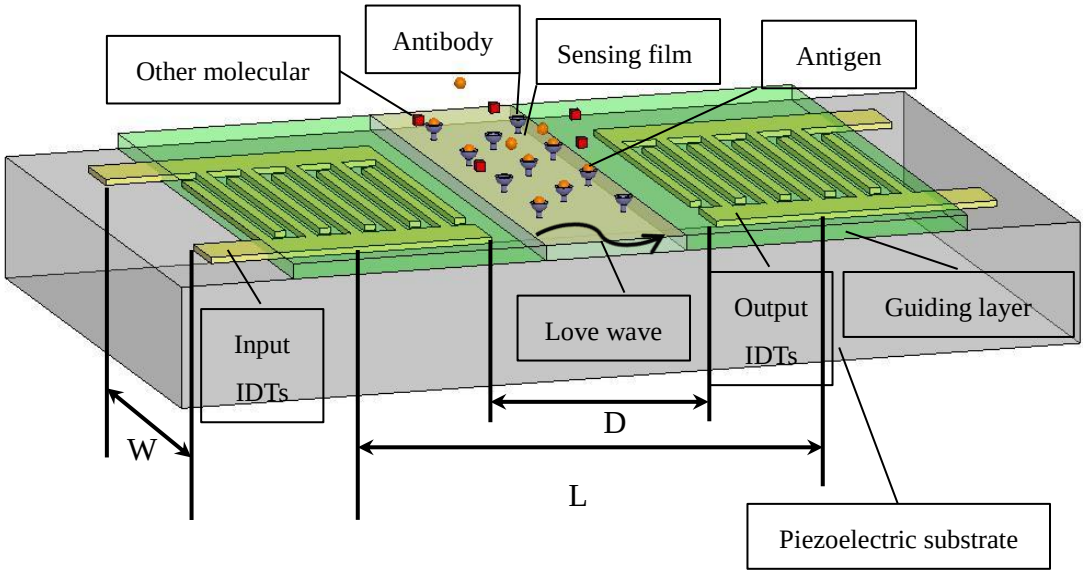

Figure 2.16 The configuration of a two-port Love-wave sensor. It is a delay line structure. RF signal is applied to the input IDTs which launches an acoustic propagating wave and the output signal is recorded at the output IDTs. D is the distance between input and output IDT. L is the centre-to-centre distance between the IDTs. W is the length of the electrodes in the IDTs.

There are two methods to measure the signal change of the Love wave delay line devices. One is to combine with other electronic elements to set up an active electrical device (close loop configuration). The other is using passive way to measure signal directly

by connecting with network analyser (open loop configuration). The Love wave delay line can be used as frequency determining element in closed loop configuration to form an oscillator circuit. In an oscillator circuit the Love wave device is placed as a delay line in the feedback loop of an RF amplifier in a closed loop configuration [113, 114]. Therefore, a change in the wave velocity, due to a sensing effect, produces a time delay in the signal through the Love wave device which appears as phase-shift that is transferred in terms of frequency-shift in an oscillator configuration. The advantages of the oscillator configuration are the low cost of their circuitry as well as the integration capability and it can be applied in continuous monitoring surroundings. These reasons make the oscillators an attractive configuration for the monitoring of the determining parameter of the resonator sensor, which in the case of the Love wave device is the phase-shift of the signal at resonance [54, 57, 58]. However, in my opinion, the oscillators are not the best option for acoustic wave sensor characterization due to the following disadvantages: First, they do not provide direct information about signal amplitude. Second, they maybe stop oscillation if insertion losses exceed the amplifier gain during an experiment. Third, despite of the apparent simple configuration, a very good design is necessary to guarantee that a Love wave resonator will operate at a specific frequency, and this is not a simple task. In effect, in the same way as in QCM oscillators it is required to assure that the sensor resonates on one defined resonance mode and does not "jump" between spurious resonances [115], in Love wave oscillators one must assure that the sensor will operate at one phase ramp in the sensor response band-pass, and does not jump from one to another which are almost of identical characteristics. Moreover, when the resonator dimensions get smaller and the frequency increases this becomes more difficult to achieve, since when increasing frequency there is a decrease of the resonator quality factor, a decrease in frequency stability [116] and in Love wave the ramps become nearer to each other. On the other hand, the passive way measurement works in an open loop configuration. The input transducer is excited at a fixed frequency while the phase shift between V_{out} and V_{in}, Φ, is recorded. In

this configuration, in the absence of interferences, frequency variations measured experimentally can be related to changes in the physical properties of the layers deposited over the sensing area. Network analysers are the most commonly used instrumentation for characterizing Love-wave sensors in a passive way measurement as shown in figure 2.17. The result of the control experiment which there is no any test specimen on the sensing area is shown in figure 2.18. The frequency spectrum of interest is in the region between 115 MHz and 118 MHz. The peak frequency of the Love-wave sensor reaches 116.466 MHz, its insertion loss is -15.67 dB and the phase is -84.35 degree.

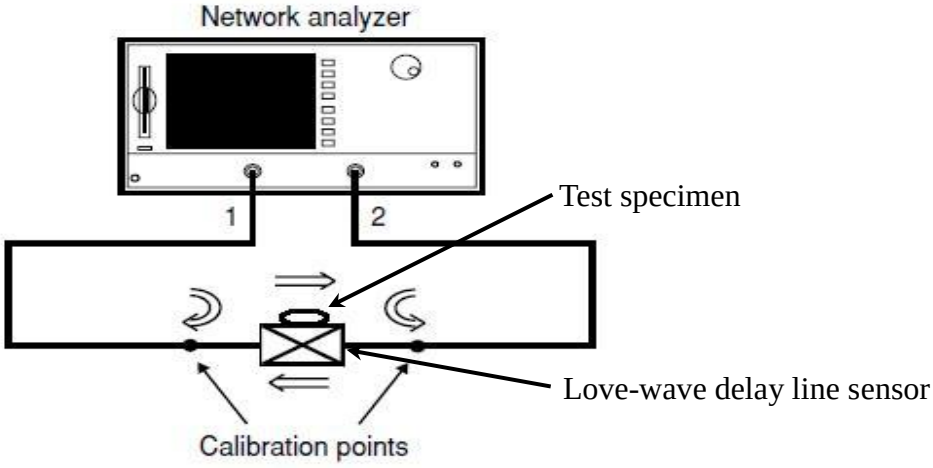

Figure 2.17 figuration of passive way to measure characters of Love-wave sensor. The parameters which are recorded are frequency response to insertion loss (IL, the S_{22} parameters) and phase.

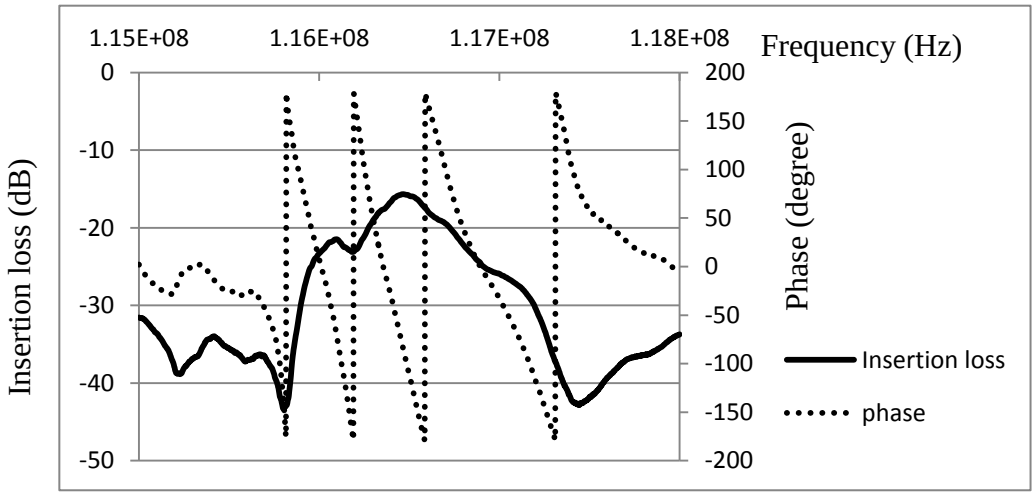

Figure 2.18 The result of the control experiment of the Love-wave sensor in this study. The frequency response of insertion loss (solid line) and phase (dotted line) were measured by using a network analyser.

In this study, frequency signals were used for sensing measurement. Although some previous researchers used phase signal for sensing applications [114] and the sensitivities of outcomes were satisfied, other researchers presented the disadvantage of the phase signals measurement and suggested to use frequency signals measurement [113]. The main disadvantage of phase signals measurement is the limit of phase system. When the signal waveform changes in a cyclic manner, one cycle waveform is defined as 360º. Hence, phase shift would be limit in the range between 0º and 360º (or from -180º to 180º), which would cause a problem when compared with results of measurements. For example, if two phase values, 43º and 56º, were observed respectively. The phase shift could not be simply determined as 13º from the equation "56º minus 43º" because there may be more than a cycle between these two values. In contrast, there is no similar question in frequency signal measurements.

2.5.1 S-parameter measurement with vector network analyser

The parameters of the result that signal is recorded by network analyser is S-parameters [117]. The reasons why S-parameters are measured with the vector network analyser are as follows [118]: At high frequencies, it is very hard to measure total voltage and current at the device ports. One cannot simply connect a voltmeter or current probe and obtain accurate measurements due to the impedance of the probes themselves and the difficulty of placing the probes at the desired positions. S-parameters have many advantages over the other parameters, such as H, Y or Z-parameters. "H-parameters" are also called as "hybrid parameters", which represent input resistance, reverse voltage gain, forward current gain, and output conductance in a two-port network. "Y-parameters" are also called as "admittance parameters", which means the input/output admittance relationship of the devices. "Admittance parameters" describe the behaviour of any linear electrical network which can be regarded as a black box with a number of ports. A port in this context is a pair of electrical terminals carrying equal and opposite currents into and

out-of the network, and having a particular voltage between them. The “Z-parameters” which are also called as impedance parameters describe the impedances of a device with open output ports. To measure H, Y or Z-parameters needs to know the exact current or voltage through the device and this is difficult to implement on high-frequency networks measurement. Therefore, that is why S-parameters (scattering parameters) were developed. S-parameters are defined in terms of voltage traveling waves, which are relatively easy to measure. S-parameters don’t require connection of undesirable loads to the device under test. The measured S-parameters of multiple devices can be cascaded to predict overall system performance. If desired, H, Y, or Z-parameters can be derived from S-parameters. And very important for RF design, S-parameters are easily imported and used for circuit simulations in electronic-design automation (EDA) tools. Also, S-parameters are the shared language between simulation and measurement [119]. An N-port device has N^2 S-parameters. Hence, a two-port device has four S-parameters. The numbering convention for S-parameters is that the first number following the “S” is the port where the signal comes out, and the second number is the port where the signal is applied. For example, S_{21} is a measure of the signal coming out port 2 relative to the RF stimulus entering port 1. When the numbers are the same (e.g., S_{11}), it indicates a reflection measurement, as the input and output ports are the same. The incident terms (a_1, a_2) and output terms (b_1, b_2) represent voltage traveling waves. The concept of S-parameters is displayed in figure 2.19.

S_{11} and S_{21} are determined by measuring the magnitude and phase of the incident, reflected and transmitted voltage signals when the output is terminated in a perfect Zo (a load that equals the characteristic impedance of the test system). This condition guarantees that a_2 is zero, since there is no reflection from an ideal load. S_{11} is equivalent to the input complex reflection coefficient or impedance of the device under test (DUT), which is a Love wave biosensor, and S_{21} is the forward complex transmission coefficient. Likewise, by placing the source at port 2 and terminating port 1 in a perfect load (making a_1 zero),

S_{22} and S_{12} measurements can be made. S_{22} is equivalent to the output complex reflection coefficient or output impedance of the biosensor. S_{12} is the reverse complex transmission coefficient. Figure 2.20 illustrates the method how to measure S-parameters of a two port device.

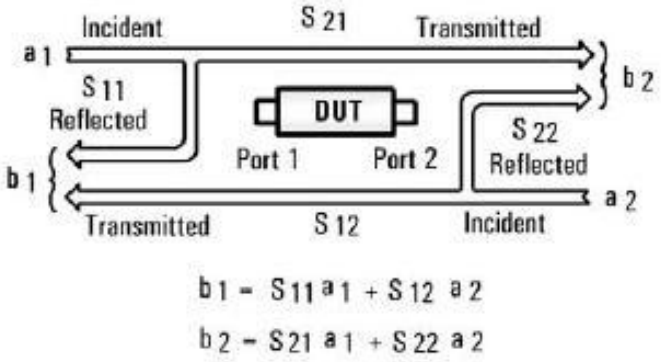

Figure 2.19 The concept of S-parameters. The signal input from port 1 is a_1. The signal input from port 2 is a_2. The signal output from port 1 is b_1. The signal output from port 2 is b_2. S_{11} is a measure of the signal coming out port 1 relative to the RF stimulus entering port 1. S_{21} is a measure of the signal coming out port 2 relative to the RF stimulus entering port 1. S_{12} is a measure of the signal coming out port 1 relative to the RF stimulus entering port 2. S_{22} is a measure of the signal coming out port 2 relative to the RF stimulus entering port 2.

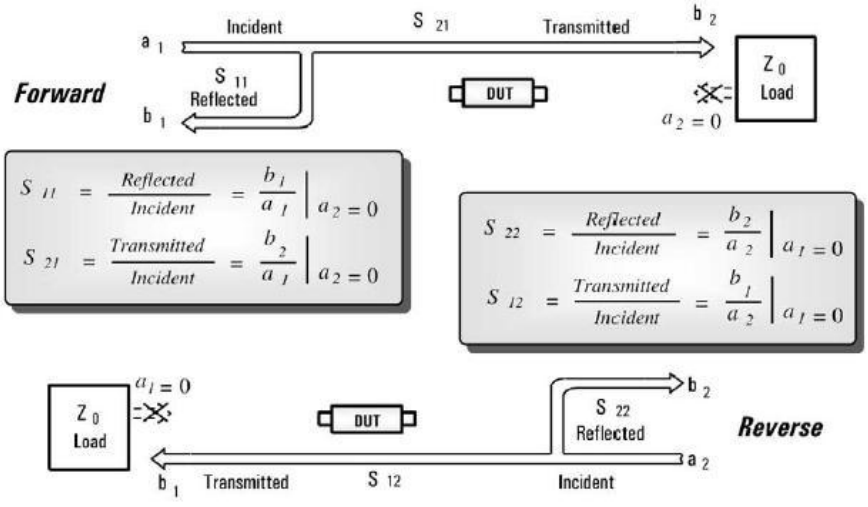

Figure 2.20 The method of S-parameters measurement. Applying a perfect load (a load that equals the characteristic impedance of the test system) on port 2 makes a_2=0. Then input a fixed signal a_1 and detect the output signal b_1 and b_2, which can calculate S_{11} and S_{21}, respectively. S_{22} and S_{12} can be obtained by a similar way to connect port 1 with a perfect load makes a_1=0, input a fixed signal a_2 and detect the output signal b_1 and b_2.

The figure 2.21 shows the essential parts of a typical 2-port vector network analyser. The signal source supplies the stimulus for this stimulus-response test system. The network analyser can sweep the frequency of the source and sweep its power level. Then the signal separation hardware provides two functions. The first function is to measure a portion of the incident signal to provide a reference for rationing. The second function is to separate the incident (forward) and reflected (reverse) traveling waves at the input of the DUT. The next portion of the network analyser is the signal detection block. The tuned-receiver approach is used in our vector network analyser. The tuned receiver uses a local oscillator (LO) to mix the RF down to a lower intermediate frequency (IF). The LO is either locked to the RF or the IF signal so that the receivers in the network analyser are always tuned to the RF signal present at the input. The "IF signals" is bandpass filtered which narrows the receiver bandwidth and greatly improves sensitivity and dynamic range. Analog-to-digital (ADC) and digital-signal processing (DSP) are used in the network analyser to extract magnitude and phase information from the IF signal. The last major block of hardware in the network analyser is the display/processor section. This is where the reflection and transmission data is formatted in ways that make it easy to interpret the measurement results.

The accuracy of S-parameter measurements depends greatly on how good a termination the researchers apply to the load port (the port not being stimulated). Anything other than a perfect load will result in a_1 or a_2 not being zero (which violates the definition for S-parameters). In cases where the biosensor was connected to the test ports of a network analyser without a perfect test-port match, I have not done a very good job satisfying the optimal conditions for a termination. For this reason, two-port error correction, which corrects for source and load match, is very important for accurate S-parameter measurements. Thus, the thru-reflect-line (TRL) calibration needs to be used in this study to improve the result of the measurement.

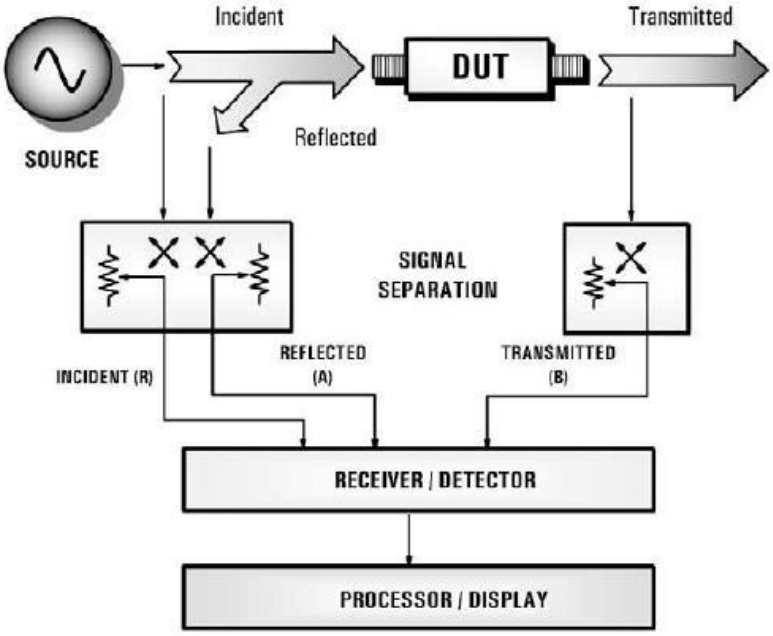

Figure 2.21 The essential structure of a network analyser. The test signal is generated by a variable frequency continuous wave source and level adjustment can tune its power level. Signal separation switches can determine the direction of the test signal flow. When switch chooses the signal flow from incident transmitted, the system can measure S_{11} and S_{21}. When the detection signal is from incident to reflected, the system can measure S_{22} and S_{12}. Receiver and detector are working with the same reference oscillator, and they can compare the received signal with the reference signal to obtain the amplitude and phase of the signal at the test frequency. The processor can conduct and control the mathematical processing and deal with the output (phase and amplitude) display.

2.5.2 TRL (through-reflect-line) calibration

As a further application of signal flow graphs I consider the calibration of a network analyser using the thru-reflect-line (TRL) technique [120]. The general problem is shown in Figure 2.23 [121], where it is intended to measure the S-parameters of a two port device at the indicated reference planes. As discussed in the previous point of interest, a network analyser measures S-parameters as ratios of complex voltage amplitudes. The primary reference plane for such measurements is generally at some point within the analyser itself, so the measurement will include losses and phase delays caused by the effects of the connectors, cables, and transitions that must be used to connect the device under test (DUT)

to the analyser. In the block diagram of Figure 2.22 these effects are lumped together in a two-port error box placed at each port between the actual measurement reference plane and the desired reference plane for the two-port DUT. A calibration procedure is used to characterize the error boxes before measurement of the DUT; then the actual error-corrected S-parameters of the DUT can be calculated from the measured data. Measurement of a one-port network can be considered as a reduced case of the two-port case.

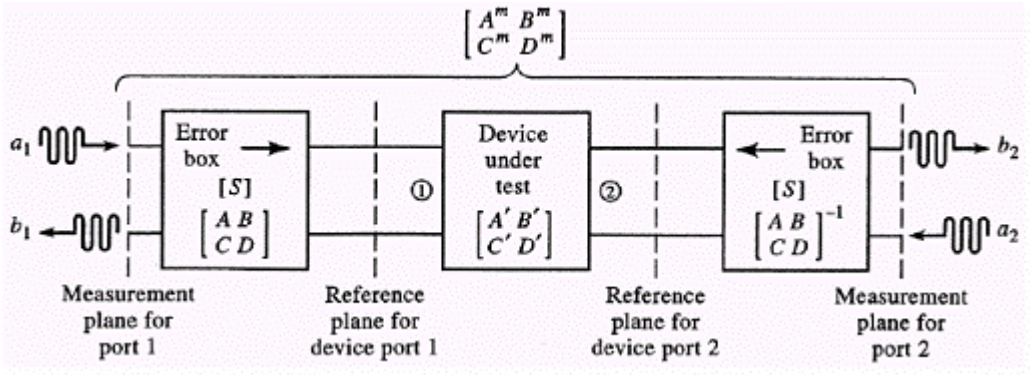

Figure 2.22 Block diagram of a network analyser measurement of a two-port device.

The simplest way to calibrate a network analyser is to use three or more known loads, such as shorts, opens, and matched loads. The problem with this approach is that such standards are always imperfect to some degree, and therefore introduce errors into the measurement. These errors become increasingly significant at higher frequencies and as the quality of the measurement system improves. The TRL calibration scheme does not rely on known standard loads, but uses three simple connections to allow the error boxes to be characterised completely. These three connections are shown in Figure 2.23. The "thru" connection was made by directly connecting port 1 to port 2, at the desired reference planes. The "reflect" connection used a load having a large reflection coefficient, Γ_L, such as a nominal open or short. It is not necessary to know the exact value of Γ_L, as this will be determined by the TRL calibration procedure. The "line" connection involved connecting ports 1 and 3 together through a length of matched transmission line. It was not necessary to know the length of the line, and it was not required that the line be lossless; these

parameters will be determined by the TRL procedure.

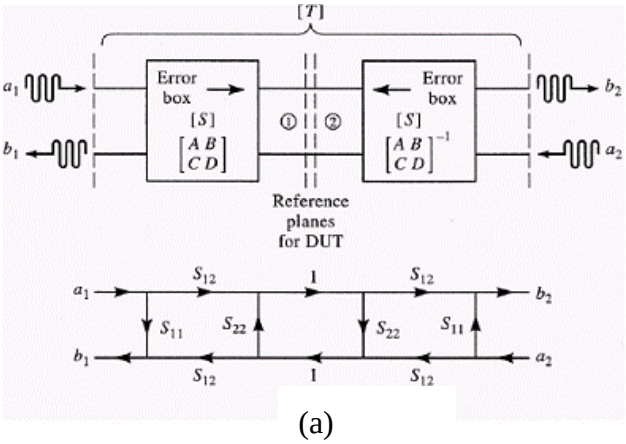

(a)

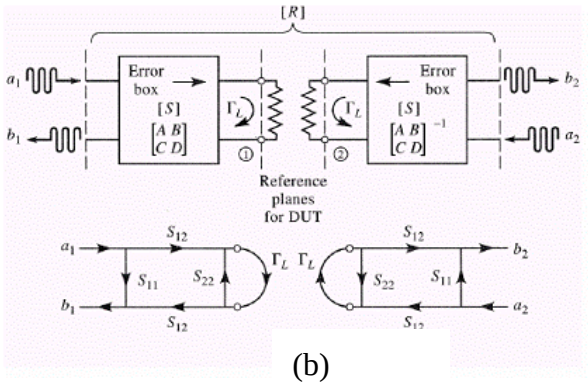

(b)

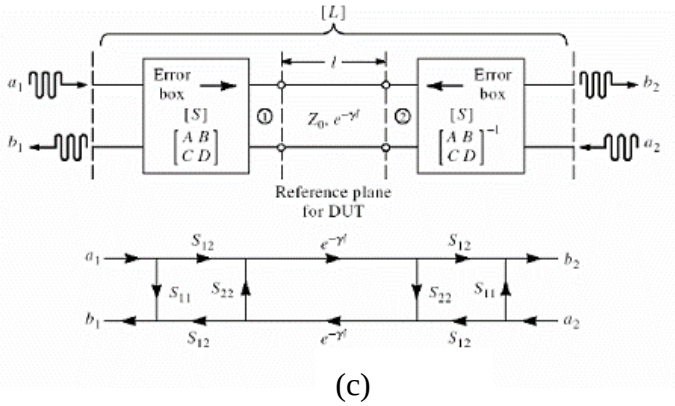

(c)

Figure 2.23 (a) Block diagram and signal flow graph for the thru connection (b) Block diagram and signal flow graph for the reflect connection (c) Block diagram and signal flow graph for the line connection [121].

In the TRL calibration procedure, signal flow graphs will be used to derive the set of equations to find the S-parameters for the error boxes. With reference to Figure 2.23, “thru”, “reflect”, and “line” were applied to the connections at the reference plane for the

biosensor, and measured the S-parameters for these three cases at the measurement planes. For simplicity, I assumed the same characteristic impedance for ports 1 and 2, and that the error boxes were reciprocal and identical for both ports. The error boxes were characterised by the S-matrix [S], and alternatively by an ABCD matrix. The ABCD matrix is also known as a Ray transfer matrix, which is a type of ray tracing technique used in the device network system. ABCD matrices involve the construction of a signal transfer matrix which describes the two port network system. Thus the relation $S_{21}=S_{12}$ was obtained for both error boxes, and an inverse relation between the ABCD matrices of the error boxes for ports 1 and 2, since they were symmetrically connected as shown in the figure. To avoid confusion in notation I will denote the measured S-parameters for the "thru", "reflect", and "line" connections as the [T], [R], and [L] matrices, respectively. Figure 2.23(a) shows the arrangement for the "Thru" connection and the corresponding signal flow graph. Observe that I have made use of the fact that $S_{21}=S_{12}$ and that the error using the decomposition rules to give the measured S-parameters at the measurement plane in terms of the S-parameters of the error boxes as [121]:

$$T_{11} = \frac{b_1}{a_1}|_{a_2=0} = S_{11} + \frac{S_{22}S_{12}^2}{1 - S_{22}^2} \tag{2.18}$$

$$T_{12} = \frac{b_1}{a_2}|_{a_1=0} = \frac{S_{12}^2}{1 - S_{22}^2} \tag{2.19}$$

By symmetry I have $T_{22}=T_{11}$, and by reciprocity I have $T_{21}=T_{12}$.

The reflect connection is shown in Figure 2.23(b), with the corresponding signal flow graph. Note that this arrangement effectively decouples the two measurement ports, so $R_{21}=R_{12}=0$. The signal flow graph can be reduced to show that [121]:

$$R_{11} = \frac{b_1}{a_1}|_{a_2=0} = S_{11} + \frac{S_{12}^2\Gamma_L}{1 - S_{22}\Gamma_L} \tag{2.20}$$

Because of symmetry $R_{22}=R_{11}$. The Line connection is shown in Figure 2.23(c), with the corresponding signal flow graph. A reduction similar to that used for the thru case gives [121]:

$$L_{11} = \frac{b_1}{a_1}|_{a_2=0} = S_{11} + \frac{S_{22}S_{12}^2 e^{-2\gamma l}}{1 - S_{22}^2 e^{-2\gamma l}} \quad (2.21)$$

$$L_{12} = \frac{b_1}{a_2}|_{a_1=0} = \frac{S_{12}^2 e^{-\gamma l}}{1 - S_{22}^2 e^{-2\gamma l}} \quad (2.22)$$

Because of symmetry and reciprocity $L_{22}=L_{11}$ and $L_{21}=L_{12}$.

Above equations (2.18) – (2.22) have the five unknowns S_{11}, S_{12}, S_{22}, Γ_L, and $e^{-\gamma l}$; the solution is straightforward. Since equation (2.20) is the only one that contains Γ_L, the four equations in (2.18), (2.19), (2.21), and (2.22) can be solved for the other four unknowns. Equation (2.19) can be used to eliminate S_{12} from (2.18), (2.21), and (2.22), and then S_{11} can be eliminated from (2.18) and (2.21). This leaves two equations for S_{22} and $e^{-\gamma l}$ [121]:

$$L_{12}e^{-2\gamma l} - L_{12}S_{22}^2 = T_{12}e^{-\gamma l} - T_{12}S_{22}^2 e^{-\gamma l} \quad (2.23)$$

$$e^{-2\gamma l}(T_{11} - S_{22}T_{12}) - T_{11}S_{22}^2 = L_{11}(e^{-2\gamma l} - S_{22}^2) - S_{22}T_{12} \quad (2.24)$$

Equation (2.23) can now be solved for S_{22} and substituted into (2.24) to give a quadratic equation for $e^{-\gamma l}$. Application of the quadratic formula then gives the solution for $e^{-\gamma l}$ in terms of the measured TRL S-parameters [121]:

$$e^{-\gamma l} = \frac{L_{12}^2 + T_{12}^2 - (T_{11} - L_{11})^2 \pm \sqrt{[L_{12}^2 + T_{12}^2 - (T_{11} - L_{11})^2]^2 - 4L_{12}^2 T_{12}^2}}{2L_{11}T_{12}} \quad (2.25)$$

The choice of sign can be determined by the requirement that the real and imaginary parts of γ be positive, or by knowing the phase of Γ_L to within 180°. Next to multiply (2.18) by S_{22} and subtract from (2.19) to obtain [121]:

$$T_{11} = S_{11} + S_{22}T_{12} \quad (2.26)$$

And similarly multiply (2.21) by S_{22} and subtract from (2.22) to get [121]:

$$L_{11} = S_{11} + S_{22}L_{12}e^{-\gamma l} \quad (2.27)$$

Eliminating S_{11} from the above two equations gives S_{22} in terms of $e^{-\gamma l}$ [121]:

$$S_{22} = \frac{T_{11} - L_{11}}{T_{12} - L_{12}e^{-2\gamma l}} \quad (2.28)$$

Solving (2.26) for S_{11} gives [121]:

$$S_{11} = T_{11} - S_{22}T_{12} \quad (2.29)$$

And solving (2.22) for S_{12} gives [121]:

$$S_{12}^2 = T_{12}(1 - S_{22}^2) \quad (2.30)$$

Finally, equation (2.20) can be solved for Γ_L to give [121]:

$$\Gamma_L = \frac{R_{11} - S_{11}}{S_{12}^2 + S_{22}(R_{11} - S_{11})} \tag{2.31}$$

Equations (2.25) and (2.28) – (2.31) give the S-parameters for the error boxes, as well as the unknown reflection coefficient, Γ_L (to within the sign), and the propagation factor, $e^{-\gamma l}$. Then the calibration procedure relies on the TRL method could be completed.

The S-parameters of the DUT can now be measured at the measurement reference planes shown in figure 2.22, and corrected using the above TRL error box parameters to a cascade of three two-port networks, it is convenient to use ABCD parameters. Thus, the error box S-parameters of the cascade is converted to the responding $A^mB^mC^mD^m$ parameters. If A'B'C'D' is used to denote the parameters for the DUT, then the matrix be obtained [121]:

$$\begin{bmatrix} A^m & B^m \\ C^m & D^m \end{bmatrix} = \begin{bmatrix} A & B \\ C & D \end{bmatrix} \begin{bmatrix} A' & B' \\ C' & D' \end{bmatrix} \begin{bmatrix} A & B \\ C & D \end{bmatrix}^{-1} \tag{2.32}$$

From which I can determine the ABCD parameters for the DUT as [121]:

$$\begin{bmatrix} A' & B' \\ C' & D' \end{bmatrix} = \begin{bmatrix} A & B \\ C & D \end{bmatrix}^{-1} \begin{bmatrix} A^m & B^m \\ C^m & D^m \end{bmatrix} \begin{bmatrix} A & B \\ C & D \end{bmatrix}^{-1} \tag{2.33}$$

The practical TRL kits applied in this study are displayed in figure 2.24. After connecting TRL kits with network analyser and operating the TRL calibration function which is set in the instrument, it successfully eliminates the losses and phase delays caused by the connectors, cables, and transitions. Therefore, the results of measurement of the Love-wave sensors can present the true characteristics of the devices themselves.

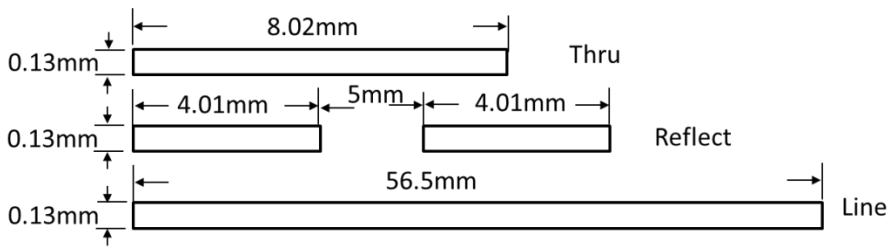

Figure 2.24. The practical TRL kits applied in this study. These kits are metal patterns on the 64° Y-X $LiNbO_3$ substrate. The dimensions of these kits were calculated with the software "Microwave Office®". The parameters that influence the dimensions used in software were as follows: the permittivity (85) of the material, thickness of the substrate (0.5 mm), working frequency of the device (115 MHz), and the metal was gold with thickness 100 nm.

2.5.3 Impedance matching between measuring instrument and Love wave biosensors

The reasons why they are important to do impedance matching when connect the sensors to the measurement instrument are as follows:

1. Maximum power is delivered when the load (sensor) is matched to the line (cable from the instrument), and power loss in the feed line is minimised.
2. Impedance matching can improve the signal-to-noise ratio of the system.
3. Impedance matching in a power distribution network will reduce amplitude and phase errors.

The fundamental concept of impedance matching is displayed in Figure 2.25, which shows an impedance matching network placed between a load impedance and a transmission line [121]. The matching network is ideally lossless, to avoid unnecessary loss of power, and is usually designed so that the impedance seen looking into the matching network is Z_0. Then reflections are eliminated on the transmission line to the left of the matching network, although there will be multiple reflections between the matching network and the load. This procedure is also referred to as tuning.

Figure 2.25 A lossless network matching an arbitrary load impedance to a transmission line.

As long as the load impedance, Z_L, has some non-zero real part, a matching network can always be found. Factors that may be important in the selection of a particular matching network include the following:

1. Complexity: As with most engineering solutions, the simplest design that satisfies the required specifications is generally the most preferable. A simpler matching network is usually cheaper, more reliable, and less lossy than a more complex design.

2. Bandwidth: Any type of matching network can ideally give a perfect match that means zero-reflection at a single frequency. In this application, however, it is desirable to match a load over a band of frequencies and the ways of doing this with a corresponding increase in complexity.
3. Implementation: Depending on the type of transmission line or waveguide being used, one type of matching network may be preferable compared to another.
4. Adjustability: In some applications the matching network may require adjustment to match variable load impedance, but in this study it is better to find an optimal matching network then fix the design of the sensor.

In the beginning, the simplest type of matching network is the L-section, which uses two reactive elements to match an arbitrary load impedance to a transmission line. There are two possible configurations for this network, as shown in Figure 2.26. If the normalised load impedance, $z_L=Z_L/Z_0$, is inside the $1+jx$ circle on the Smith Chart, then the circuit of Figure 2.26(a) should be used. If the normalised load impedance is outside the $1+jx$ circle on the Smith Chart, the circuit of Figure 2.26(b) should be used. The $1+jx$ circle is the resistance circle on the impedance Smith chart for which r =1. In either of the configurations of Figure 2.26, the reactive elements may be either inductors or capacitors, depending on the load impedances. Thus, there are eight distinct possibilities for the matching circuit for various load impedances. If the frequency is low enough and/or the circuit size is small enough, actual lumped-element capacitors and inductors can be used. This may be feasible for frequencies up to about 1 GHz. However, a large range of frequencies and circuit sizes where lumped elements may not be realisable. This is limitation of the L-section matching technique. The analytic expressions for the matching network elements of the two cases would be derived in figure 2.26.

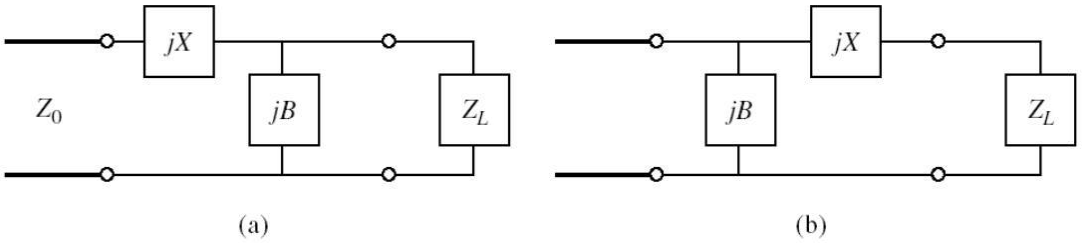

Figure 2.26 L-section matching networks. (a) Network for Z inside the 1+*jx* circle. (b) Network for Z outside the 1+*jx* circle.

Let us consider first the circuit of Figure 2.26(a), and let $Z_L = R_L + jX_L$. The circuit would be used when $z_L = Z_L/Z_0$ is inside the 1+*jx* circle on the Smith chart, which implies $R_L > Z_0$ for this case.

The impedance seen looking into the matching network followed by the load impedance must be equal to Z_0, for a match:

$$Z_0 = j\mathrm{X} + \frac{1}{j\mathrm{B} + 1/(R_L + jX_L)} \tag{2.34}$$

Rearranging and separating into real and imaginary parts gives two equations for the two unknown variables, X and B:

$$B(XR_L - X_L Z_0) = R_L - Z_0 \tag{2.35}$$

$$X(1 - BX_L) = BZ_0 R_L - X_L \tag{2.36}$$

Solving (2.35) for X and substituting into (2.36) gives a quadratic equation for B. The solution is

$$B = \frac{X_L \pm \sqrt{R_L/Z_0}\sqrt{R_L^2 + X_L^2 - Z_0 R_L}}{R_L^2 + X_L^2} \tag{2.37}$$

Note that since $R_L > Z_0$, the argument of the second square root is always positive. Then the series reactance can be found as

$$X = \frac{1}{B} + \frac{X_L Z_0}{R_L} - \frac{Z_0}{B R_L} \tag{2.38}$$

Equation (2.38) indicates that two solutions are possible for B and X. Both of these solutions are physically realisable, since both positive and negative values of B and X are possible. Positive X implies an inductor, negative X implies a capacitor, while positive B implies a capacitor and negative B implies an inductor. One solution may result in significantly smaller values for the reactive components, and may be the preferred solution if the bandwidth of the match is better, or the standing wave ratio (SWR) on the line between the matching network and the load is smaller.

Let us consider the circuit of Figure 2.26(b). This circuit is to be used when z_L is outside the 1+*jx* circle on the Smith chart, which implies that $R_L < Z_0$. The admittance seen looking into the matching network followed by the load impedance $Z_L=R_L+jX_L$ must be equal to $1/Z_0$ for a match:

$$\frac{1}{Z_0} = jB + \frac{1}{R_L + j(X + X_L)} \tag{2.39}$$

Rearranging and separating into real and imaginary parts gives two equations for the two unknowns, X and B:

$$BZ_0(X + X_L) = Z_0 - R_L \tag{2.40}$$

$$X + X_L = BZ_0 R_L \tag{2.41}$$

Solving for X and B gives

$$X = \pm\sqrt{R_L(Z_0 - R_L)} - X_L \tag{2.42}$$

$$B = \pm\frac{\sqrt{(Z_0 - R_L)/R_L}}{Z_0} \tag{2.43}$$

Since $R_L<Z_0$, the arguments of the square roots are always positive.

In order to match an arbitrary complex load to a line of characteristic impedance Z_0, the real part of the input impedance to the matching network must be Z_0, while the imaginary part must be zero. This implies that a general matching network must have at least two degrees of freedom; in the L-section matching circuit these two degrees of freedom are provided by the values of the two reactive components.

In practice, in order to reduce the passive elements and the complexity of the matching network, a continuously tapered line would be approached [121]. An approximate theory that is based on the theory of small reflections will be adopted to predict the reflection coefficient response as a function of the impedance taper, Z(z). Consider the continuously tapered line of figure 2.27 as being made up of a number of incremental sections of length Δz, with an impedance change ΔZ(z) from one section to the next, as shown in figure 2.27.

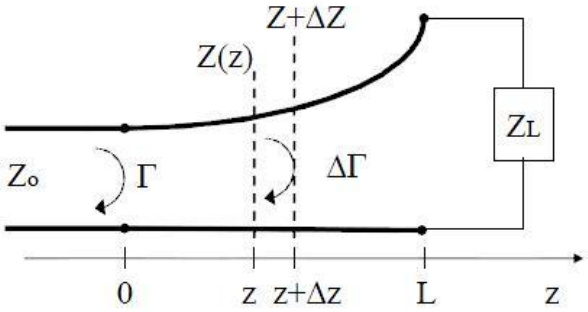

Figure 2.27 A tapered transmission line matching section and the model for an incremental step change in impedance of the tapered line.

Then the incremental reflection coefficient from the step at z is given by [121]:

$$\Delta\Gamma = \frac{(Z + \Delta Z) - Z}{(Z + \Delta Z) + Z} \simeq \frac{\Delta Z}{2Z} \tag{2.44}$$

In the limit as $\Delta z \rightarrow 0$ [121],

$$d\Gamma = \frac{dZ}{2Z} = \frac{1}{2}\frac{d(\ln Z/Z_0)}{dz}dz \tag{2.45}$$

Since [121]

$$\frac{d(\ln f(z))}{dz} = \frac{1}{f}\frac{f(z)}{dz} \tag{2.46}$$

Then, by using the theory of small reflections, the total reflection coefficient at z = 0 can be found by summing all the partial reflections with their appropriate phase shifts [121]:

$$\Gamma(\theta) = \frac{1}{2}\int_{z=0}^{L} e^{-2j\beta z}\frac{d}{dz}\ln\left(\frac{Z}{Z_0}\right)dz \tag{2.47}$$

Where $\theta = 2\beta\ell$. So if Z(z) is known, $\Gamma(\theta)$ can be found as a function of frequency. Alternatively, if $\Gamma(\theta)$ is specified, then in principle Z(z) can be found.

In this study, the method of tapered transmission line was used to match the impedance between connectors and Love-wave sensors. Figure 2.28 represents the device with original rectangular connection electrode (left) and the device with taper line for matching (right). These two devices are connected to the network analyser (Agilent E5071) and measured their return losses (S_{11} parameters) by smith chart, respectively. The results of return losses on smith chart are displayed in figure 2.29.

Figure 2.28 The pictures of the Love-wave devices with original rectangular connection electrode (left) and with taper line for matching (right).

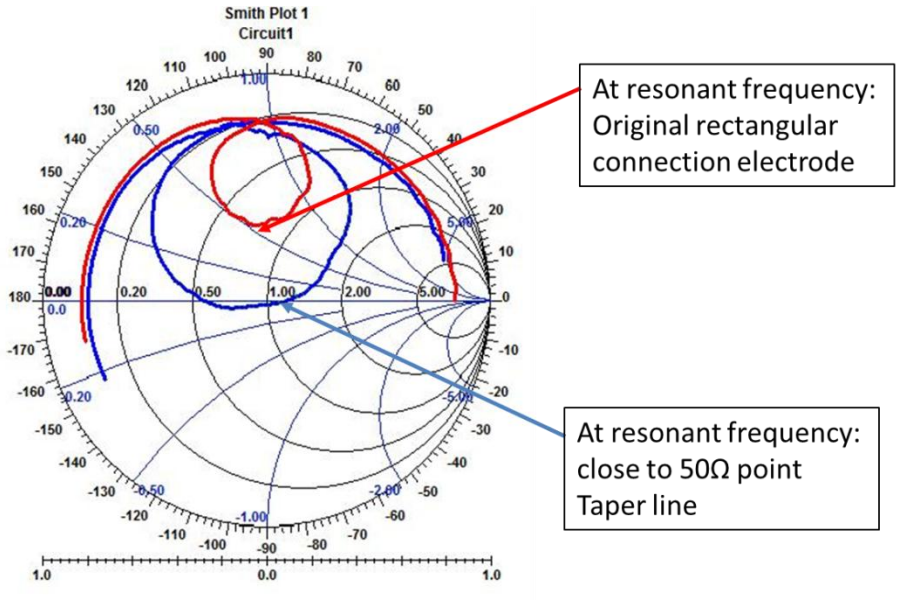

Figure 2.29 The results of return losses on the smith chart. Red line is the result of the Love-wave device with original rectangular connection electrode. Blue line is the result of the Love-wave device with taper line for matching. The frequency measurement ranges from 100M Hz to 130M Hz. These two Love-wave devices have the same resonant frequency at 114.83M Hz. The impedance of the resonant frequency of the device with original rectangular connection electrode is |Z| = 45.53Ω (37.2Ω+*j*26.25Ω). The impedance of the resonant frequency of the device with taper line is |Z| = 49.92Ω (49.9Ω-*j*1.55Ω). It can be observed that the impedance of the device with taper line is closer to 50Ω (the centre point of the circle in the smith chart) than the impedance of the device with original rectangular connection electrode.

These two Love-wave sensors are connected with a signal generator (Agilent, N5181A) and a RF signal power amplifier (Mini-Circuits, ZHL-5W-1). Then signal generator inputs a continuous sinusoidal signal to the Love-wave devices through power amplifier. A 5μl deionized water droplet is arranged on the surface of the device to absorb the energy that is transferred from the electric signal to the Love waves and using IR (Infrared) temperature sensor records the temperature change of the droplet. The total system setup is shown as figure 2.30. The results are illustrated in the figure 2.31. It can be observed that the temperature of the droplet rises with the increase of the input signal power. To compare with two devices which have different connection electrodes, the droplet temperature of the device with matching circuit (taper line) is obvious higher than

that the device without matching circuit (original rectangular connection electrode) at the same input power level. This result can explain that the Love-wave device with matching circuit not only prevent additional input signal from reflecting to the source but also exactly has a better efficiency to transfer input electric signal to output acoustic wave.

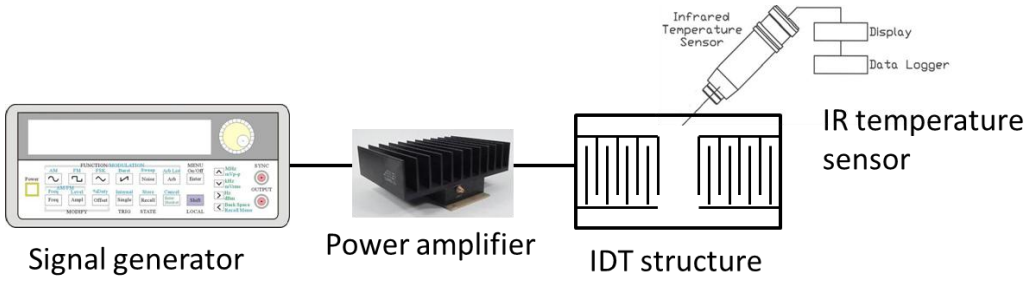

Figure 2.30 To measure the temperature changes on the surface of the Love-wave devices. Signal generator inputs a continuous sinusoidal signal into the power amplifier. After amplifying the signal, the signal is transferred in to the Love-wave device with original rectangular connection electrode and the Love-wave device with taper line, respectively. IR temperature sensor is used to measure the temperature changes on the surface of the devices.

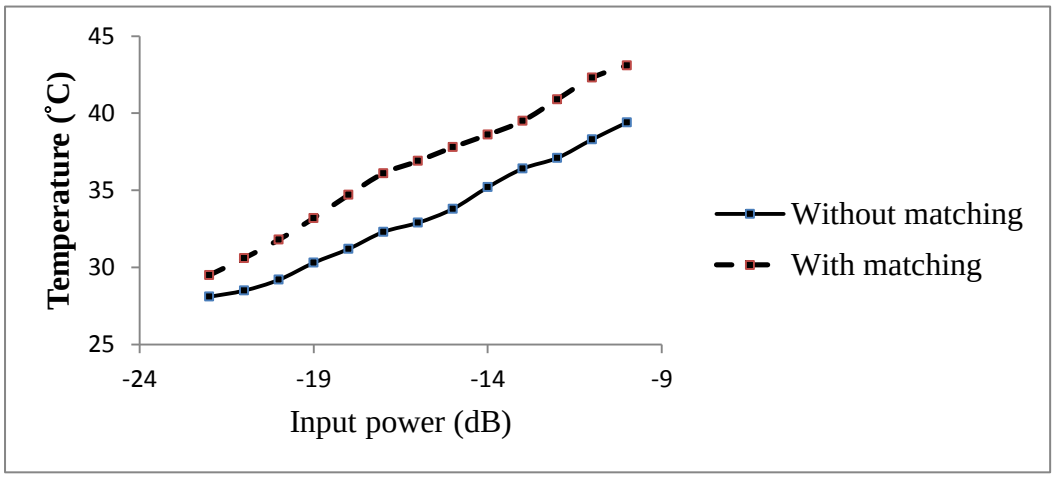

Figure 2.31 The relationship between input power and the temperature of the droplet on the device surface. The Red line is the result of the Love-wave device with matching circuit (taper line). The blue line is the result of the Love-wave device without matching circuit (original rectangular connection electrode).

2.6 The optimisation of the guiding layer thickness

The difference between the mechanical properties of the piezoelectric substrate and the guiding layer generates a confinement of the acoustic energy in the guiding layer,

slowing down the wave propagation velocity, but maintaining the propagation loss [51, 122]. In particular, the condition for the existence of Love wave modes is that the shear velocity of the guiding layer material ($v_L = (\mu_L/\rho_L)^{1/2}$) is less than that of the substrate ($v_S = (\mu_S/\rho_S)^{1/2}$) [123]. Here μ is the shear modulus, and ρ is the density of the material. The subscript L and S denotes the guiding layer and substrate respectively. When substrate and guiding layer have similar density ratio μ_S/μ_L determine the dispersion of the Love mode; a large value of that ratio (higher μ_S and lower μ_L) leads to a stronger entrapment of the acoustic energy [122] and greater sensitivity. Consequently, the benefit of the guiding layer is that an enhanced sensitivity to mass deposition can be obtained, but also to viscoelastic interactions [124].

The effect of the guiding layer on Love modes influences the substrate coupling factor K^2 [125]. It also affects the temperature behaviour, since it modifies TCD compared to their parent leaky SAW device.

In relation to the materials used for the guiding layer, those with a low shear velocity and low insertion loss seem to be the most promising materials for developing sensitive biosensors [122, 126, 127]. Materials such as silicon dioxide (SiO_2) [128], gold (Au) [66], zinc oxide (ZnO) [129], and polymers [130] have been used as guiding layers. The acoustic properties of these materials are shown in table 2.3.

Silicon dioxide (SiO_2), which is also known as fused silica, is a standard material in semiconductor industry and offers low damping, sufficient low shear velocity and excellent chemical and mechanical resistance [41]. It is the only native oxide of a common semiconductor which is stable in water and at elevated temperatures, an excellent electrical insulator, a mask to common diffusing species, and capable of forming a nearly perfect electrical interface with its substrate. When SiO_2 is needed on materials other than silicon, it is obtained by chemical vapour deposition (CVD), either thermal CVD or Plasma enhanced CVD (PECVD) [42]. The main shortcoming for SiO_2 is that the optimum thickness, at which the maximum sensitivity is reached, is very high, so this complicates

the manufacturing process. Regarding gold guiding layers, they provide very strong wave guiding, since gold has a relatively low shear acoustic velocity and a high density. However, it couples the RF signal from input to output IDT. Using ZnO as guiding layer has some advantages over those with a different material. The research team of Kalantar-Zadeh has reported that a Love-wave sensor with ZnO/ST-quartz structure can provide significantly high sensitivity, small TCD and high K^2 [129]. Moreover, $ZnO/LiTaO_3$ devices were also found to have higher mass sensitivity than $SiO_2/LiTaO_3$ devices [131]. However, there are several disadvantages with using ZnO. First, it is a wide-bandgap semiconductor of the II-VI semiconductor group and thus it can deteriorate the efficiency of the transducers and make some artefacts. Besides that, it gets easily rough when sputtered and is liable to react with acids, liquids, or moisture. Hence, it will dissolve if exposed to liquid environment, which is a severe problem in biosensors application. It is a better choice to use polymers as the guiding layer, such as polyimide, polydimethylsiloxane (PDMS) and polymethylmethacrylate (PMMA). Because of their low shear velocity, the Love-wave device will have a higher sensitivity. In addition, polymers are usually resistant to chemical agents [71]. Although there is a problem with acoustic damping (losses) when using polymers [132], to choose an appropriate polymer and optimize the thickness of the guiding layer still can have a promising result with low losses and high sensitivity.

In this study, PMMA is chosen as the guiding layer material. PMMA is a strong and light weight material. Its density is about 1.18 g/cm^3. Although the impact strength of PMMA is lower than polycarbonate and some engineered polymers, it still has higher impact strength than glass or polystyrene [133]. PMMA ignites at 460℃ and burns, forming carbon dioxide, water, carbon monoxide and low-molecular-weight compounds [134]. PMMA dissolves in many organic solvents because of its easily hydrolysed ester groups. In addition, its environmental stability is superior to most other plastics such as polystyrene and polyethylene [135]. Because PMMA is transparent and durable, it is a

versatile material and has been used in a wide range of fields and applications. For example, it has been used for rear-lights and instrument clusters for vehicles, appliances and lenses for glasses. PMMA in the form of sheets affords shatter resistant panels for building windows, skylights, bullet proof security barriers, LCD screens, furniture and many other applications. Methacrylate polymers are used extensively in medical and dental applications where purity and stability are critical to performance. Another characteristic of PMMA is that has a good degree of compatibility with human tissue. The hard contact lenses were frequently made of this material. In orthopaedic surgery, PMMA bone cement is used to affix implants and to remodel lost bone. Dentures are often made of PMMA, and can be colour-matched to the patient's teeth and gum tissue [136]. In semiconductor research and industry, PMMA plays a role as a resist in the electron beam lithography process. A solution consisting of the polymer in a solvent is used to spin coat on silicon or other kind wafers with a thin film. Patterns on this can be made by an electron beam, deep UV light, or X-rays. Exposure to these creates chain scission within the PMMA, allowing for the selective removal of exposed areas by a chemical developer, making it a positive photoresist. The advantage of using PMMA is that it admits for extraordinarily high resolution patterns to be made. Smooth PMMA surface can be easily nanostructured by treatment in oxygen radio-frequency plasma or vacuum ultraviolet (VUV) irradiation [137].

Table 2.3 The properties of variable materials using as guiding layer [138-140]

Material	Shear acoustic wave velocity(m/s)	Density (Kg/m^3)	Sensitivity ($Hz \cdot cm^2/ng$)	Thickness(nm)
Fused silica	3764	2200	15	12000
Zinc	2440	7100	16	7000
Gold	1200	19700	20	1500
Zinc Oxide	2650	5606	950	6000
PMMA	1100	1180	1500	3000

In order to discover the most appropriate thickness of PMMA in this study, the experiments of measuring the transmission gain with different thickness of PMMA were conducted. By using the spin coating technique, 24 different thicknesses of PMMA layers were arranged on the Love-wave devices. The range of the thickness was from 353nm to 3862nm. Then the insertion loss at resonant centre frequency of the different thickness PMMA devices was recorded and compared them with the blank control device (no PMMA on the device) to obtain the transmission gain respectively. The result is reported in figure 2.32. From the results of the experiment, it can be found that the transmission gain rises with the increase of PMMA thickness when the thickness is below 1000nm. If the thickness of PMMA is higher than 1300nm, more loss will generate (lower transmission gain) with the thicker PMMA layer. Therefore, the optimum thickness of PMMA guiding layer will be between 1000nm and 1300nm.

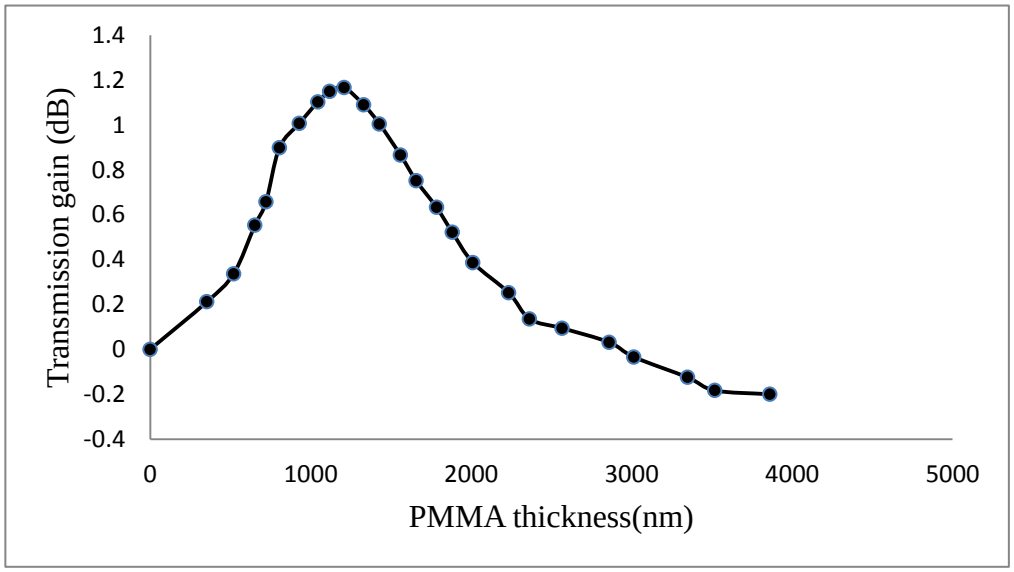

Figure 2.32 The relationship between transmission gain and the thickness of PMMA. The higher transmission gain represents the energy of Love-wave travelling in the guiding layer has a lower loss. With the increase of the PMMA thickness, more energy of acoustic waves could be trapped in the guiding layer. Hence, the transmission gain of the device became higher. However, PMMA is not a completely stiff material, which means that some energy of acoustic waves would be lost by travelling through the PMMA. If the thickness of PMMA increases, the loss that is induced by interactions with the material would rise. The sum of above two effects results in the outcome of the transmission gain. The optimum thickness of PMMA guiding layer in this study was suggested between 1000nm and 1300nm because the maximum of transmission gain appeared in this range.

2.7 Compensation of temperature effect

Because the temperature coefficient of delay (TCD) of the substrate 64° Y-X $LiNbO_3$ is not zero, the influence that changes of temperature affect the resonant frequency of the sensor was explored. The Love-wave sensor was placed on the hot plate. Then the temperature of the hot plate was tuned from 30℃ to 60℃. The practical surface temperature of the sensor was monitored by the IR temperature sensor. The resonant frequency of the Love-wave sensor was recorded while the temperature of the surface changed. The result of temperature and resonant centre frequency is shown in figure 2.33. With the increase of the temperature from 30℃ and 60℃, the resonant centre frequency of the Love-wave sensor decreases steadily from 116.46MHz to 116.22MHz. The relationship between resonant centre frequency and temperature was linear and the rate was -8 KHz/℃. This rate can be transferred as 78 ppm/℃. Compared with the report from Morgan [79] in table 2.2, the value of TCD in this device is similar to the previous study (81 ppm/℃). The experimental result was useful information to calibrate the data to compensate the influence of temperature changes under the sensing surroundings when measuring by the Love-wave sensor in this study.

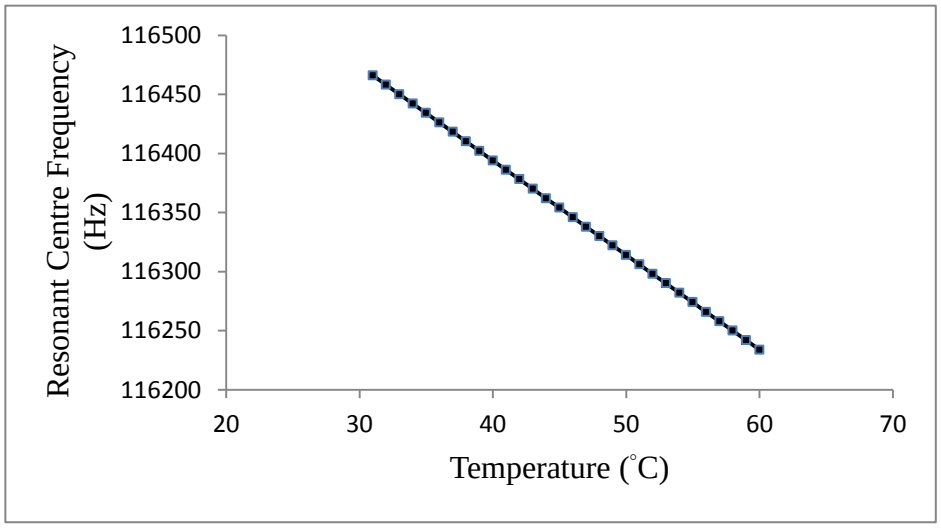

Figure 2.33 The result of resonant centre frequency changes with different temperature on the sensing surface of the Love-wave sensor. With the increase of the temperature from 30℃ and 60℃, the resonant centre frequency of the Love-wave sensor decreases linearly from 116.46MHz to 116.22MHz.

Chapter 3 Sensitivity and limit of the detection of the Love wave biosensor

3.1 Modelling method

Love-wave biosensors can be considered as devices which are consisted of two parts. The first part is the propagation of acoustic waves in the structure, and the second part is the sensing characteristics of the structure. Models allow relating changes to some characteristics of the wave, as with the velocity of changes in the physical properties of the layers deposited over the sensing area. In addition, models provide information about the sensing event [51]. Nevertheless, modelling Love-wave devices commonly requires simplified assumptions, or the use of numerical methods [131] because of the complex nature of SAW propagation in anisotropic and piezoelectric materials. In this section, information regarding the currently most popular models used for modelling Love-wave sensors is provided: the dispersion equation and the transmission line model.

3.1.1 Dispersion equation

The dispersion equation provides the wave phase velocity as a function of the guiding layer thickness. The procedure for obtaining this equation for a two-layer system (guiding layer and substrate) is detailed in the study of McHale *et al.* [141]. Broadly, this equation is reached after imposing the boundary conditions to determine the constants appearing in the particle displacement expressions of the waveguide and the substrate. These displacements are the solution of the equation of motion in an isotropic and non-piezoelectric material. After extensive algebraic manipulation, the dispersion equation for a two-layer system is as follows [142]:

$$\tan\left(k_{Ly}d\right) = \frac{\mu_s}{\mu_L}\sqrt{\frac{1-\left(\frac{v_\varphi^2}{v_s^2}\right)}{\left(\frac{v_\varphi^2}{v_s^2}\right)-1}} \tag{3.1}$$

Where k_{Ly} is the guiding layer transverse wavenumber in y direction, given by [142]:

$$k_{Ly} = \sqrt{\frac{\omega^2}{v_L^2} - \frac{\omega^2}{v_\varphi^2}} \tag{3.2}$$

Taking into account the relation between the frequency and wave wavelength, $f = v_\varphi/\lambda$, the argument of the tangent in equation (3.1) can be written as [142]:

$$k_{Ly}d = 2\pi v_\varphi \frac{d}{\lambda}\sqrt{\frac{1}{v_L^2} - \frac{1}{v_\varphi^2}} \tag{3.3}$$

The ratio d/λ is the normalized guiding layer thickness. From the dispersion equation, the phase velocity can be solved numerically [127]. On the other hand, the group velocity, v_g, as a function of the normalized guiding layer thickness can also be determined from the phase velocity by the equation [127]:

$$v_g = v_\varphi\left[1 + \frac{d/\lambda}{v_\varphi}\frac{dv_\varphi}{d(d/\lambda)}\right] \tag{3.4}$$

The phase velocity and group velocity of an 64°Y–X $LiNbO_3$/PMMA x propagating (the direction of x-axis is also the direction of acoustic wave propagating, which is provided by the material vendor) layered structure were calculated using the dispersion equation (eq. (3.1)) solved numerically through the bisection method. The data used to solve the equation for this Love-wave structure are: v_S = 4450 m/s, ρ_S = 4650 kg/m^3, v_L = 1100 m/s, ρ_L = 1180 kg/m^3 and λ = 40 μm. The respective shear modulus were obtained through $\mu_i = v_i^2\rho_i$. Assuming that the perturbing mass layer deposited over the sensing area is of the same material than the guiding layer, this equation will provide information over the sensing event. Nevertheless, this assumption is far from the biosensor's reality, where the consideration of a five–layer model is required as shown in figure 3.1.

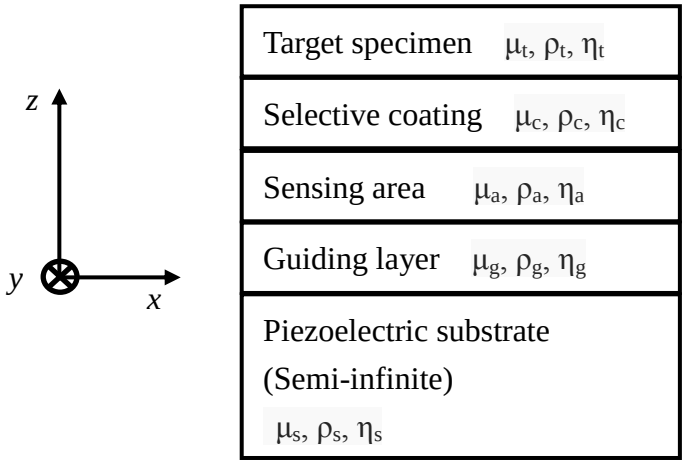

Figure 3.1 Five-layer model of a Love-wave biosensor. Each layer has its material characteristics given by: the shear modulus μ, density ρ, and viscosity η. The subscript s, g, a, c, and t denotes the substrate, guiding layer, sensing area, selective coating and target specimen, respectively. Axes are set as following: the acoustic waves propagate in the direction *x*, the direction *z* is aligned to the normal of the layers.

3.1.2 Transmission line model

Because the assumption of the dispersion equation is far from the Love wave biosensor's reality, the modelling result is just for reference. In order to develop a model that can get close to the experimental results, other researchers investigated another model – transmission line model [143, 144]. The first step is to set a reference coordinate plane (figure 3.1) that is representative of the problem. The direction of propagation of the wave is set as the x-axis that is parallel to the layer's boundaries. The normal to the boundaries is arbitrarily set as the z-axis aligned from the substrate to the top layer. The position of the origin is set at the interface between the substrate and the guiding layer. The n layers that compose the Love plates which include guiding layer, sensing area, and selective coating, are numbered from 1 to n from bottom to top. The substrate is assumed to be an infinite half space so that no number is attributed to it. The top half space (target specimen is here) is also an infinite half space and no acoustic waves propagate in this region.

For the considered problem of shear waves propagating along direction *x*, one has to define the initial properties of that propagation. The wave is considered independent of the

direction *y*. In addition, the wave is also considered to be polarised along this latter direction and so the local particle displacement **u** (or equivalently the local particle velocity **v**) has only *y* component [144]:

$$\mathbf{u}(x,z) = \begin{bmatrix} 0 & u_y(x,z) & 0 \end{bmatrix} \qquad (3.5)$$
$$\mathbf{v}(x,z) = \begin{bmatrix} 0 & v_y(x,z) & 0 \end{bmatrix}$$

For waves propagating in a waveguide structure, like the Love plate, an assumption has to be made: the main wave propagating in the *x* direction results from the interaction of two partial waves propagating in different directions. The other assumption is to consider all the materials as isotropic. Although it is not really the case for the piezoelectric substrate since it is a crystalline material, the approximation simplifies the problem, and remains meaningful if the anisotropy factor of the material is not too high. In each layer, the partial waves are propagating upwards and downwards, they are totally defined in the *xz* plane. The partial waves present the same component along the direction *x* and are symmetrical around this axis, the components along *z* are opposite. This effect results from the reflection of the partial waves at the layer interfaces, and is understood by considering the representation of the partial waves in the slowness curves of the materials (figure 3.2). A partial wave is considered to propagate along the direction *z'*. The direction is related to the axis by the angle θ that forms with one of the in-plane direction (figure 3.3). Arbitrarily the *z* direction is taken as reference [144]:

$$\boldsymbol{z}' = [\sin\theta \; 0 \; \cos\theta] \qquad (3.6)$$

It is easily seen that in each layer, the angles made by the two partial waves are supplementary, only θ has to be defined since the other one would be (π-θ).

All those definitions allow the translational equation of motion and the constitutive equation of the solid to be written as [144]:

$$\frac{\partial T_4(x,z)}{\partial z} + \frac{\partial T_6(x,z)}{\partial x} = \rho \frac{\partial v_y(x,z)}{\partial t} \qquad (3.7)$$

$$c_{44}\frac{\partial v_y(x,z)}{\partial z} = \frac{\partial T_4(x,z)}{\partial t} \tag{3.8}$$

$$c_{44}\frac{\partial v_y(x,z)}{\partial x} = \frac{\partial T_6(x,z)}{\partial t} \tag{3.9}$$

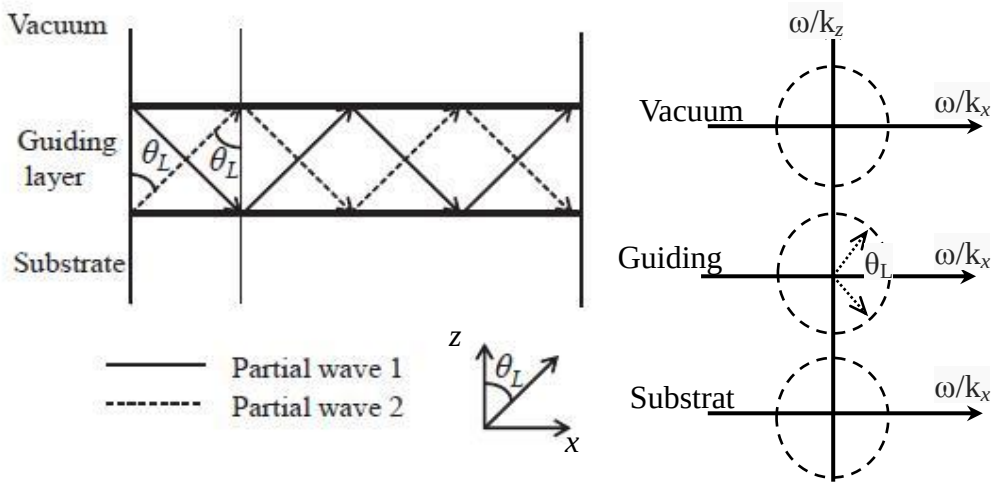

Figure 3.2 Simplified description of Love-waves traveling in a guided structure. The Love wave results from the interaction in each layer of partial waves propagating in opposite direction along *z* but with the same component along *x*. The common component along *x* gives the Love wave velocity. The partial waves are described by the slowness curves for each layer. ω the angular frequency of the wave and k is the wavenumber of the wave, so ω/k is the speed that wave travels in the +*x*/*z* direction [51].

The spatial derivatives expressed for *z'* are given by [144]:

$$\frac{\partial}{\partial x} = \frac{\partial}{\partial z'}\sin\theta \tag{3.10}$$

$$\frac{\partial}{\partial z} = \frac{\partial}{\partial z'}\cos\theta \tag{3.11}$$

To define $T_{4'}(z')$ as $(T_4(x,z)\cos\theta + T_6(x,z)\sin\theta)$, the relations are finally reduced to [144]:

$$\frac{\partial T_{4'}(z')}{\partial z'} = \rho\frac{\partial v_{y'}(z')}{\partial t} \tag{3.12}$$

$$c_{44}\frac{\partial v_{y'}(z')}{\partial z'} = \frac{\partial T_{4'}(z')}{\partial t} \tag{3.13}$$

and obviously the rotation of the axis has not changed the polarisation of the wave so that $v_{y'}(z') = v_y(x, z)$.

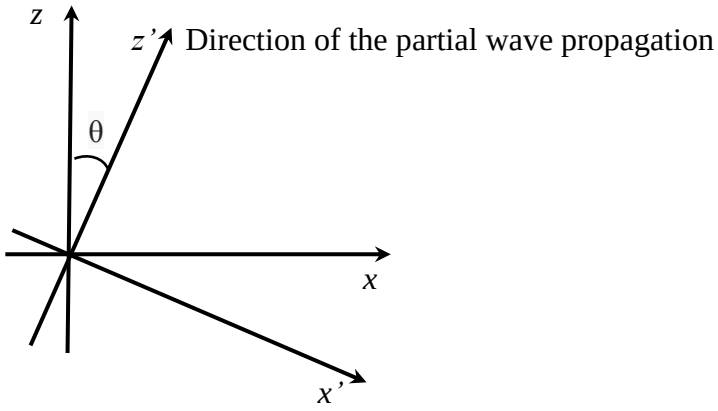

Figure 3.3 The partial wave propagates along direction *z'* that results of a rotation of the axis around y by an angle θ.

This section reports the basic relations needed for further modelling of the acoustic wave device. The theory for transmission line has been reported in previous studies [143, 144]. An infinitesimal length ∂r ($<<\lambda$) of transmission line is represented by a series impedance Z and a shunt admittance Y as shown in figure 3.4. The voltage $V(r)$ and tension $I(r)$ are linked together by the coupled equations [144]:

$$-\frac{\partial V(r)}{\partial r} = ZI(r) \tag{3.14}$$

$$-\frac{\partial I(r)}{\partial r} = YV(r) \tag{3.15}$$

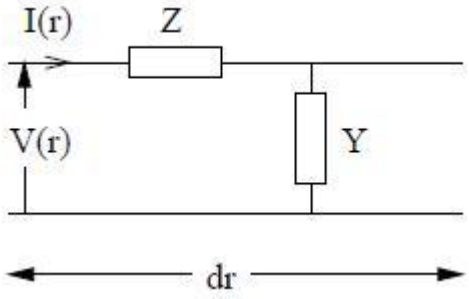

Figure 3.4 Infinitesimal equivalent circuit of a transmission line [51].

The transmission line admits a characteristic impedance $Z_c = (Z/Y)^{1/2}$ and a propagation function $\gamma = (ZY)^{1/2} = \alpha + j\beta$. The voltage and tension at any point of the line is the summation of two partial values V^- and V^+ that represent electrical waves propagating in opposite directions [51]:

$$V(r) = V^{+}e^{-\gamma r} + V^{-}e^{\gamma r} \quad (3.16)$$

$$Z_c I(r) = V^{+}e^{-\gamma r} - V^{-}e^{\gamma r} \quad (3.17)$$

For a transmission line of length L, the equivalent circuit is a quadrupole whose origin can be set to one end of the line. This origin is also considered as the attach point for any impedance loading. Due to the definition, voltage and current are easily computed at any point of the line if they are known at the origin as respectively $V(0)$ and $I(0)$ [51]:

$$V(r) = V(0)\cosh\gamma r + Z_c I(0)\sinh\gamma r \quad (3.18)$$

$$I(r) = -\frac{V(0)}{Z_c}\sinh\gamma r - I(0)\cosh\gamma r \quad (3.19)$$

For a line that only presents a partial value V and where ($r \leq 0$), the equations are [51]:

$$V(r) = V(0)e^{\alpha r}\cos(\omega t - \beta r) \quad (3.20)$$

$$Z_c I(r) = V(0)e^{\alpha r}\cos(\omega t - \beta r) \quad (3.21)$$

This case is typical of an infinite half-line. For a transmission line of length L loaded by an impedance Z_L, the equivalent impedance seen at the end of the line is [51]:

$$Z(L) = Z_c\frac{Z_c + Z_L\coth\gamma L}{Z_L + Z_c\coth\gamma L} \quad (3.22)$$

From the equations (3.12) and (3.13), a strong analogy with the fundamental equations of a transmission line is set. This analogy was known since a long time and has been reported for propagation of waves in the bulk of materials [144]. The analogy is given by comparing the mechanical stress $T_{4'}$ to the inverse of the electrical voltage and the local particle velocity v_y to the electrical current [51]:

$$T_{4'}(z') \equiv -V(r) \quad (3.23)$$

$$v_y(z') \equiv I(r) \quad (3.24)$$

Table 3.1. Comparison between the propagation of a shear wave in an isotropic medium and the propagation of an electrical wave in a transmission line.

Acoustic wave propagation	Electrical wave propagation
$\frac{\partial T_{4'}(z')}{\partial z'} = \rho\frac{\partial v_y(z')}{\partial t} = i\omega\rho v_y(z')$	$-\frac{\partial V(r)}{\partial r} = ZI(r)$
$c_{44}\frac{\partial v_y(z')}{\partial z'} = \frac{\partial T_{4'}(z')}{\partial t} = i\omega T_{4'}(z')$	$-\frac{\partial I(r)}{\partial r} = YV(r)$

Table 3.1 allows direct interpretation of the equivalence and helps to determine the equivalent parameters. In that table, the fields are assumed to be time-harmonic plane waves so that the time derivative is replaced by $i\omega$ factor multiplication of the term. The equivalent parameters are $Z = i\omega\rho$ and $Y = i\omega/c_{44}$ that correspond respectively to an inductance L (value ρ) and a capacitance C (value $1/c_{44}$). The equivalent model in transmission line of the isotropic and lossless medium is shown in figure 3.5 and the parameters are summarized in table 3.2.

Table 3.2. Summary of the equivalent transmission line parameters for isotropic solids that have a bulk wave phase velocity V. The impedance Z and the admittance Y are defined for an infinitesimal length. For the line itself, the relevant parameters are the characteristic impedance Z_c and the propagation function γ.

Series impedance	$Z = i\omega\rho$
Shunt impedance	$Y = i\omega/c_{44}$
Characteristic impedance	$Z_c = \sqrt{Z/Y} = \sqrt{\rho c_{44}} = \rho V$
Propagation function	$\gamma = \sqrt{ZY} = i\omega\sqrt{\frac{\rho}{c_{44}}} = \frac{i\omega}{V}$

Further models have been developed for viscous solids and piezoelectric solids. For viscous solids, the viscosity is represented by a conductance G in series with the shunt capacitance. The value of G is $1/\eta_{44}$. For piezoelectric solids, the situation is represented by the combination of a capacitance C_{piezo} in series with C, the result is a stiffened capacitance $C_{stiffened}$ whose expression depends upon the direction of propagation and is given by [51]:

$$\frac{1}{C_{stiffened}} = c_{44} + \left(\frac{e_{x4}^2}{\varepsilon_{xx}^s} sin^2 2\theta\right) \tag{3.25}$$

One has to be careful that the application of the equivalence is not direct for anisotropic solids, and requires usually better developments than shown here. These developments would not be reported here since they are irrelevant for the modelling of the Love-wave device.

The equivalence has been set for the specific propagation of the partial wave. The equivalence with the Love wave device is given by a decomposition of the Love wave that propagates in each layer of the device along the direction *x* and the direction *z*. Along the longitudinal direction *x*, the propagation is totally free. The ideal case corresponds to the propagation of the wave in an unbound medium. Along the transversal direction *z* the wave is submitted to a condition of resonance: at each boundary, the partial waves are reflected. Incident, transmitted and scattered waves interact together under specific conditions that are directly derived from transmission line theory. Figure 3.6 illustrates the decomposition of the Love wave device into the two equivalent transmission lines. The parameters of each transmission line are linked by the angle of propagation θ_i (with *i* different in each layer).

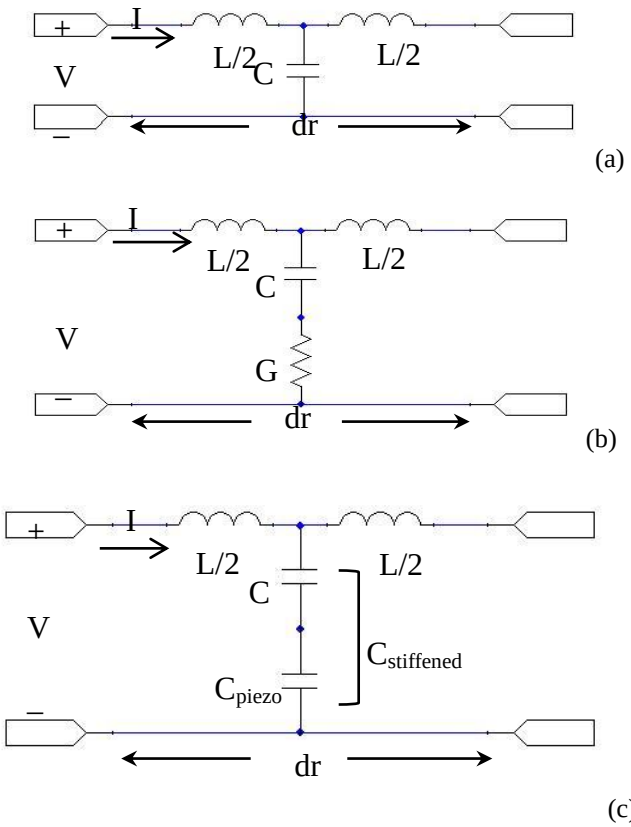

Figure 3.5 The equivalent transmission line model of the propagation of shear wave in different mediums: (a) isotropic, lossless medium, (b) isotropic, lossy medium, and (c) piezoelectric, lossless medium (for piezoelectric substrates this assumption is valid because of a low anisotropy). The inductance *L* has the value ρ and the capacitance C has the value $1/c_{44}$. For a viscous medium, the shunt arm is the series combination of the mechanical capacitance with a conductance G that has the value $1/\eta_{44}$. For a piezoelectric media, a piezoelectric capacitance C_{piezo} is included in series with the mechanical capacitance. The total effect of C and C_{piezo} results the stiffened capacitance $C_{stiffened}$.

The selection of direction is important because the reference plane of atoms arrangement would be different. If choosing direction y (along y-axis) for the propagation direction of acoustic waves, the result would be not the same with the propagation direction of x-axis because the Love mode acoustic waves could not be excited. The decomposition allows the impedance of the line to be computed for the two main directions. The impedance matrices admit only non-zero component for the central component. The impedance value in the directions *x* and *z* are then [51]:

$$(Z_x^k)_{22} = \frac{c_{66} k \sin\theta}{\omega} \tag{3.26}$$

$$(Z_z^k)_{22} = \frac{c_{44} k \sin\theta}{\omega} \tag{3.27}$$

The expression given by the impedances are in agreement with the decomposition approach; the impedances are given by the projection of the impedance experienced by the partial wave propagating along *z'* on the main directions *x* and *z*. Since for isotropic solids, $c_{44} = c_{66}$ and $\omega/k = V = (c_{44}/\rho)^{1/2}$, the relations are as follows:

$$(Z_x^k)_{22} = \sqrt{\rho c_{44}} \sin\theta \tag{3.28}$$

$$(Z_z^k)_{22} = \sqrt{\rho c_{44}} \cos\theta \tag{3.29}$$

The guiding of the Love wave in the structure is possible on the condition that the partial waves reflected and transmitted interact in phase to give rise to a coherent interference that holds the signal in the structure and embeds the wave in the layers. The partial waves are forced to verify the boundary conditions at each interface; these mechanical conditions are given by the relations of Snell's law, and are directly solved in the decomposition, when the equivalent transmission lines in the direction *z* constitute a series network. The continuity of the equivalent voltage and current is appropriated to the continuity of the mechanical stress and particle velocity at each interface [143].

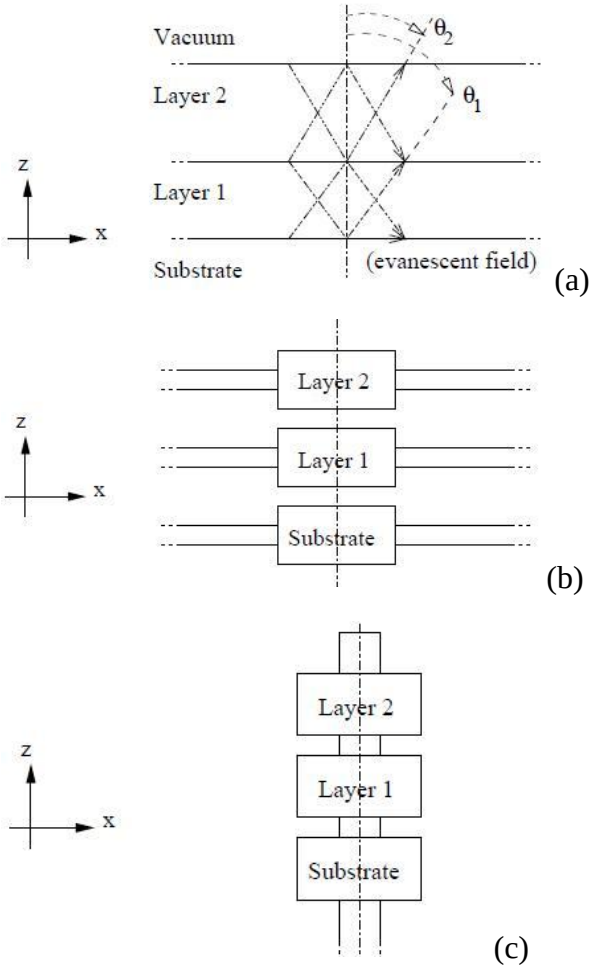

Figure 3.6 The equivalence between shear waves in solids and transmission line is applied to the Love wave device. (a) For a proper Love wave velocity, each layer (layer 1, 2 …) has a different angle of propagation θ_i (with *i* associated to each layer). (b) In the longitudinal direction *x*, the layers' structure is the superposition of the equivalent transmission line of each layer. These lines are only linked by the angles θ_i and they all admit the same propagation function, which corresponds to the Love wave velocity. (c) In the transversal direction *z*, the device is the series network of the transmission lines associated to each layer. The Love wave corresponds to a resonating scheme in this structure.

From the classical transmission line theory, waves are able to enter a resonating scheme in the structure if the impedances seen from any point of the structure in the two directions are opposite. Therefore, the impedance of the line seen at the point z_0 when looking to the increasing values of *z* is $Z^+(z_0)$, and the impedance of the line seen at the same point when looking to the decreasing values of *z* is $Z^-(z_0)$ (figure 3.7). The resonance condition is then expressed as [51]:

$$Z^+(z_0) + Z^-(z_0) = 0 \tag{3.30}$$

It should be noticed that this expression is a general relation that may involve complex numbers; no restriction has been made on the nature of the impedances. In particular, the relation may involve complex values that have to be exactly equal. This means that two scalar relations have to be solved simultaneously to observe the resonance of the wave in the structure. The angle that checks the resonance condition corresponds to one Love mode.

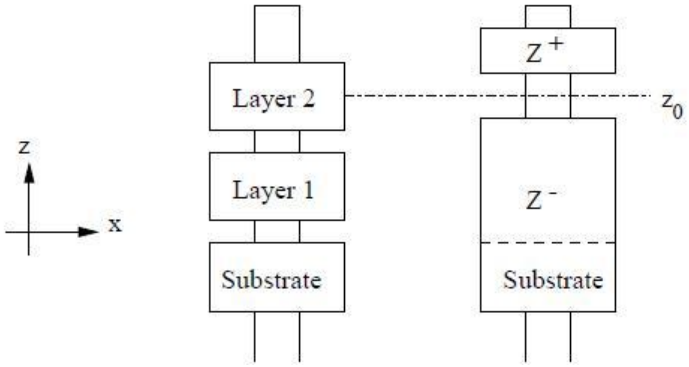

Figure 3.7 The equivalent network in the direction *z* set the resonance condition. The line presents two impedances Z^+ and Z^- at any point z_0 of the layered structure. These two impedances are a function of the geometry of the structure, of the materials' combination, and of the angles of propagation of the partial waves.

Another problem that needs to be solved is the determination of the impedance seen at the point z_0. The geometry of the device has to be taken into account, in particular the thickness of the different layers. The first step is to determine the angle of propagation in all layers and in the substrate. Snell's law links the angles. A particular layer is selected as the reference layer for the angle. It is usually easier to take the layer that presents the higher slowness, since the angle of resonance has to be a real number (a complex angle of propagation is related to evanescent fields). This angle is swept between 0 and $\pi/2$; the angles in the different layers must follow the variation of the angle in the reference layer. For a given angle, the acoustic impedance and propagation function of the layers are different. The impedance seen at the position z_0 is directly deduced by the equation (3.22) where the length L of the transmission line is equivalent to the thickness of the layer. The relation has to be used from the bottom of the device (position 0) to z_0 and from the top of

the device to z_0. For modelling, the top layer is always considered to be a vacuum. It is a specific medium that is modelled by a zero-impedance element (short-circuit).

Variations in amplitude and phase of the transfer function $H(f) = V_{out}/V_{in}$ (due to perturbations in the acoustic wave) can be monitored in real-time. These perturbations can occur due to variations of the mechanical and geometrical properties of the layers deposited over the sensing area. Such physical changes affect the propagation factor of the wave, and the attenuation and phase velocity of the Love wave. Next, the relations between Love wave electrical parameters (phase shift, φ and insertion loss, IL) and the complex propagation factor are explained.

The relation between the output and input voltage in a delay line (DL) of length l can be modelled by its transfer function $H_{DL}(f)$ in the following way [144]:

$$H_{DL}(f) = e^{-\gamma l} \tag{3.31}$$

where γ corresponds to the propagation factor of the wave in the line, which in this case corresponds to that of the guiding layer in the z direction γ_{Lz}. Assuming that the transfer function of the input and output IDTs is equal to unit, the relation between the electrical signal in the output and input IDTs $H(f)$ is the same than the one for the delay line [79]:

$$H(f) = \frac{V_{out}}{V_{in}} = \frac{|V_{out}|}{|V_{in}|} e^{j(\varphi_{out} - \varphi_{in})} = \frac{|V_{out}|}{|V_{in}|} e^{j\varphi} = e^{-\gamma_{Lz} l} \tag{3.32}$$

$$e^{-\gamma_{Lz} l} = e^{-(\alpha_{Lz} + j\beta_{Lz}) l} \tag{3.33}$$

Thus, the normalized phase shift (φ) and insertion loss (IL) are given by [144]:

$$\frac{IL}{z} = -\alpha_{Lz} 20 \log e \tag{3.34}$$

$$\frac{\varphi}{z} = -\beta_{Lz} \tag{3.35}$$

The increment in IL/z and φ/z from a non-perturbed state γ_{Lz0} to a perturbed state γ_{Lz1} is the

following [144]:

$$\Delta\frac{IL}{z} = (\alpha_{Lz1} - \alpha_{Lz0})20\log e \tag{3.36}$$

$$\Delta\frac{\varphi}{z} = \beta_{Lz1} - \beta_{Lz0} \tag{3.37}$$

The last set of equations provides a relation between the experimental data and the physical parameters of the layers. The extraction of the layers' physical parameters is a major problem and is the limit of the transmission line model. It is possible to measure and extract related parameters when adding a layer on the device each time. But the parameters of the coating layer in total layers could not be extracted exactly. The reason is the mechanical characteristics of the coating layer when it is isolated or not in contact with, the test sample would be different from when the coating layer interacts with the test specimen. Even assuming that the physical properties of the substrate, guiding layer, gold and test specimen are known and these properties do not change during the sensing process (which can be the case in biosensing), still the parameters of the coating layer are not known. In Love-wave sensors, the assumptions that the thickness of the coating layer is acoustically thin and that biochemical interaction is translated to a *simple* mass change is not always valid. Therefore the experimental data obtained in Love wave devices (equation (3.36) and (3.37)) from sequential measurements of the device with and without the coating layer (and any bound analyte species) are not necessarily enough to extract the unknown parameters of the coating. Therefore, the results of transmission line model are slightly different from the practical experimental results.

3.2 Experimental results of the sensitivity of the Love-wave biosensor

The sensitivity of the Love-wave sensor on theoretical calculations has been discussed in the previous section. However, it is necessary to discover the practical sensitivity of the sensor in this study through measurement by conducting experiments. The means to

investigate the sensitivity is demonstrated as follow. First, a blank control experiment with no added test specimen on sensing area (just air, because the theoretical calculations indicate that the results of testing under air and vacuum are almost the same) was conducted. The measurement setup (including matching the connector, using TRL calibration, and temperature compensation) has been shown in figure 2.17. The frequency response to the insertion loss is recorded by network analyser. After that, a 10nm thickness of titanium layer was deposited on the sensing area (a rectangular region that in length is 2mm and the width is 5mm). Then the frequency response about the insertion loss was measured again. Because the volume and the density of the Titanium (4.506g/cm^3) were known, the mass on the sensing area of the sensor can be obtained by calculation. Then another 10nm thickness of titanium layer was deposited on the sensing area again, so the total thickness of titanium on the sensor was 20nm, and its frequency response data was measured. The measurement was repeated by 10 times and every time the thickness of titanium was increased by 10nm up to 100nm. The next step was to explore the resonant centre frequency shifts among these experiments. The definition of “frequency shift” is shown in figure 3.8. The peaks of curves are the resonant centre frequencies. In figure 3.8, the solid line represents data from the blank control experiment, and the dotted line represents the data of 100nm thickness titanium on the senor. The frequency peaks of these two curves are different. The peak frequency of the dotted line is lower than that of the solid line. The difference between them is the “frequency shift”. In this case, it can be observed that the frequency shift is 11.6 kHz. In addition, the insertion loss of the dotted line is lesser than that of the solid line by 0.3dB. The reason is that some energy of acoustic wave is lost in the layer of deposited titanium. It can be considered that most of the energy of acoustic is kept in the guiding layer due to Love wave is shear horizontal wave, and the loss will not affect the result of frequency shift.

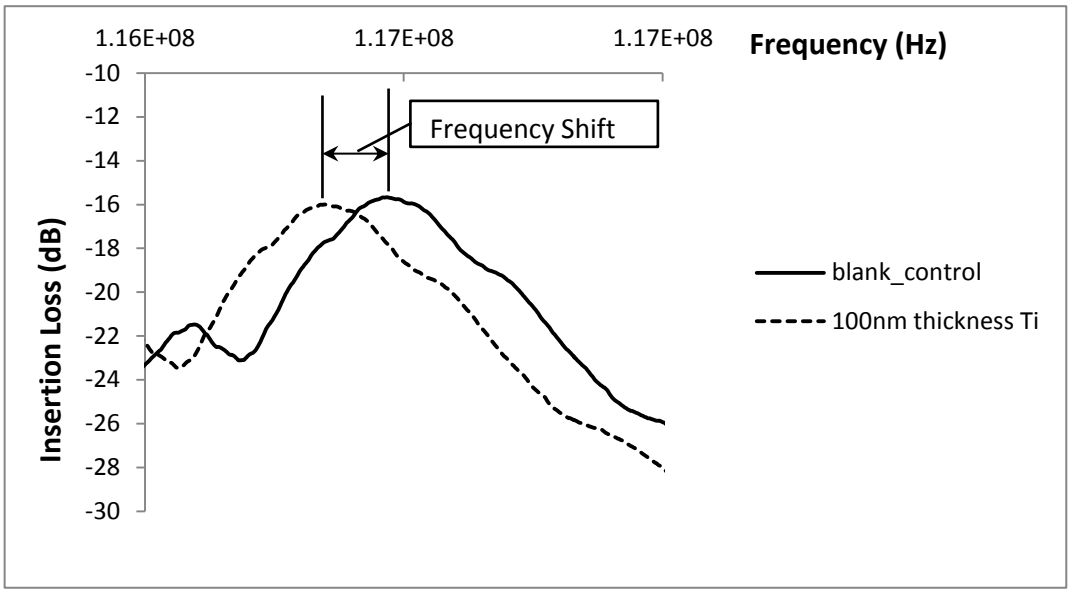

Figure 3.8 The comparison between resonant centre frequency of the shift between the different conditions of Love-wave sensor

The detail result of the relationship between frequency shift and thickness of titanium is shown in figure 3.9. With the increasing thickness of the deposited titanium layer, the frequency shift gradually rises. The mass of the deposited layer can be transferred from the data of titanium thickness. In addition, it can be found that the relationship between mass and frequency shift is linear. As a result, the sensitivity of the Love wave sensor in this study reaches 2574mm^2/ μg.

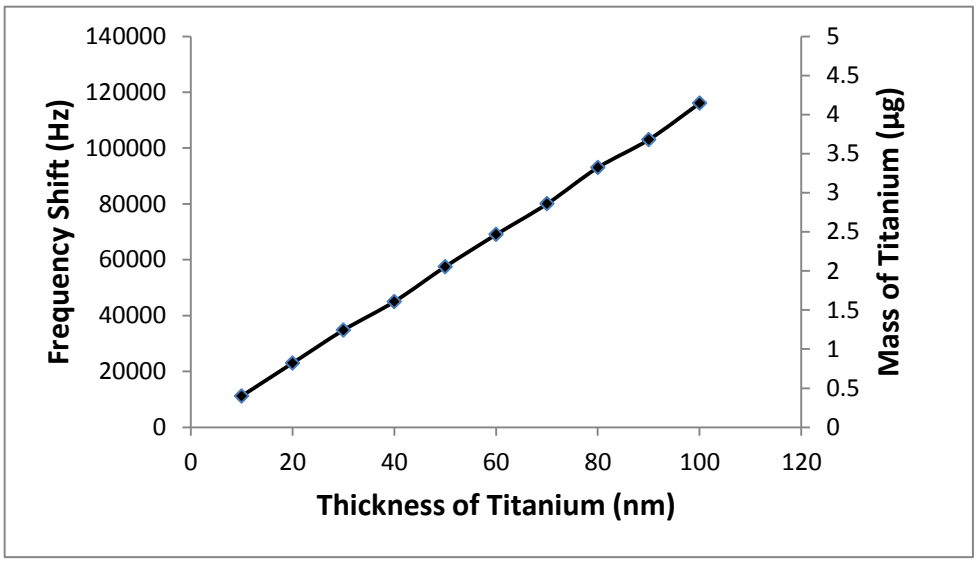

Figure 3.9 The comparison between resonant centre frequencies of the shift between the Love-wave sensors

3.3 Limit of detection (LOD) of the Love wave biosensor

The limit of detection (LOD) is a very important characteristic of acoustic biosensors, since it gives the minimum surface mass that can be detected by the device. It can be directly derived from the ratio between the noise in the measured electrical signal N_f and the sensitivity of the device. It is usually recommended to measure a signal variation higher than 3 times the noise level in order to conclude from an effective variation [145]. From this recommendation, it emerges that the LOD is given by [146]:

$$LOD = \frac{3N_f}{Sensitivity \cdot f} \tag{3.38}$$

where f is the resonant centre frequency. The LOD can be improved by minimizing the influence of temperature on the sensor response [147]. The stability with respect to temperature can be achieved by implementing temperature control in the biosensor system. In this study, the noise N_f is the root mean square (RMS) value of the resonant centre frequency variation measured over a given period of time in stable and constant conditions. Under the condition of blank control experiment, the value of N_f is obtained as 2.2Hz. From previous section, the sensitivity of the Love wave sensor and the resonant centre frequency are 2574mm^2/μg and 116.467 MHz, respectively. Hence, the LOD of the Love wave sensor in this study is 0.022fg/mm^2.

Chapter 4 Experimental Results of Love-wave sensor

4.1 Measurement of protein A

Protein A is a kind of protein which is found on the surface of the cell wall of the bacterium Staphylococcus aureus. Its mass on a molecular scale is 42 kDa and its regulation is controlled by DNA topology, cellular osmolarity, and a two-component system called ArlS-ArlR [148]. Because of its ability to bind immunoglobulins, protein A is usually used in biochemical research. In this study, the Love wave sensor was used to measure the protein A and test the function of the sensor. The test specimen of protein A is purchased from Invitrogen (catalog number: 10-1011), ensuring that the product is in 10 mM Phosphate buffered saline, pH 7.4 containing 1% ovalbumin, 40% glycerol and 0.1% sodium azide as preservative. It is composed of five homologous Ig-binding domains that fold into a three-helix bundle. Each domain is able to bind proteins from many mammalian species, most notably IgGs [149]. Protein A binds with high affinity to human IgG1 and IgG2 as well as mouse IgG2a and IgG2b. Protein A binds with moderate affinity to human IgM, IgA and IgE as well as to mouse IgG3 and IgG1. It does not react with human IgG3 or IgD, nor will it react to mouse IgM, IgA or IgE. The capacity of protein A to bind antibodies with such high affinity is the driving motivation for its industrial scale use in biologic pharmaceuticals. The protein A used for production of antibodies in bio-pharmaceuticals is most commonly bound to a stationary phase chromatography resin [150]. Recombinant Staphylococcal Protein A is often produced in E. coli for use in immunology and other biological research [151]. Protein A is often coupled to other molecules such as a fluorescent dye, enzymes, biotin, and colloidal gold or radioactive iodine without affecting the antibody binding site. It is also widely utilised coupled to magnetic, latex and agarose beads. Protein A is often immobilised onto a solid support and used as reliable method for purifying total IgG from crude protein mixtures such as serum

or ascites fluid, or coupled with one of the above markers to detect the presence of antibodies. Immunoprecipitation studies with protein A conjugated to beads are also commonly used to purify proteins or protein complexes indirectly through antibodies against the protein or protein complex of interest [152]. A droplet platform was used in this study and a chamber was established on the sensing area to locate droplets for each experiment.

In this study, protein A was used to test the efficiency of the Love wave sensor. In order to do this, experiments were conducted to examine whether Protein A could be immobilised on the sensing area of the sensor, and whether the sensor is capable of detecting the Protein A molecules. First, the sensing area (gold surface) of the sensor was immersed in buffer solution (Sigma Dulbecco's Phosphate Buffered Saline, product number: D8537) for 30minutes and was shaken at a rate of 10rpm. After that, the surface was dried with a nitrogen stream and cleaned under the oxygen Plasma Asher (100Watt, 180 seconds) to ensure that there was no impurity on the sensing area. The next step was to arrange a 2μl deionized water (Diwater, obtained from Milli-Q A10 Synthesis Ultrapure Water System) on the sensing area, then waited for 15 minutes to let the water evaporate naturally and measured the frequency shift of the sensor. The value of the frequency shift was 0.9 KHz. Then the sensing area was cleaned by buffer solution rinsing and oxygen Plasma Asher again. The next step was to arrange a 2μl buffer solution (PBS, Sigma, D8537) on the sensing area and waited for 15 minutes to let the PBS evaporate naturally. Then the buffer solution was used to wash the surface of the sensing area and measured the frequency shift of the sensor. The value of the frequency shift was 1 KHz. Then the sensing area was cleaned again by the same procedure as descripted above. The next step was to arrange a 2μl Protein A (Invitrogen, 10-1011) at a concentration of 15mg/ml on the sensing area and the frequency shift of the sensor was recorded. The value of the frequency shift was 66.4 KHz. After 15 minutes, the solvent of the Protein A solution evaporated naturally. The sensing area was rinsed with PBS to remove the molecules of Protein A that had not

immobilised well on the surface. After that, the surface was dried with a nitrogen stream, and the frequency shift of the sensor was measured to obtain the value of 25.2 KHz. Then a 2μl buffer solution (PBS, Sigma, D8537) was arranged at the same location of the Protein A solution droplet, and measured the frequency shift again. The value of the frequency shift was 69.4 KHz. The whole procedure was repeated 5 times, and deviations of the results were less than 10%. In addition, the results, including the error bar, are displayed in figure 4.1.

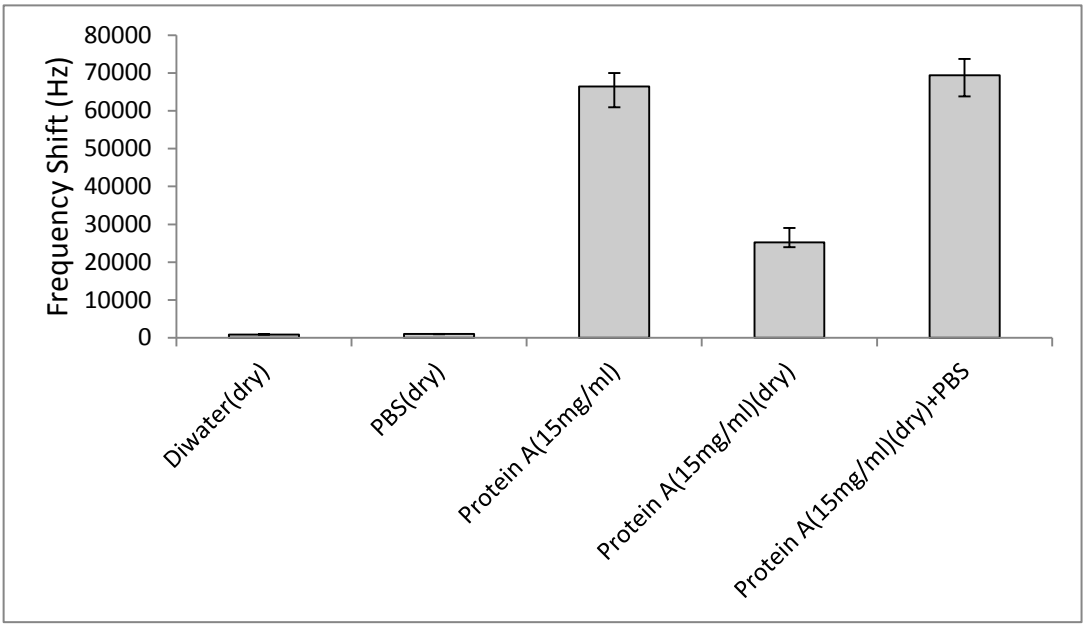

Figure 4.1 The frequency shifts of different kinds of materials and conditions on the Love wave sensor. The frequency shifts of Diwater and PBS under the dry state are both less than 1 KHz because there are almost no molecules left on the sensing area. The frequency shift of the liquid state of Protein A is more than that of the dry state of Protein A, by 41.2 KHz. This is because the mass of solvent and the viscosity of the solution lead to increase frequency shift. The frequency shift of Protein A under the dry state after rinsing by the PBS is 25.2 KHz, which is supporting evidence that Protein A did immobilise on the surface of the sensing area, and its mass causes the change of the centre resonant frequency. The frequency shift of dry state Protein A plus PBS is more than that of Protein A solution by 3 KHz, and the reason is that the condition of the solvent is different (Protein A solution is not the same as PBS and some Protein A molecules were removed when rinsing).

Some environmental factors would influence the frequency peak shift, such as the temperature and the connection state between cables and the sensor. The temperature factor was discussed in previous section (chapter 2.1) and the dual channel system could be used

to reduce the influence of temperature change. The state of connections between cables and the sensor would also affect the result of measurement. In early measurements, the electrode pads of the sensor were touched with probes to measure the signals. However, the variations of frequency peak shift between nominally the same measurements, were more than 3 KHz; even there was no added target on the sensing area. Consequently, connecting wires were stuck on the electrode pads with silver paste. This lead to variations in measurement results of less than 1 KHz. As a result, silver paste was adopted as the best method to fix wires on the electrode.

After the immobilisation of Protein A on the sensor was confirmed, the next experiment was designed to discover the relationship between the concentration of Protein A and frequency shift. Before each measurement, the sensing area of was completely cleaned. The clean processes were the same with the above descriptions (PBS rinsed, treated with plasma, dried with nitrogen stream). The steps of arrange droplets to conduct experiment were as follows: to arrange a 2μl Protein A solution (Invitrogen, 10-1011) with a concentration of 5mg/ml on the sensing area. After 15 minutes, the solvent of the Protein A solution was evaporated naturally, leaving the Protein A molecules on the sensing area. Then, the surface was rinsed by PBS to remove Protein A molecules that were not firmly immobilised on the sensing area. Afterwards, there were still some Protein A molecules immobilised on the sensor, and the frequency shift of the device was measured. Next, measurement with the same concentration of Protein A was repeated 5 times. According to the above processes, the frequency shifts with different concentrations of Protein A solution (5mg/ml, 10mg/ml, 12mg/ml, 13mg/ml, 14mg/ml and 15mg/ml, respectively) were monitored. The relationship between frequency shift and concentration of Protein A is illustrated in figure 4.2. The data points in the figure are the medians for measurements at each Protein A concentration. The deviations at each measurement of concentration are less than 1 KHz, and shown in the error bars in figure 4.2. When the concentration of Protein A

is less than 14mg/ml, the relationship seems to be linear between the frequency shift and the Protein A concentration. The higher Protein A concentration resulted in more frequency shift. However, the Protein A concentration is higher than 14mg/ml. A very slightly increase of frequency shift (less than 2 KHz) was observed. This can be explained by the saturation of the sensing area by means of Protein A molecules occupied almost whole space on the sensing area.

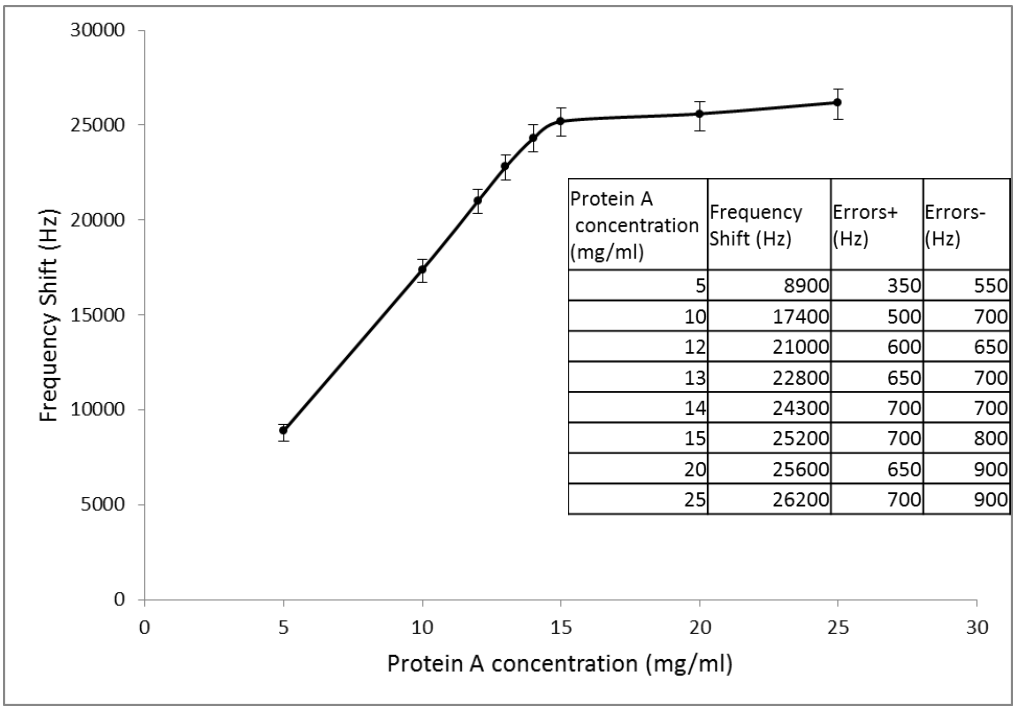

Protein A concentration (mg/ml)	Frequency Shift (Hz)	Errors+ (Hz)	Errors- (Hz)
5	8900	350	550
10	17400	500	700
12	21000	600	650
13	22800	650	700
14	24300	700	700
15	25200	700	800
20	25600	650	900
25	26200	700	900

Figure 4.2 The relationship between frequency shift and Protein A concentration. Under the saturation concentration of 14 mg/ml, frequency shift almost rises linearly with the increase of Protein A concentration. When the concentration of Protein A exceeds 14mg/ml, higher Protein A concentration only causes slightly increase of frequency shift. This is because the sensing area is almost saturated by the Protein A molecules, and more Protein A molecules could hardly immobilise on the sensor to increase the mass on the surface of the sensing area. The measurement data includes medians and deviations (errors) are in the table of the figure.

4.2 Measurement of IgG

IgG (Immunoglobulin G) is a kind of protein that it belongs to an antibody isotype. The mass of IgG antibodies on a molecular scale is approximately 150 kDa. IgG is composed of four peptide chains, which are two identical class γ heavy chains of about 50

kDa and two identical light chains of about 25 kDa; thus, there is a tetrameric quaternary structure, shown in figure 4.3 [153]. The two heavy chains are linked to each other and to a light chain each by disulfide bonds [154]. The resulting tetramer has two identical halves, which together form the Y-like shape. Each end of the fork contains an identical antigen binding site. The Fc regions of IgGs carry a highly conserved N-glycosylation site. The N-glycans attached to this site are two mainly core-fucosylated biantennary structures of the complex type. In addition, small amounts of these N-glycans also bear bisecting GlcNAc and α-2,6-linked sialic acid residues [155]. Representing approximately 75% of serum immunoglobulins in humans, IgG is the most abundant antibody isotype found in the circulation. IgG molecules are usually synthesized and secreted by plasma B cells [156].

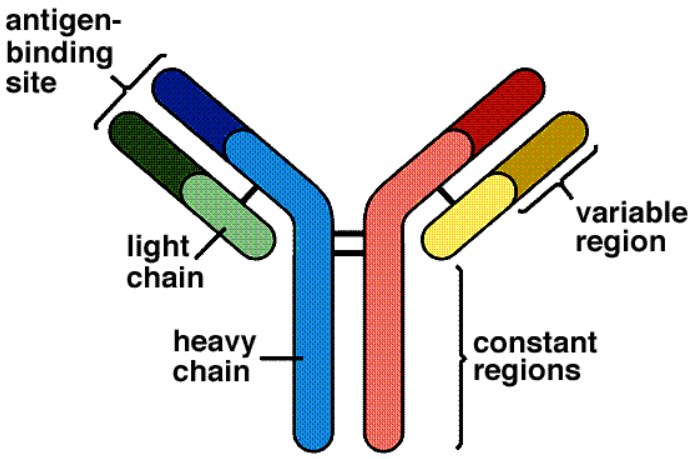

Figure 4.3 The structure of IgG. It is composed of four peptide chains: two identical heavy chains and two identical light chains, arranged in a Y-shape typical of antibody monomers. Each IgG has two antigen binding sites [153].

Antibodies are major components of the immune system. IgG is the main antibody isotype, found in blood and extracellular fluid, allowing it to control infection of body tissues. By binding many kinds of pathogens — representing viruses, bacteria, and fungi — IgG protects the body from infection. IgG can work via several immune mechanisms: IgG-mediated binding of pathogens causes their immobilisation and binding

together via agglutination; IgG coating of pathogen surfaces (known as opsonization) admits their recognition and ingestion by phagocytic immune cells; IgG activates the classical pathway of the complement system, a cascade of immune protein production that results in pathogen elimination; IgG also binds and neutralizes toxins. Additionally, IgG also plays an important role in antibody-dependent cell-mediated cytotoxicity and intracellular antibody-mediated proteolysis, in which it binds to TRIM21 (the receptor with greatest affinity to IgG in humans) in order to direct marked virions to the proteasome in the cytosol [157]. IgG antibodies are generated following class switching and maturation of the antibody response, and participate predominantly in the secondary immune response. IgG is secreted as a monomer that is small in size, allowing it to easily perfuse tissues. It is the only isotype that has receptors to facilitate passage through the human placenta, thereby providing protection to the foetus in utero. Along with IgA secreted in the breast milk, residual IgG absorbed through the placenta provides the neonate with humoral immunity before its own immune system develops [158]. Colostrum contains a high percentage of IgG, especially bovine colostrum. In individuals with prior immunity to a pathogen, IgG appears about 24–48 hours after antigenic stimulation [159].

The measurement of immunoglobulin G can be a useful diagnostic tool for certain conditions, if indicated by certain symptoms [160]. Clinically, measured IgG antibody levels are generally considered to be indicative of an individual's immune status to particular pathogens. A common example of this practice are titers drawn to demonstrate serologic immunity to measles, mumps, and rubella (MMR), hepatitis B virus, and varicella (chickenpox), among others. Besides that, IgG antibodies are also extracted from donated blood plasma and the antibodies could be used as a therapeutic known as intravenous immunoglobulin. This is used to treat immune deficiencies, autoimmune disorders and infections [159]. Since the Protein A has been immobilised on the sensing area of the Love wave sensor and the affinity between Protein A and IgG is strong, IgG

will be bound with Protein A, as in figure 4.4, and measured by the Love wave sensor in this study.

The first experiment in this section was conducted to verify whether the sensor was in a stable state when IgG molecules bound with Protein A molecules are immobilised on the sensing area of the sensor. The processes of the experiment include three parts. First part was to remove whole particles on the sensing area and clean the device. The cleaning method was the same as the previous description in chapter 4.1. Second part was to immobilise a layer of Protein A molecules on the gold sensing area. Third part was to measure IgG solution with a concentration in different droplets. Because a Protein A layer had been immobilised on the sensor, the IgG molecules in the test specimens would be captured by Protein A. Although the sensing area of the device would be immersed in the liquid media during the measurement process, the electrodes were protected under the PMMA layer. Hence, the electrodes of the sensor could not touch the liquid and there was no short circuit problem. The processes of immobilising Protein A on the gold sensing area were in the following description. First, a 2μl Protein A droplet (Invitrogen, 10-1011) with a concentration of 15mg/ml was arranged on the sensing area. After 15 minutes, the solvent of the Protein A solution evaporated naturally, then the sensing area was rinsed by PBS to remove the molecules of Protein A that were not firmly immobilised on the surface. The next step was to arrange a 2μl IgG solution (IgG, from human serum, Sigma, I2511) with a concentration of 0.01mg/ml on the sensing area, then wait for 15 minutes to let the IgG molecules bind with Protein A molecules naturally. Then the sensing area was rinsed with PBS to remove the IgG molecules that were not firmly bound with Protein A molecules on the surface. Afterwards, the surface of the sensing area was dried by nitrogen stream and the frequency shift of the sensor was measured. After measurement, the sensing area was cleaned completely by rinsing and treated with plasma. Then the whole experimental processes were repeated 5 times, and the results of measurements are shown in figure 4.5.

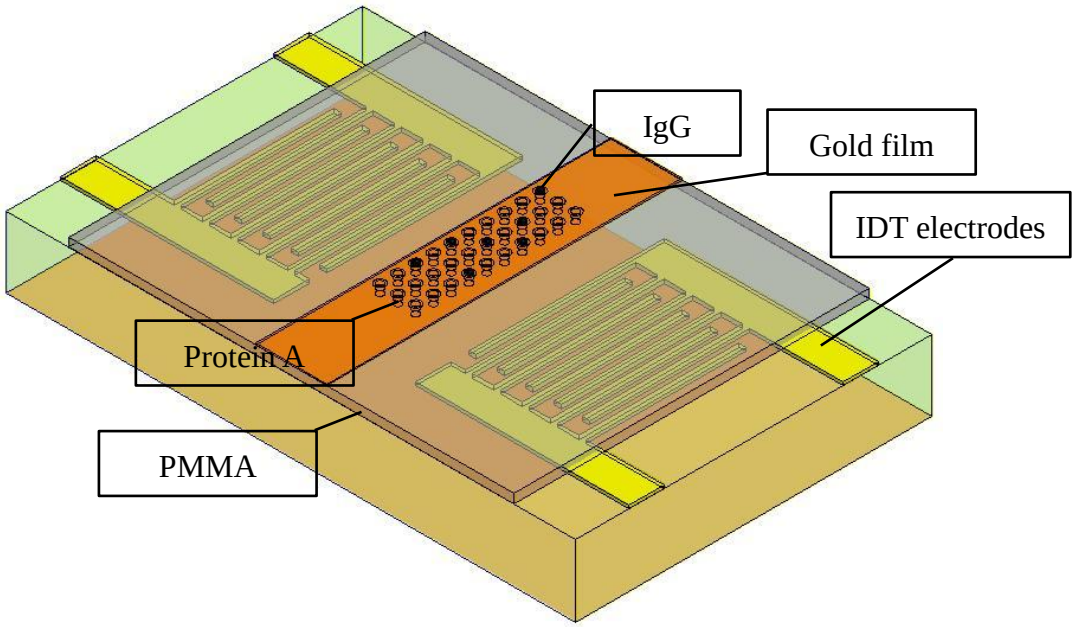

Figure 4.4 IgG Measurement on Love wave sensor. The sensing area is a gold film with 20nm thickness and Protein A molecules are saturated on this region. The frequency shift of the device is measured after IgG is arranged on the sensing area to bind with Protein A.

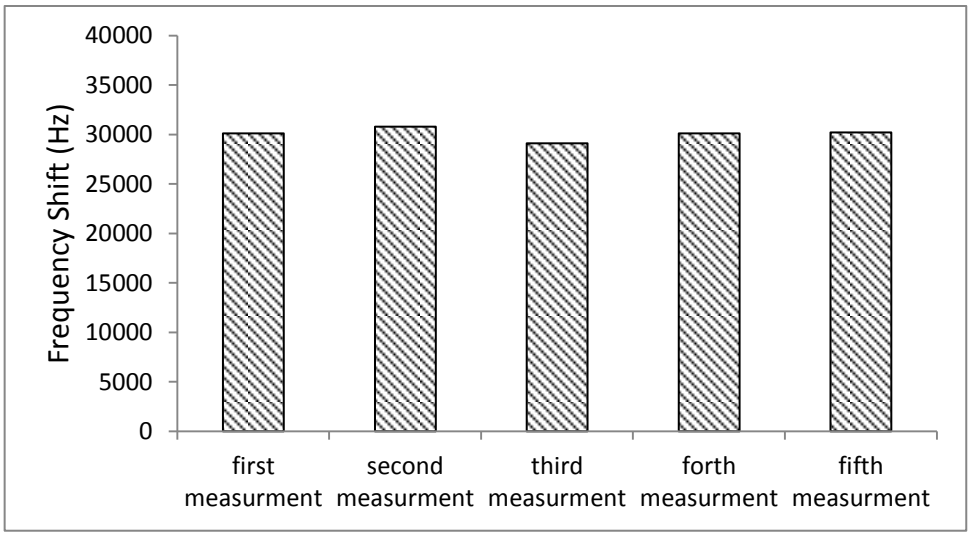

Figure 4.5 The results of measuring frequency shift of the IgG solution with the concentration 0.01mg/ml. The experiments are repeated 5 times, and the median of measurements is 30.1 KHz. The variations among these 5 measurements are less than 1 KHz. This experiment demonstrates that duration of 15 minutes is enough to let IgG molecules bind with Protein A firmly on the sensing area, and that the binding is insoluble by washing.

In the next experiment, the relationship between frequency shift and concentration of IgG solution was investigated. Before each measurement, the sensing area of the sensor was completely cleaned with rinsing by PBS, treated with plasma, and dried with nitrogen

stream. The protein A layer was established according to the method that was descripted in the above paragraph. Afterwards, a 2μl IgG solution (IgG, from human serum, Sigma, I2511) with a concentration of 0.01mg/ml was arranged on the sensing area, and then waited for 15 minutes to let the IgG molecules bind with Protein A molecules naturally. Next, the sensing area was rinsed by PBS to remove the IgG molecules that were not firmly bound with Protein A molecules on the surface. After that, the surface of the sensing area was dried by a nitrogen stream, and the frequency shift of the sensor was measured. According to the above processes, the experiments used different concentrations of IgG solutions were conducted. The IgG concentration range was from 0.01mg/ml to 0.1mg/ml. There were five measurements in each concentration, and the deviations of the frequency shift were all less than 2 KHz. The results of the experiments are displayed in figure 4.6.

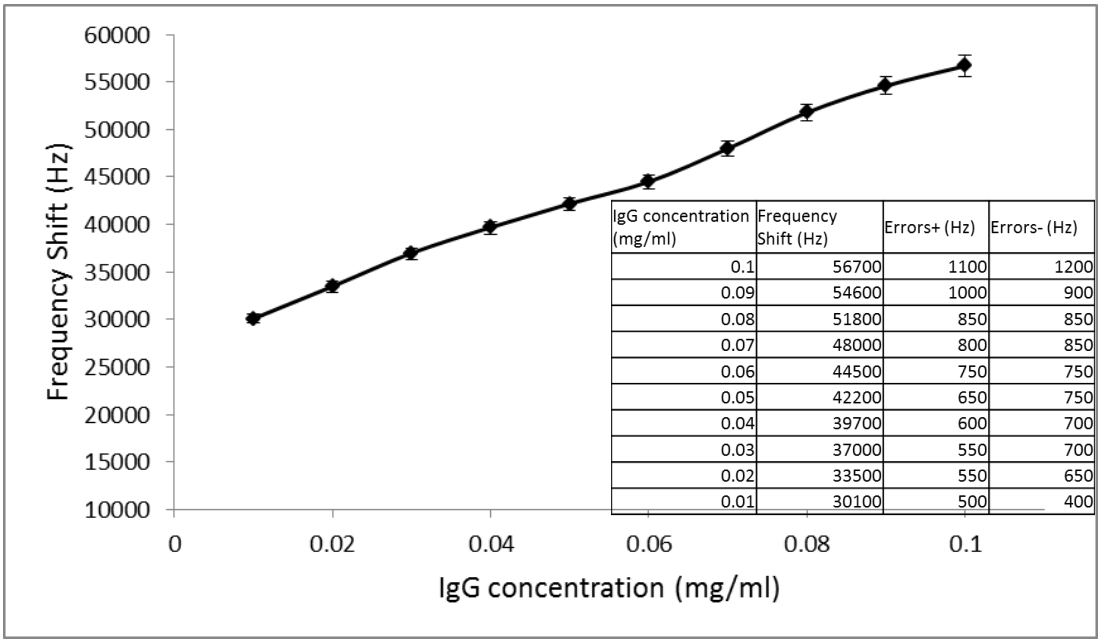

IgG concentration (mg/ml)	Frequency Shift (Hz)	Errors+ (Hz)	Errors- (Hz)
0.1	56700	1100	1200
0.09	54600	1000	900
0.08	51800	850	850
0.07	48000	800	850
0.06	44500	750	750
0.05	42200	650	750
0.04	39700	600	700
0.03	37000	550	700
0.02	33500	550	650
0.01	30100	500	400

Figure 4.6 The results of measuring frequency shift of the different concentration of IgG solution. Higher concentration of IgG solution causes more frequency shift of the sensor, and seems linear between IgG concentration and frequency shift.

4.3 Measurement of Anti-GABA and GABA

GABA (gamma-aminobutyric acid, γ-Aminobutyric acid) is a kind of zwitterion.

These compounds contain an ammonium and a carboxylate group as figure 4.7 [161]. The conformation of GABA depends on its environment. In the standard state (at 25 ℃, 100 kPa) its appearance is white microcrystalline powder. In addition, a more extended conformation is found in solid state, with a trans-conformation at the amino end and a gauche conformation at the carboxyl end, because of the packing interactions with the neighbouring molecules. GABA can also be dissolved in water. Moreover, five different conformations in solution state, some folded and some extended, are found as a result of solvation effects [161]. The conformational flexibility of GABA is important for its biological function, as it has been discovered to bind to different receptors with different conformations. Many GABA analogues with pharmaceutical applications have more rigid structures in order to better control the binding [162, 163].

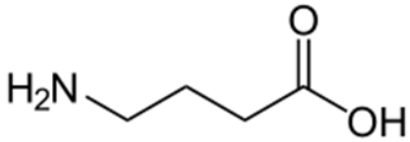

Figure 4.7 The Structure of GABA. Its molecular formula is $C_4H_9NO_2$ and molar mass is 103.12 g/mol. In the standard state (at 25 ℃, 100 kPa) its appearance is white microcrystalline powder. The density of GABA is 1.11 g/ml. In 100ml water, it can dissolve 130g GABA. Its melting point and boiling point are 203.7 ℃ and 247.9 ℃, respectively [161].

GABA was first investigated in the late nineteenth century and was known as a plant and microbe metabolic product at that time. In 1950, GABA was discovered to be an integral part of the mammalian central nervous system [164]. GABA can be synthesized from glutamate using the enzyme L-glutamic acid decarboxylase and pyridoxal phosphate as a cofactor in the brain. Besides that, GABA is converted back to glutamate by a metabolic pathway called the GABA shunt, which the process converts glutamate into the principal inhibitory neurotransmitter [165-167].

GABA is the main inhibitory neurotransmitter in the mammalian central nervous system. It plays an important role in regulating neuronal excitability throughout the

nervous system. For example, GABA is a key factor of the regulation of muscle tone in humans [168]. Although it can be regarded as an amino acid in chemical terms, GABA is rarely referred to as such by the scientific communities, because GABA is not considered to be incorporated into proteins. In mammalian, GABA works on inhibitory synapses in the brain by binding to specific transmembrane receptors in the plasma membrane of both pre- and postsynaptic neuronal processes. This binding causes the opening of ion channels to allow the charged ions (chloride ions or potassium ions) entering or leaving the cell. When net chloride flows out of the cell, GABA is excitatory or depolarizing. On the other hand, when the net chloride flows into the cell, GABA is inhibitory or hyperpolarizing. When the net flow of chloride is close to zero, the action of GABA is shunting. Shunting inhibition has no direct effect on the membrane potential of the cell. However, it minimizes the effect of any coincident synaptic input, by decreasing the electrical resistance of the cell's membrane. A developmental switch in the molecular machinery controlling the concentration of chloride inside the cell is responsible for the changes in the functional role of GABA between the neonatal and adult stages. Consequently, the role of GABA changes from excitatory to inhibitory as the brain develops into adulthood [169].

Two general classes of GABA receptor are known: $GABA_A$ in which the receptor is part of a ligand-gated ion channel complex, and $GABA_B$ metabotropic receptors, which are G protein-coupled receptors that open or close ion channels via intermediaries (G proteins) [164]. Neurons that produce GABA are called GABAergic neurons, and have mainly inhibitory action on receptors. For example, Medium Spiny Cells are a type of typical inhibitory CNS GABAergic cells. In mammals, some GABAergic neurons, such as chandelier cells, are also able to excite their glutamatergic counterparts [170]. There are several papers and clinical reports to link GABA to mood disorders and depression [171-174]. Depression is usually associated with decreased GABAergic function, while various antidepressant manipulations incline to increase it [175]. Low GABA function is

proposed to be an inherited biological marker of vulnerability for depression. Positive modulators of GABA-A receptors can have antidepressant actions, while GABA-A negative modulators often produce depression. There is more evidence for the role of GABA in depression [176, 177].

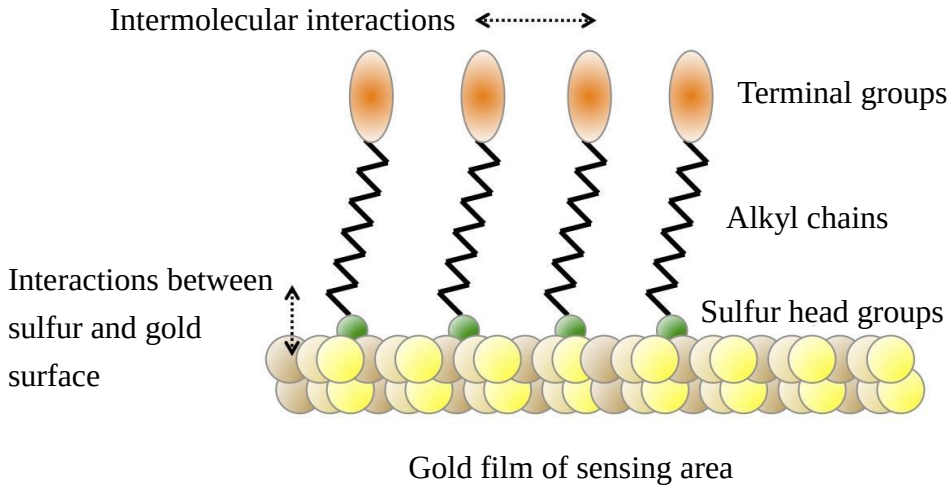

Figure 4.8 The binding between Anti-GABA molecules and gold film sensing area. The Anti-GABA consists of sulfur head groups, alkyl chains, and terminal groups. A gold-sulfur bond is strong, not only involving inorganic sulfur ligands but also thiolates. Gold has a high electronegativity so it forms moderately strong bonds to sulfur. This bond is widely employed to attach biological linkers, functional groups and other molecules to Colloidal gold nanoparticles for research purposes [185].

The conventional method to measure concentrations of GABA under the extracellular conditions is by using liquid chromatography, with electrochemical detection by pre-/post-column derivation [178-181], fluorescence, micellar electro-kinetic chromatography and laser-induced fluorescence detection [182-184]. However, the disadvantages of chromatographic methods are baseline drift and additions of solvent and internal standards [185]. Moreover, it is very difficult to detect GABA directly, because of its insensitive to spectroscopic method. Therefore, it is necessary to develop a simple, rapid and reliable method for direct measurement of GABA, and the Love wave sensor is an attractive choice. The first thing needed to consider was how to immobilise GABA on the Love wave sensor. It is difficult to directly bind GABA with gold sensing film on the sensor because there are no chemically specific gold-GABA bonds (in contrast to the strong gold-sulfur bond that

forms when thiols are immobilised on a gold surface). Nevertheless, I investigated whether any non-specific binding occurred by arranging solutions of GABA on the gold sensing area of the device. However, the measurement results showed that there was almost no frequency shift. This result implied that the binding between GABA and gold was weak and most GABA molecules were removed from the surface of the sensor after rinsed with buffer solution. However, if binding GABA molecules with its conjugate members, it is possible to fix the later on the gold film, then measuring GABA by Love wave sensor [185]. In this study, GABA powder was purchased from Sigma-Aldrich (Sigma, A2129) and its conjugate members, Anti-GABA, can also be provided from the same company (Sigma, A2052). In addition, it can be known that there is a thiol structure within the Anti-GABA molecule from the instructions of the product. Thiol structure organize a stable binding on gold surfaces by virtue of the strong affinity between sulfur head groups and gold substrates, and to intermolecular interactions (e.g., van der Waals interaction between the alkyl chains and electro- static interactions between the sulfur head groups and between charged or polar terminal groups) (figure 4.8) [185]. Because it is easy to prepare to immobilise Anti-GABA on the gold film, and its stability under ambient conditions, Anti-GABA was applied to the measurement of GABA.

The first experiment in this section was conducted to verify that the binding between Anti-GABA and gold film of sensing area is a stable state. Before each measurement, the sensing area of the sensor was completely cleaned and the clean method was described in chapter 4.1. Next, a 2μl Anti-GABA droplet (Sigma, A2052) with a concentration of 10mg/ml was dropped by using a pipette. After 15 minutes later, the solvent of the Anti-GABA solution evaporated naturally, and the sensing area was rinsed with PBS. The aim of this process was to remove the unfirmly immobilised Anti-GABA molecules on the surface. After that, the surface of the sensing area was dried by nitrogen stream, and the frequency shift of the sensor was monitored. Then the experimental processes were repeated 5 times and the results of measurement are shown in figure 4.9.

Now, the immobilisation of Anti-GABA on the sensor is stable has been confirmed. Because I would like to arrange as many Anti-GABA molecules on the surface of the sensing area as possible, the experiments to investigation the saturation concentration of Anti-GABA on the sensing area were designed. The processes of the experiments are as follows: First, the sensing area of the sensor was rinsed in PBS (Sigma, D8537) for 30 minutes. After that, the nitrogen stream was used to dry the surface. Next, the sensor was treated in the oxygen Plasma Asher (100Watt, 180 seconds). The next step was to arrange a 2μl Anti-GABA solution (Sigma, A2052) with the concentration of 1mg/ml on the sensing area. After 15 minutes, the solvent of the Protein A solution had been evaporated naturally, and only left the Anti-GABA molecules on the sensing area. Then, redundant Anti-GABA molecules that were not firmly immobilised on the sensing area will be removed by PBS rinsing for 10 minutes. Afterwards, there were still some Anti-GABA molecules immobilised on the sensor and the frequency shift of the device was measured. After measurement, the sensing area is cleaned again to remove all particles on the sensor. Next, the measurement with the same concentration of Anti-GABA will be repeated 5 times. According to the above processes, the frequency shifts with different concentrations of Anti-GABA solution from 1mg/ml to 10mg/ml were measured. The relationship between frequency shift and concentration of Anti-GABA is displayed in the figure 4.10. The data points in the figure are the medians for measurements in each Anti-GABA concentration. The deviations in each measurement of concentration were all less than 2 KHz, and shown in the error bars in the figure 4.10. When the concentration of Anti-GABA was less than 7mg/ml, it seemed to be linear between the frequency shift and the concentration. A higher Anti-GABA concentration could lead to more frequency shift. However, when the Anti-GABA concentration exceeded 7mg/ml, the frequency shift of the sensor could only increase from 75.6 KHz to 76.6 KHz. The change of frequency shift in this range (from 7mg/ml to 10mg/ml) was less than the measurement deviations, so the increase of the frequency shift can be neglected. It can be considered as saturation concentration was

7mg/ml.

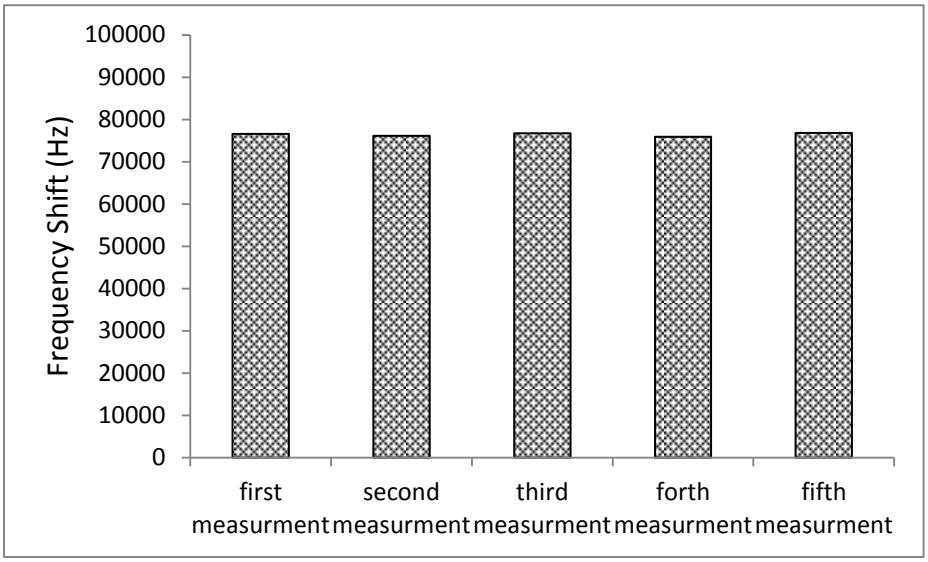

Figure 4.9 The result of measuring frequency shift of Anti-GABA solution with the concentration 10 mg/ml. The experiments are repeated 5 times and the median of measurements is 76.6 KHz. The variations among these 5 measurements are less than 1 KHz. This experiment demonstrates that the binding between Anti-GABA molecules and gold film of sensing area is stable and insoluble.

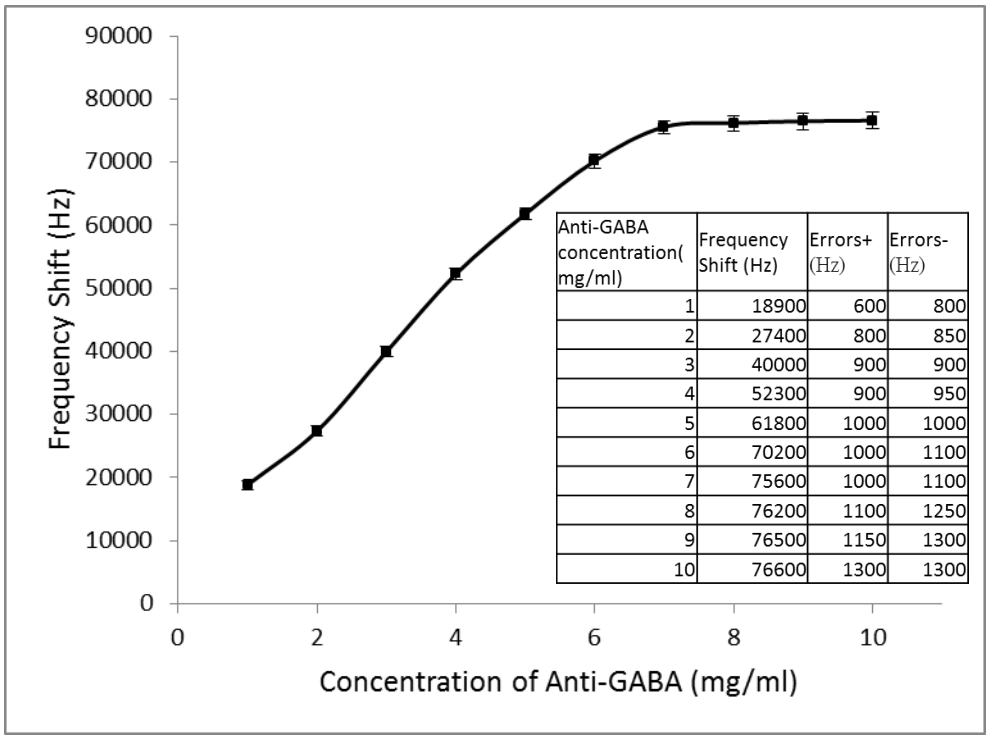

Anti-GABA concentration(mg/ml)	Frequency Shift (Hz)	Errors+ (Hz)	Errors- (Hz)
1	18900	600	800
2	27400	800	850
3	40000	900	900
4	52300	900	950
5	61800	1000	1000
6	70200	1000	1100
7	75600	1000	1100
8	76200	1100	1250
9	76500	1150	1300
10	76600	1300	1300

Figure 4.10 The relationship between frequency shift and Anti-GABA concentration. Under the saturation concentration of 7mg/ml, frequency shift rises almost linearly with the increase of Anti-GABA concentration. When the concentration of Anti-GABA is higher than 7mg/ml, frequency shift does not change significantly, because the sensing area is almost saturated by the Anti-GABA molecules.

Since the Anti-GABA molecules had been successfully immobilised on the sensor,

they could capture GABA molecules in the test specimens and the frequency shifts of the sensor were monitored. The processes of the experiment include three parts. First part was to clean the device before each measurement and the cleaning method according to the description in chapter 4.1. Second part was to immobilise a layer of Anti-GABA molecules on the gold sensing area and it had been complete as the above paragraph. Third part was to arrange various concentrations of GABA solution on the sensor and the frequency shifts of the device were measured. The volume of the target GABA solution was 2μl. In addition, the time for GABA molecules binding with Anti-GABA molecules naturally was 15 minutes. After 15 minutes, the sensing area was rinsed with PBS to remove the redundant GABA molecules that were not well bound with Anti-GABA molecules on the surface. Next, the surface of the sensing area was dried by nitrogen stream, and the frequency shift of the sensor was measured. The range of concentration of GABA solution was from 0.01mg/ml to 0.1mg/ml. There were five measurements in each concentration, and the deviations of the frequency shift were all less than 2 KHz. The results of the experiments are displayed in the figure 4.11.

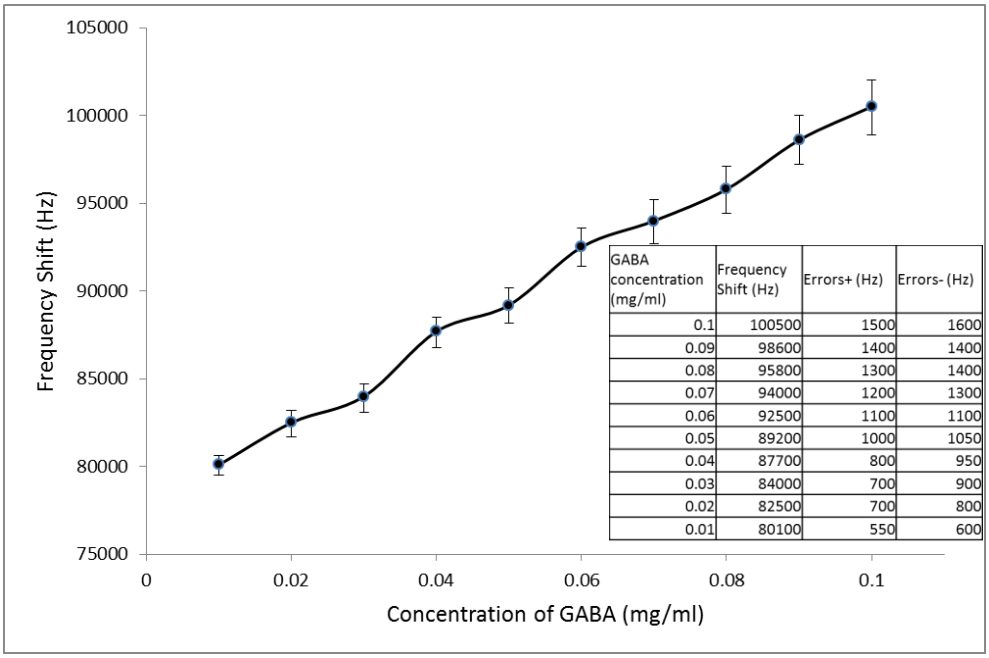

GABA concentration (mg/ml)	Frequency Shift (Hz)	Errors+ (Hz)	Errors- (Hz)
0.1	100500	1500	1600
0.09	98600	1400	1400
0.08	95800	1300	1400
0.07	94000	1200	1300
0.06	92500	1100	1100
0.05	89200	1000	1050
0.04	87700	800	950
0.03	84000	700	900
0.02	82500	700	800
0.01	80100	550	600

Figure 4.11 The result of measuring frequency shift of the different concentration of GABA solution. With the increased concentration of GABA solution, frequency shift of the sensor rises linearly.

The Love wave biosensor in this study has the capability to work in dry or liquid states (not at the same time). Under the dry state, the experiments of measuring Protein A, IgG, Anti-GABA, and GABA molecules had been conducted and the results could confirm that the mass variations of the test specimens reflected the linear changes of frequency shifts of the device. However, if the measurement environment of the sensor was only immersed in the liquid, the frequency shift of the device would become unpredictable. Although the frequency shift of the device could still reflect the mass changes of the solutions, other variables (viscosity, conductivity of the solutions) would influence the measurement results. The result of figure 4.1 provides enough information to explain the suitable working environment of the Love wave sensor in this study is in the dry state. Therefore, it is necessary to develop another detection method to aid the Love wave sensor working in the liquid media. In addition, the aim of augmenting these measurements with electrochemical impedance ones is to enable the Love wave sensor to be used to accurately characterise the test specimens in pure liquid state. The electrochemical impedance measurement is especially applied in the liquid environment so an impedance sensor was selected to work together with the Love wave sensor. The details of working theory of the impedance sensor and how these two sensors cooperate to measure targets are in the following chapter.

Chapter 5 Experimental results of impedance sensor

5.1 To add an impedance sensor on the Love wave sensor

In the previous section 2.4, when fabricating the Love wave sensor, I deposited a 20 nm thick gold film to act as the sensing area. This sensing area is rectangular in shape and has a 100 μm gap in the middle. The direction of the gap is perpendicular to the direction of propagation of the Love wave. This allows the two separated gold films to be used as the electrodes for electrochemical impedance sensing. Thus, the Love wave sensor in this device can be used to measure the mass of the immobilised analyte under both dry and wet conditions, with the impedance sensor function detecting the electrochemical impedance of the same immobilised analyte in liquid conditions alone. The biggest advantage of the impedance sensor is that it is sensitive to the surface coverage of molecules bound to the substrate and insensitive to the mechanical strength (viscoelasticity) of the bonds involved (strong or weak links) – the impedance measurements depend on the ability of redox and ionic species to diffuse around the adsorbed molecules and interact with the underlying metal electrode i.e. impedance measurement are sensitive to the *area* of the electrodes that are not covered by adsorbed molecules. In contrast, the Love wave sensor is sensitive to the *mechanical rigidity* of the coupling. This mechanical rigidity is especially sensitive to the solvation state of the bound molecules and thus to Love wave measurement in liquids. It is important to appreciate that although Love wave measurements are sensitive to the adsorption of molecules in liquids, absolute calibration of the amount (mass) of material adsorbed is problematic if there is a significant (unknown) viscoelastic component to the linkage between the molecules and the substrate. Therefore, using information from the electrochemical impedance results can provide more information about the analyte and the accuracy (or calibration) of the Love wave sensor measurements in a liquid environment (n.b. the titanium deposition calibration method was performed under dry conditions and it would be expected that the coupling between a metal film and the substrate would be much

more rigid than for macromolecular organic molecules such as IgG and Protein A). Usefully, neither of these two sensors requires special reagents so they are label-free sensors. In addition, the fabrication of the device is not too complicated and it is easy to miniaturise. This may make the system suitable for point-of-care diagnostics and bio-material detection. Moreover, the working frequency of the Love wave sensor in this study was about 115 MHz, and the frequency range of testing signals used in electrochemical impedance sensor was from 10 Hz to 1 MHz, respectively. Because the frequency ranges of signals used in these two sensors were very different, the problem of signal cross-talking or interference is avoided.

The theory of an electrochemical impedance sensor has been well introduced in electrochemical technology books [186]. Like all electrochemical measurement techniques, employing impedance detection for biosensor technology has some fundamental characteristics. These dictate the electrical circuits used in the electrochemical measurement. The circuits generally detect an AC current following the application of an AC potential, which is the most commonly used method for impedance experiments. Alternating current (AC) voltage sources are usually specified to have a sinusoidal wave shape and defined frequency. Both voltage and current oscillate as in figure 5.1. When the voltage or current is applied to a system that has capacitive and resistive components, this oscillation causes a phase difference between the current and voltage, because AC excitation signal and sinusoidal current response are based on Ohm's law. As can be seen in figure 5.1, the sinusoidal fluctuation of both current and potential show a difference, this difference, Φ, is a function of the AC resistance (or impedance). The relationship between current and voltage can be described by the equation (5.1) (Z: impedance, V_t: voltage in a time, I_t: current in a time, V_0: voltage at zero point, I_0: current at zero point, ω: frequency, t: time).

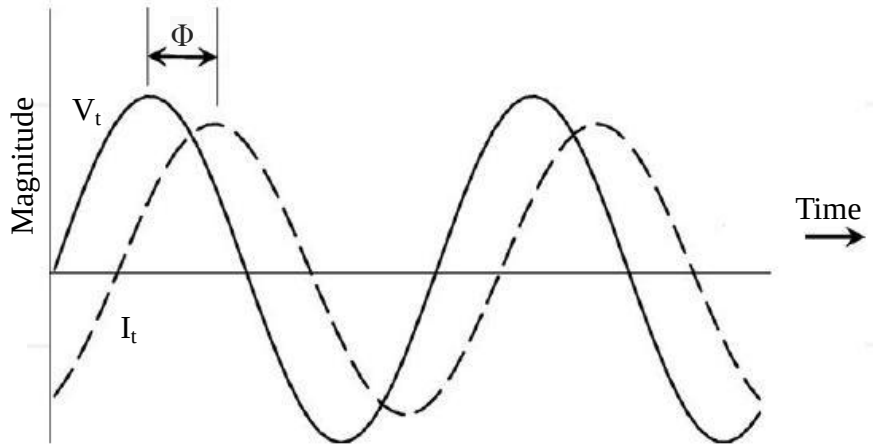

Figure 5.1 Alternative current (AC) is a kind of signal that magnitude varies with time and the range is from positive to negative. Φ is the phase difference between voltage (V_t) and current (I_t).

In equation (5.1), impedance is represented by Z, and Φ is a phase shift of AC; furthermore this phase shift is angle of the impedance curve in a Nyquist plot. This theory has been used in biosensor technology for a long time; its aim is to examine the electrical characteristics of an electrode interface after formation of an immobilised layer and/or electron transfer interactions between solution or surface bound molecules and an underlying metal electrode. In general, the presence of charged groups of molecules in the solution between the two electrodes influences the system impedance, and those in layer nearest the electrode surface have the greatest influence on electrical characteristics of electrode. These ions cause changes in the distribution of electrode surface charge and consequently a variation in the capacitive current. The electrical measuring circuit of the system measures this as the impedance increases or decreases [187].

$$\mathrm{Z} = \frac{V_t}{I_t} = \frac{V_0 \sin(\omega t)}{I_0 \sin(\omega t + \Phi)} = Z_0 \frac{\sin(\omega t)}{\sin(\omega t + \Phi)} \qquad (5.1)$$

An advantage of electrochemical impedance sensor over other electrochemical measurement techniques is the opportunity to model the system response as an electrical circuit that comprises a combination of resistors and capacitors. The model circuit is designed so that it will have the same electrical response as the measured Nyquist plot for

the electrochemical system. Figure 5.2 shows a typical electrical circuit model for an impedance curve obtained from simple electrochemical measurements. As you can see there are both resistors and capacitors in figure 5.2. The series capacitance element (C_{test}) and resistance element (R_e) represent the electrode surface impedance and the series resistance element (R_s) corresponds to the solution resistance. The capacitor C_d represents capacitance of electrical double layer between electrode and solution, resistor R_e represents resistance of the electron transfer interactions on the surface of the electrode. In typical electrochemical impedance measurements, the Nyquist plot of the electrode does not start from the (zero, zero) point; this means that the solution in the cell has a non-zero resistance (If it started at the zero point, it would mean the resistance of solution "R_s" does not exist). Therefore a resistance element (R_s) is always added in circuit model. The next part of the curve (going from a high to low frequency) shows a semi-circular impedance curve; this is characteristic of resistance occurring in parallel with capacitance. Thus R_e is added to the capacitance, C_d, which occurs because of the electrical double layer. Variations in the impedance curve will result in changes to the structure and values in the electrical circuit model; for example, a circuit element can be added in series after the R_e circuit element [188]. This additional circuit element, a capacitor C_{test}, represents the capacitance generated by the layer of test specimen on electrode surface. This capacitor occurs when an immobilised layer is deposited on the electrodes, the dielectric constant of which is different from redox couples in solution.

The value of C_{test} is related to the interaction between the electrode surface and solution and can correspond to a mass transfer towards electrode surface. However, this interaction is not only due to diffusion effects, but it also reflects electron transfer to/from molecules on the surface and in solution. Therefore at lower frequencies, after the semi-circle, the Nyquist curve varies in a linear shape (a straight line). The interaction between electrode surface and solution, determine the relative values of C_{test} and electrode

surface resistance (R_e). This balance can be influenced by mass transfer and after any increase in mass transfer the value of C_{test} gets larger relative to the electrode surface resistance (R_e) [189-191]. As you can see there are a number of factors in the impedance that contribute to the design of a circuit model. These include the surface of the electrode, content of the solution and characteristics of any redox couples present.

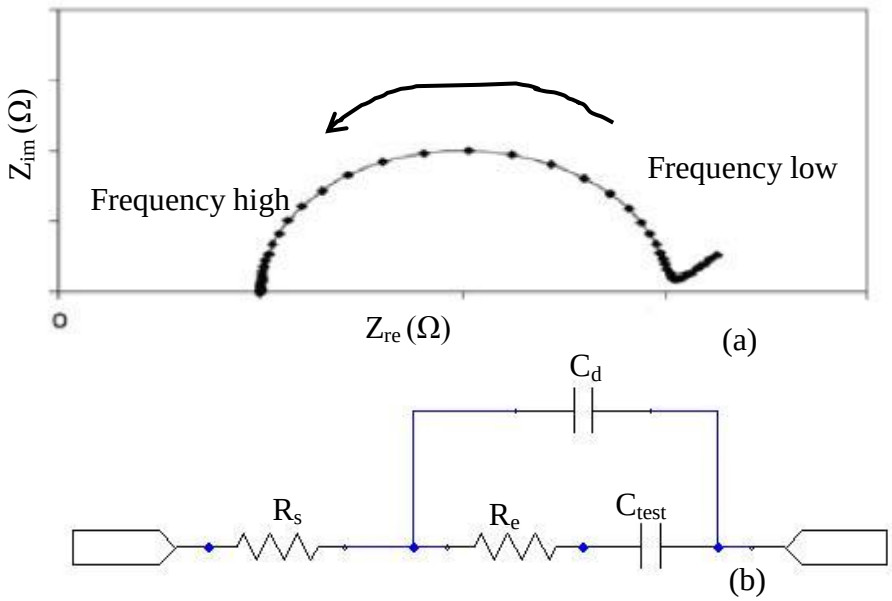

Figure 5.2 (a) Nyquist plot curve of the measurement for impedance spectroscopy. The x axis is real part impedance and y axis is imaginary part impedance. The data points in this figure are measured from the same sample with a frequency range. (b) Equivalent circuit model for impedance sensor. The Nyquist plot curve belongs to the Faradaic impedance case. C_d represents capacitance of electrical double layer between electrode and solution. R_e represents resistance of the interaction on the surface of the electrode. R_s represents resistance of the solution. C_{test} represents capacitance which is related to the layer of test specimen on electrode surface.

Impedance sensors which are based on electrochemical impedance spectroscopy (EIS) methods are being developed as high quality substitutes for fluorescent staining, magnetic counting, microdialysis, plate-culture techniques, and other clinical laboratory methods. For example, electrochemical biosensors offer a number of advantages over optical, ultrasonic, magnetic, and other diagnostic principles employed in clinical and biomedical settings. The increased interest in application of electrochemical technology as a basis for point-of-care biomedical diagnostic devices and sensors arises from high sensitivity,

selectivity, temporal and spatial resolution, rapid response, simplicity of rapid screening procedures, label-free non-invasive sensing, cost effectiveness, versatility, flexibility of design, easiness of integration, compatibility with micro-fabrication technology, high throughput screening, and the ability to perform in vivo and respond adequately to the dynamic nature of living systems [192]. The small size of electrochemical devices allows them to be used in microfluidic products and sensor arrays when simultaneous detection of several analytes present in low-volume sample is required. One of the examples of in vivo application of electrochemical technology is the use of fast scan voltammetry with implanted microelectrodes, which produced a unique fingerprint for dopamine with excellent selectivity and sensitivity [193]. Microelectrode arrays can often reliably record neural activity for several months after the implantation. Since the pioneering works of Schwan in 1950s, the foundation was laid for the impedance analysis and interpretation of biological cells dispersions [194]. Since then many researchers have characterized biological colloidal suspensions [195, 196], developed “Coulter counters” and capacitive cytometers for bio-particles detection [197, 198], designed enzyme-based biosensors for glucose monitoring [199], and practiced electrophoretic and dielectrophoretic separations of drugs, proteins, cells, DNA, and pathogenic bacteria [200-202]. Impedance spectroscopy has been used to study biomedical and pathogenic cell cultures, which is extremely useful for both medical diagnostics of many major clinical complications and early detection and prevention of infectious diseases [203].

To my knowledge, there is no related research about combining Love wave sensor with impedance sensor in the same device. As a result, I would like to invent a new type of sensor that can take advantage of these two sensors in one chip to measure analytes and determine or calibrate the accuracy of solution based Love wave measurements.

5.2 The calibration of the impedance sensor

There are many factors that influence the measurement data of impedance sensors. For example, electrical conductivity of solution is very important for choosing frequencies. In high electrically conducting solutions, i.e. those in which the solution contains high ion concentrations, low frequencies can be used, especially in the presence of a redox couple solution. As indicated above, a potential must be applied to gain a proper current signal, this potential is called the AC excitation signal. When the solution includes redox couple such as ferricyanide or ferrocyanide, according to the oxidation or reduction potentials of the materials, the small applied AC potential corresponds to the beginning of the electrochemical transformation. In order to obtain higher sensitivities when doing these measurements, use of the faradaic impedance model is proposed as a method to allow lower frequencies to be used. This is because at these frequencies the reduction/oxidation properties of redox couples allow the electrons (which are involved in this oxidation/reduction) to move more easily. This transportation can be measured as an electron transfer resistance. As stated above, the electrical circuit model is constructed by examining the characteristics of the impedance curve. Thus, impedance spectroscopy provides a sensitive and label free detection due to it being sensitive to the electrode surface character. Electrode surface modification plays a key role in impedance measurements. If the modification is inhomogeneous on the electrode surface or there are gaps in it, allowing a direct interaction between the bare electrode surface and electrolyte, the electrons can pass through the electrode surface without confronting any electrical resistance. This will strongly influence the impedance spectrum. In this case of inhomogeneity, the capacitance element of the circuit model is redefined as a constant phase (Warburg) element to solve this problem. Based on the above considerations, it is necessary to calibrate the sensor and regulate the measurement conditions. In this study, the sensor was connected to an impedance analyser (HP, 4192A), which is capable of

varying the measuring frequency from 5 Hz to 13 MHz and directly reporting the measured real and imaginary parts of the impedance. The magnitude of AC excitation signal was chosen to be 100mV so as to provide a small, rather than large, perturbation to the solution redox composition. Importantly, the solution contained both $K_3Fe(CN)_6$ and $K_4Fe(CN)_6$ to provide the redox couple ($[Fe(CN)_6]^{3-}/[Fe(CN)_6]^{4-}$) and their concentrations were 5 mM. The equivalent circuit model of total measurement system is shown as figure 5.3.

The cell of the system was constructed using a PDMS (Polydimethylsiloxane) ring to define the area of electrodes exposed to the solution, as shown in figure 5.4. The ring was stuck across the two electrodes with the gap was bisecting the ring. The calibration of total measurement system in this impedance sensor was conducted according to the operation manual of the impedance analyser. 2μl the redox couple solution was dropped inside the PDMS ring to form the electrochemical cell. The observed value of $R_{connect}$ was 46 Ω and this value was far less than other resistances in this system, so it can be neglected when analysing the measurement data. After calibration, the values of R_s (307 Ω), R_e (540 KΩ), and C_d (0.105 nF) were obtained respectively when fitting the data to figure 5.2.

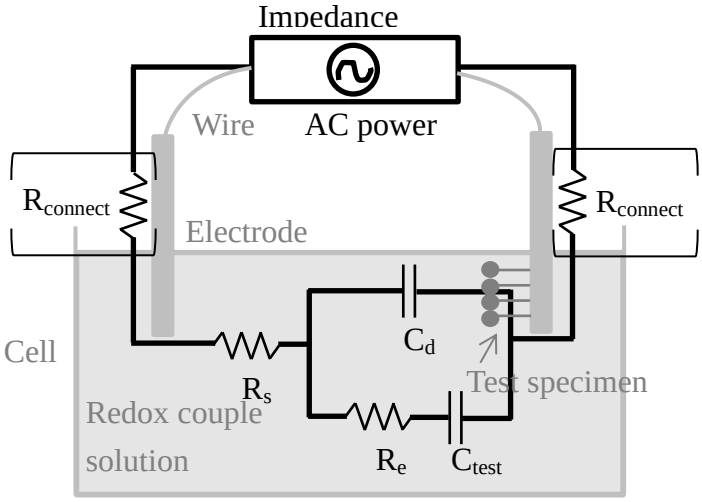

Figure 5.3 The equivalent circuit model of total measurement system in this impedance sensor. $R_{connect}$ represents resistance of wire and the connection interface with the electrode. After calibration, $R_{connect}$ can be neglected because their values are far less than other resistors in this system. C_d represents electrical double layer capacitance. R_e represents interaction electrode resistance. R_s represents the redox couple solution resistance. C_{test} represents capacitance that generated by the interaction of surface of the electrode and solution so the test specimen affects the value of C_{test} significantly.

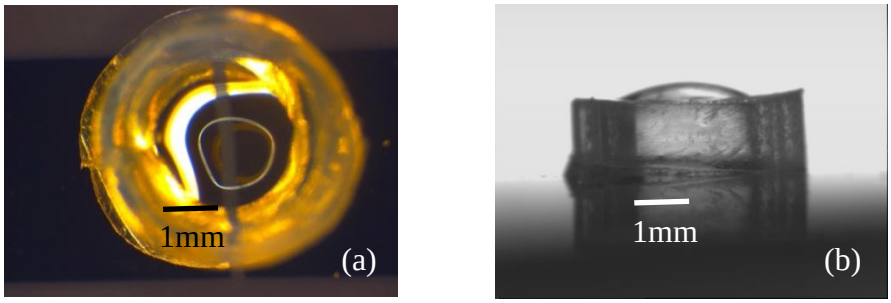

Figure 5.4 (a) Top view of the PDMS cell (b) Side view of the PDMS cell.

Next, the experiment was designed to verify that equivalent circuit model used to describe our impedance sensor is reasonable. Three kinds of conditions (clean, PMMA coated and SAM coated electrodes) were chosen to create different electrode surfaces. Clean electrodes (it will be called as blank in the following description) represent the situation where there was only a redox couple solution in the cell and no other molecules immobilised on the surface of electrodes. PMMA coated represent the condition where there was a PMMA (Polymethylmethacrylate) layer of thickness 52nm on the surface of electrodes. The PMMA layer was spun coated on the electrodes and its thickness was determined by a stylus surface profiler (Dektak 6). SAM coated represents the formation of a thin SAM (Self-assembled monolayer) layer on the surface of electrodes. SAM-modified substrates were prepared as described previous documents [204-206]. The SAM was formed on the surface of the electrodes by first cleaning the device by immersing in piranha solution (30:70 v/v solution of 30% hydrogen peroxide H_2O_2 and concentrated sulphuric acid H_2SO_4) for 5 minutes, and then rinsed by deionized water for 30 minutes. After that, the device was dried by a nitrogen stream and treated under oxygen Plasma Asher (100 Watt, 180 seconds). The next step was to prepare enough solution for all samples to ensure the solution concentration is constant across the sample set. When preparing mixed thiol solutions, prepared a stock solution of each thiol separately, and then mixed them at the proper proportions for the final stock solution. All assembly containers were rinsed with 3-5 ml of solvent. Repeated 2 times and re-cap each container and rinsed all beakers, tweezers, etc., to be used in the experiment. The appropriate volume of solvent

was measured to a clean solution container. The volume of thiol was dispensed into the solvent. Then the solution was shaken for 10 minutes to dissolve. Once dissolved, dispensed the planned volume of solution into each sample container. The thiol solution in this study was hexadecyl mercaptan with concentration 2mM and was purchased from Sigma-Aldrich (1-Hexadecanethiol, 674516 Aldrich). Next, gold electrodes of the impedance sensor were immersed in container containing thiol solution. The device was handled with tweezers and minimized exposure to air. The samples were stored for 48 hours because longer assembly times tend to result in better monolayer packing. After 48 hours, samples were held with clean tweezers and rinsed with solvent for about 10 seconds using a clean solvent bottle. Then samples were dried with a nitrogen stream and placed each sample in a container with fresh solvent and close the cap. The samples were shaken for 3 minutes. Afterwards, all the samples were removed individually and rinsed again for about 10 seconds under a steady stream of ethanol. All samples were dried with a nitrogen stream and placed devices in clean Petri dishes. It is better to minimize time between preparation and use, because SAMs can oxidize over time.

The measurement processes are as follows. First, the surface of ‘control’ electrodes was rinsed in buffer solution (Sigma, D8537) for 30 minutes, and then the surface was dried by a nitrogen stream and treated under the oxygen Plasma Asher (100Watt, 180 seconds) to remove impurities on the sensing area. Next, the cell was filled with redox couple solution and connected the sensor with an impedance analyser, which was controlled by computer. Then the impedance was measured with a frequency scanning from 10 Hz to 10 MHz, and the data (real part impedance and imaginary part impedance) was transferred to the computer. This provided the calibration data corresponding to the impedance response of the particular redox solution being used. After that, a new impedance sensor was connected with a PMMA layer on the surface to the impedance analyser. The impedance of the sensor with a PMMA layer was measured and recorded.

Next, another new impedance sensor with a SAM layer on the surface was connected to the impedance analyser to measure its real part and imaginary impedance. These three sensors were thus measured under the identical conditions and any variation in the impedance response was due to the surface of the electrodes. The experimental result of these three sensors is displayed in figure 5.5.

The Nyquist plot of experimental results above illustrates the impedance of the total measuring system. Since the calibration values of R_s (307 Ω), R_e (540 KΩ), and C_d (0.105 nF) are known in this system, the value of C_{test} under different surface conditions on the electrodes could be calculated from the measured impedance. The capacitances transformed from the measured impedance are shown in figure 5.6.

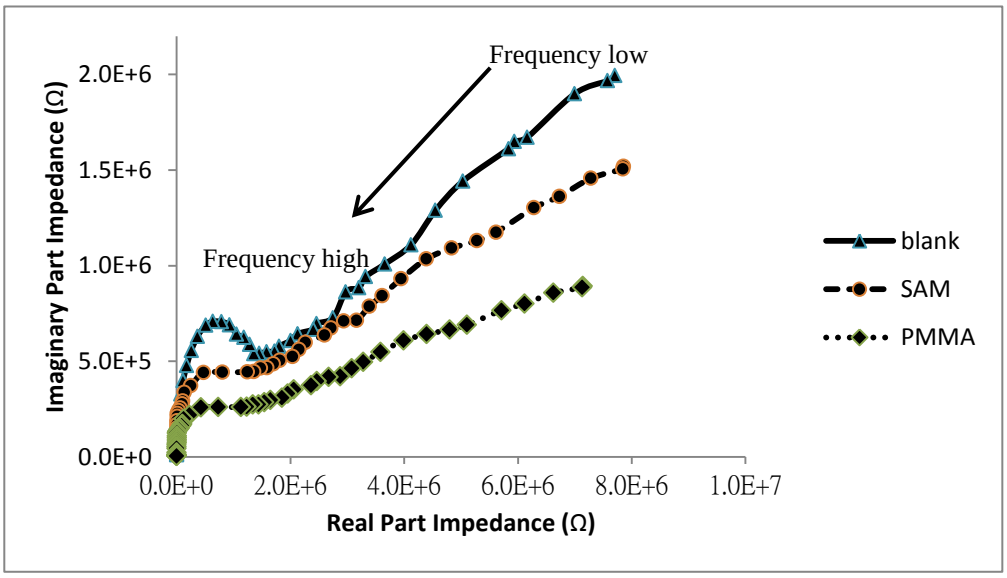

Figure 5.5 The Experimental Result of measuring different surface conditions on impedance sensor. Blank represents that there was only redox couple solution in the cell and no other molecules immobilised on the surface of electrodes. SAM represents that there was a SAM (Self-assembled monolayer) layer on the surface of electrodes. PMMA represents that there was a PMMA (Polymethylmethacrylate) layer with thickness 52nm on the surface of electrodes. The scanning frequency range is from 10 Hz to 10M Hz. The magnitude of AC excitation signal is 100 mV.

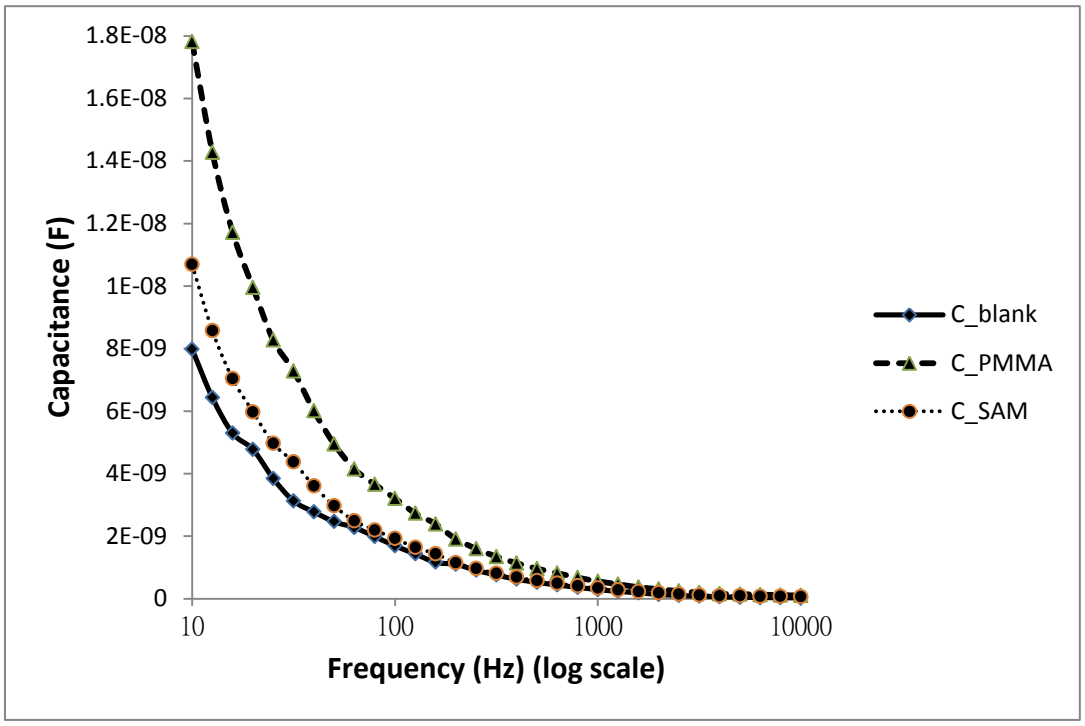

Figure 5.6 The transformation of imaginary part impedance to capacitance for different surface conditions on impedance sensor. C_blank represents the capacitance C_t of nothing on the surface of electrodes except redox couple solution in the cell. C_PMMA represents the capacitance C_t of 52nm thick PMMA layer on the surface of electrodes. C_SAM represents the capacitance C_t of the SAM layer on the surface of electrodes.

With the increase of frequency, the capacitance C_{test} decreases sharply. No matter what the surface conditions I measured, when the measuring frequency is more than 1 KHz, the value of capacitance C_{test} approximates a constant that is much smaller than C_d. This phenomenon explains why the capacitance of double layer C_d dominates the capacitance of total system at high frequencies. However, at low frequencies such as 10 Hz, the value of capacitance C_{test} is much larger than C_d; so C_{test} becomes a main contributor in total system capacitance. Therefore, fixing the measuring frequency at a low value (10 Hz) can be used to obtain significant values of C_{test}. Compared with three different surface conditions (blank, PMMA, and SAM), the highest capacitance occurred in the surface of electrodes with a PMMA layer; this is followed by the surface of electrodes with a SAM layer; the lowest capacitance occurred for the electrodes with a clean, control surface (C_blank). This result demonstrates that to coat or immobilise molecules on the impedance sensors can indeed change their surface capacitance. These changes influence the interaction of

transferring charges between electrodes and solution so that the capacitance value (C_{test}) varies with different surface conditions of the electrodes. As a result, the equivalent circuit model in this study (figure 5.3) works and I can utilise it with the impedance sensor to detect the density of molecules binding on the surface of the electrodes.

5.3 Measurement of Protein A

As mentioned in the previous section 4.1, Protein A is a useful molecule in biochemical research and can be measured with using Love wave sensors. Now Protein A also could be measured with impedance sensor and examine the function of total measurement system. The first experiment in this section is to discover how much time I need to immobilise Protein A on the electrodes of the sensor in order to obtain stable, equilibrium measurements. There were three surface conditions in the following experiment. One is the control condition that I didn't involve any Protein A molecules but included a SAM layer on the surface of the electrodes. Another is to immobilise Protein A molecules on the SAM layer. The last one is to immobilise Protein A directly on the surface of the electrodes. The experimental procedures are described as follows. First, it is necessary to form a SAM layer on the surface of the electrodes as above mentioned in the previous section 5.2. Then the sensor was connected with impedance analyser (HP, 4192A) and the cell on the surface of the electrodes was filled with the redox couple solution. Next, the impedance value of the sensor was recorded every 10 minutes. After 120 minutes, the impedance value was recorded every 30 minutes until 300 minutes. After the measurements, the inside of the cell was cleaned by buffer solution rinsing and treated by oxygen Plasma Asher to remove all the material from the surface of the electrodes. Afterwards, a 2μl protein A solution (Invitrogen, 10-1011) with concentration 25mg/ml was placed in the cell, then the cell was filled with the redox couple solution again. The next step was to connect the sensor with the impedance analyser and the impedance value

was monitored every 10 minutes. After 120 minutes, the impedance value was recorded every 30 minutes until 300 minutes. Next, another impedance sensor without SAM layer on the surface of the electrodes was used to detect directly the Protein A molecules immobilisation. Again, before measurement, inside of the cell was cleaned by buffer solution rinsing and treated by oxygen Plasma Asher to remove impurities on the surface of the electrodes. Next, a 2μl protein A solution with concentration 25mg/ml was arranged in the cell, then the cell was filled with the redox couple solution. Then the sensor was connected with the impedance analyser and measured the impedance value every 10 minutes. After 120 minutes, the impedance value was recorded every 30 minutes until 300 minutes. The result of the capacitance change during the period between 10 minutes and 300 minutes is displayed in figure 5.7. It can be seen that C_SAM is constant. It expresses that the SAM is a stable layer and influence the value of capacitance C_{test} as soon as SAM layer be formed on the surface of the electrodes. Both C_PA and C_SAM_PA (corresponding to Protein A being adsorbed onto clean and SAM modified electrodes) increased steadily from the beginning of the measurement to 120 minutes. Then the values of them did not change much and remained at a steady state for a further 2 hours. This phenomenon could be explained by the quantities of Protein A molecules immobilised on the surface increasing with time from start of the solution being added to the cell, up to a period of 120 minutes. Notably, the value of C_SAM_PA is larger than those of C_SAM or C_PA. This indicates that adding more molecules (SAM and Protein A) on the surface increases the capacitance.

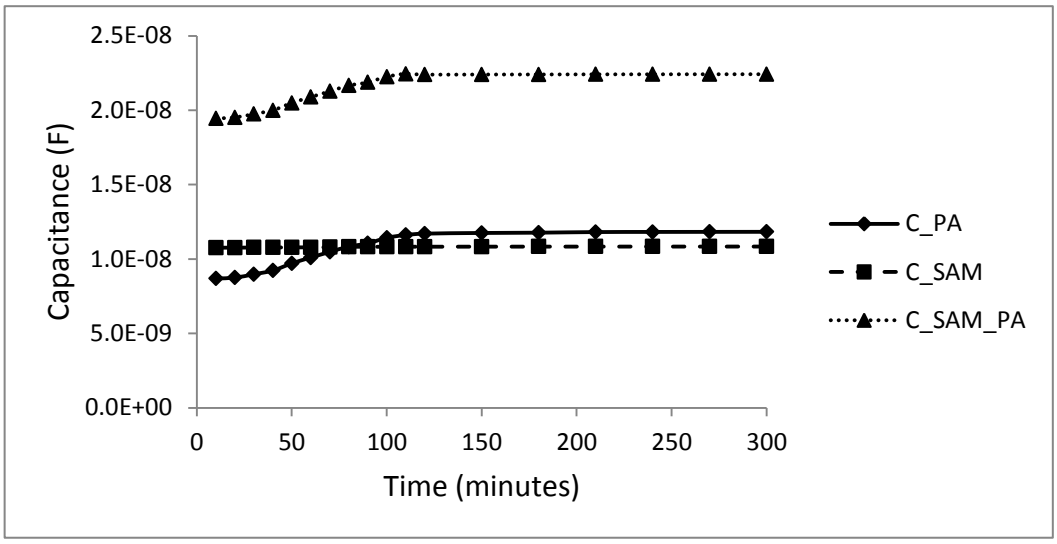

Figure 5.7 The result of capacitance change with time. The x axis is the value of capacitance C_t in equivalent circuit (figure 5.3). C_PA represents the capacitance C_t of immobilising Protein A directly on the surface of electrodes. C_SAM represents the capacitance C_t of the SAM layer on the surface of electrodes. C_SAM_PA represents the capacitance C_t that coating a SAM layer first then immobilising Protein A molecules on SAM.

The next experiment in this section was conducted to verify whether the immobilisation of Protein A molecules on the surface of the electrodes is a stable state. Before each measurement, the inside of the ring on the sensing surface was cleaned completely, and the cleaning processes were the same as above mentioned. A 2μl Protein A solution (Invitrogen, 10-1011) with concentration 25mg/ml was arranged in the cell, then the cell was filled with the redox couple solution. After 120 minutes, the cell was rinsed with buffer solution to remove the unfirmly immobilized molecules of Protein A. After that, the cell was filled with the redox couple solution again and impedance was monitored. These experimental processes were repeated 5 times. Next, a SAM layer was formed on the surface of the electrodes in the same device. Then a 2μl protein A solution (concentration 25mg/ml) was arranged into the cell, and the cell was also filled with the redox couple solution. After 120 minutes, the cell was rinsed with buffer solution to remove unbound Protein A molecules on the surface of the electrodes. Next, the cell was filled with the redox couple solution again and the impedance was measured. These

experimental processes were also repeated 5 times. The recorded impedance data were transferred to the capacitance value and the experimental result is displayed in figure 5.8.

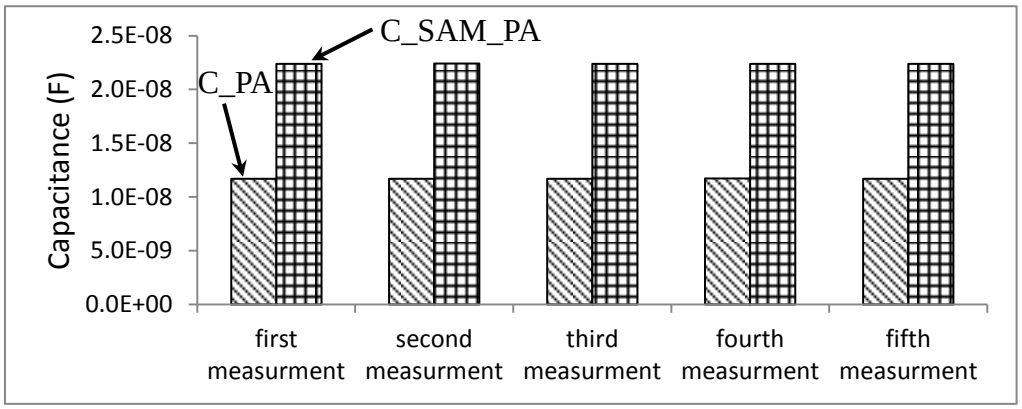

Figure 5.8 The result of measuring capacitance C_t of the Protein A solution with a concentration 15mg/ml. C_PA represents the capacitance C_t of immobilising Protein A directly on the surface of electrodes. C_SAM_PA represents the capacitance C_t that coating a SAM layer first then immobilising Protein A molecules on SAM. It can be found that the variations among these 5 measurements are less than 5%. This experiment interprets that the duration of 120 minutes is enough to let Protein A molecules immobilise firmly on the surface of the electrodes, and the binding is insoluble by washing.

In the next experiment, the relationship between capacitance C_{test} and concentration of Protein A solution was investigated. Before each measurement, the inside of the ring on the sensing surface was cleaned completely, and the cleaning processes were the same as above mentioned. The concentrations of Protein A solution used in this experiment were 0.01mg/ml, 0.1mg/ml, 1mg/ml, 10mg/ml, 20mg/ml, and 25mg/ml, respectively. The processes of measurement were according to the above descriptions and the results are displayed in figure 5.9.

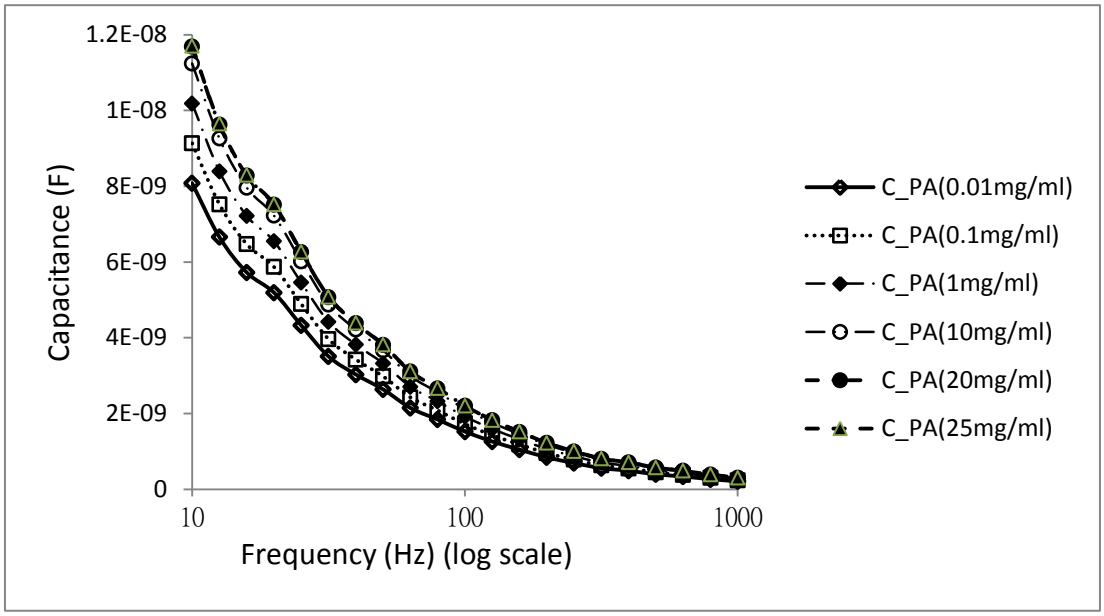

Figure 5.9 The result of measuring capacitance of different concentrations of Protein A solution with a frequency range from 10 Hz to 1000 Hz.

From figure 5.9, it can be found that no matter what concentration of Protein A solution used in the experiment, the capacitance C_{test} fall with the increase of the measuring frequency. In addition, I was interested in the values of capacitance that were measured in the low frequency range (below 100 Hz). In the low frequency range, the differences of capacitance among the different concentrations of Protein A solution are larger than those in the high frequency range. In particular, the data at frequency 10 Hz was focused where it was clear that the capacitance of Protein A solution obtained with high concentrations (10mg/ml, 20mg/ml, or 25mg/ml) was larger than that obtained with low concentrations (0.01mg/ml, 0.1mg/ml, or 1mg/ml). However, the differences among these three high concentrations were not significant. Thus, I focused on measuring the capacitance C_{test} at 10 Hz, and measured a wider range of different concentration Protein A solutions (0.008mg/ml, 0.009mg/ml, 0.05mg/ml, 0.5mg/ml, 5mg/ml, 12mg/ml, 13mg/ml, and 14mg/ml, respectively). The data corresponding to these results is displayed in figure 5.10.

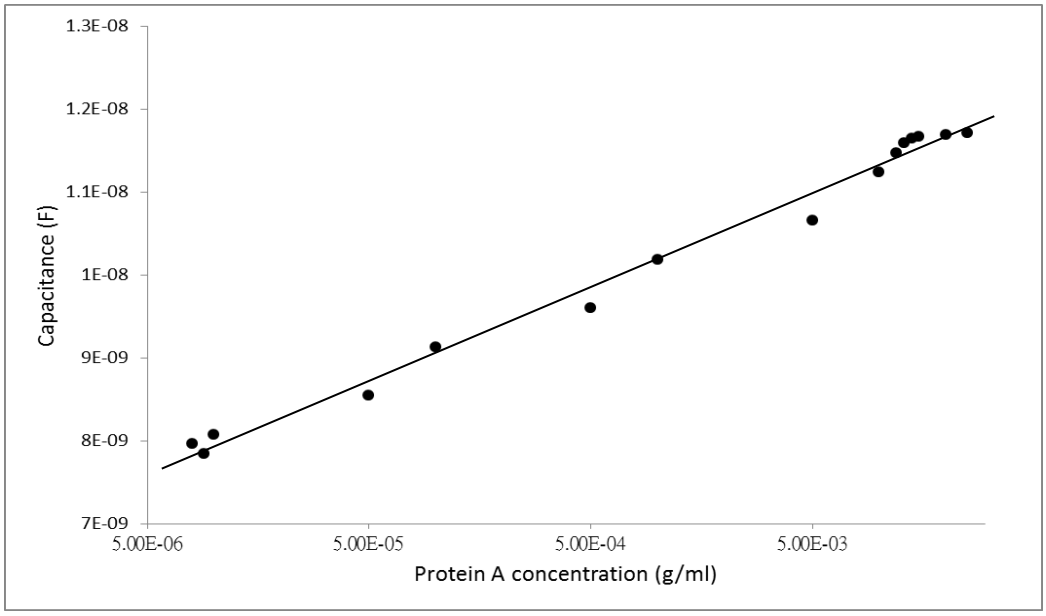

Figure 5.10 The relationship between capacitance C_{test} and Protein A concentration on the impedance sensor without a SAM layer. The x-axis is Protein A concentration expressed in log scale. The y-axis is the value of capacitance C_{test}.

From figure 5.10, the value of capacitance C_{test} increases with the increase of Protein A concentration in the range between 0.01mg/ml and 14mg/ml. When the concentration of Protein A is lower than 0.01mg/ml, variations in capacitance seems to be insensitive to the concentration of Protein A solution. As a result, the limit of detection (LOD) of this sensor can be considered as 0.01mg/ml. When the concentration of Protein A is higher than 14mg/ml, higher Protein A concentration can only cause slightly increase of capacitance. The reason is that at this concentration, the surface of the electrodes is almost saturated by the Protein A molecules, and more Protein A molecules cannot be immobilized on the sensor and so change the value of capacitance C_{test}. This result is similar to the Love wave experimental result in section 4.1, so the saturation concentration of Protein A in this system is 14mg/ml. In the range between 0.01mg/ml and 14mg/ml, the sensitivity of the impedance sensor can be calculated as 118nF·ml/mg.

I was also interested in the sensitivity and LOD of the sensor with SAM layer on it, so the following experiment was conducted. The sensing area was cleaned completely before each measurement. The concentrations of Protein A solution used in this experiment were

0.8ng/ml, 0.9ng/ml, 1ng/ml, 10ng/ml, 100ng/ml, 1μg/ml, 0.01mg/ml, 0.1mg/ml, 1mg/ml, 10mg/ml, 12mg/ml, 13mg/ml, 14mg/ml, 15mg/ml, 20mg/ml, and 25mg/ml, respectively. The processes of measurement were according to the above descriptions. The results of the experiments are displayed in the figure 5.11.

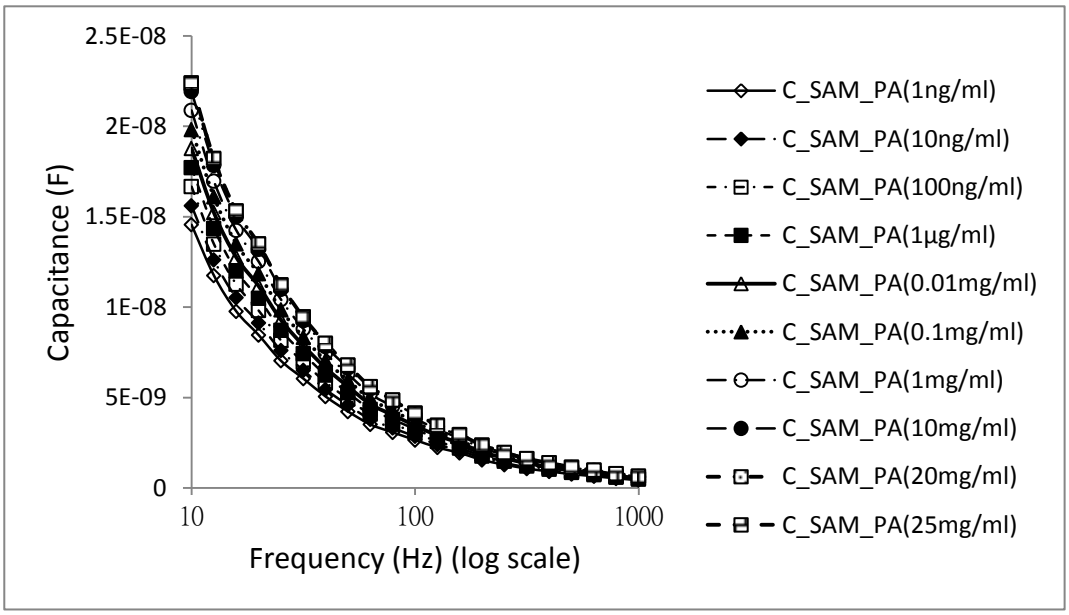

Figure 5.11 The result of measuring capacitance of different concentrations of Protein A solution on the impedance sensor with a SAM layer.

The trends of curves in figure 5.11 is similar to the result in figure 5.9. The data of measuring frequency at 10 Hz was focused and the relationship between capacitance C_{test} and concentration of Protein A was transferred as figure 5.12. From figure 5.12, it can be found that higher concentration of Protein A solution causes the higher value of capacitance C_{test} in the concentration range between 1ng/ml and 14mg/ml. When the concentration of Protein A is lower than 1ng/ml, again it seems to be insensitive to the change in capacitance. Therefore, the limit of detection (LOD) of the impedance sensor with a SAM layer could be considered as 1ng/ml; this value of the LOD is lower than that on the sensor without a SAM layer. Furthermore, again, when the concentration of Protein A exceeded 14mg/ml, higher Protein A concentrations led to only a slight increase of capacitance. This was again because Protein A molecules become difficult to immobilise on the sensor when the concentration of Protein A solution exceeded the saturation concentration. It can be known that the saturation concentration of Protein A in this system

is 14mg/ml, and this result is the same with figure 5.10 and the Love wave measurements of section 4.1. In the range between 1ng/ml and 14mg/ml, the sensitivity of this sensor can be calculated as 120nF·ml/mg. The sensitivity of the sensor with a SAM layer is not much different from that of the sensor without a SAM layer, but the detection limit is much lower.

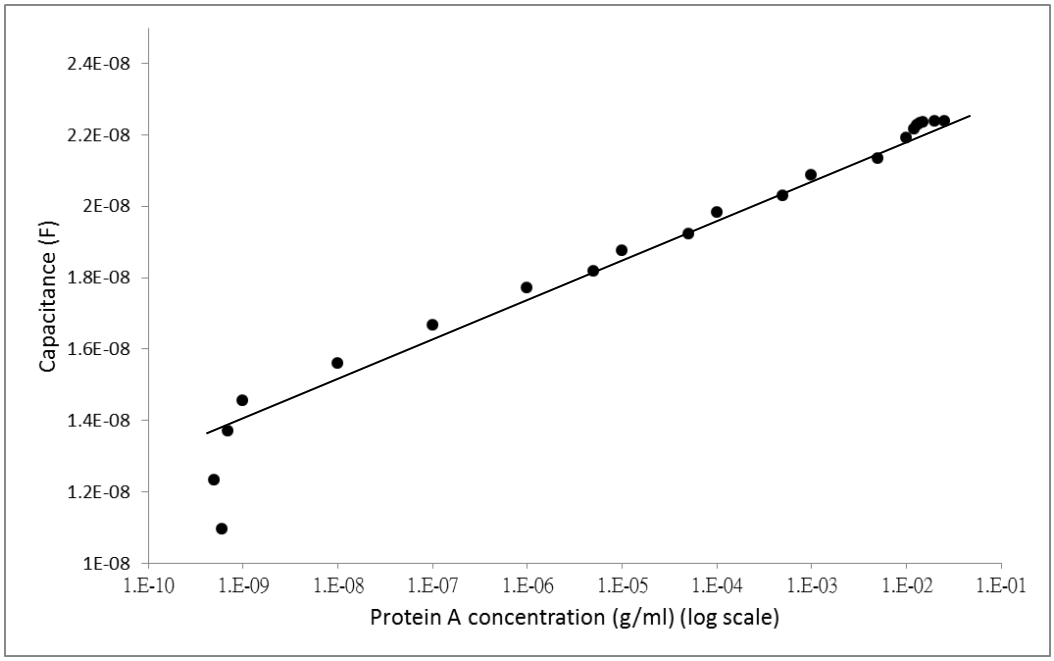

Figure 5.12 The relationship between capacitance C_t and Protein A concentration on the impedance sensor with a SAM layer. The x axis is Protein A concentration expressed in log scale. The y axis is the value of capacitance C_t.

5.4 Comparison of impedance sensor and Love wave sensor measurements

Now the biosensor which combined with two kinds of sensors (Love wave sensor and impedance sensor) was obtained. The Love wave sensor was capable of measuring the mass of the analyte under the dry state on the surface of the sensor based on the calibration data obtained from thin film Ti deposition. The impedance sensor could detect the immobilisation state of the analyte and its capacitance under the liquid state (the changes in capacitance are related to the fraction of the surface that is covered by the adsorbed species). As a third piece of the biosensor characterisation, it was an interesting issue to measure the analyte using Love wave sensor and impedance sensor at the same time under

liquid state. In order to understand what happens with these two measurements at the same time, the following experiment was designed. First, the inside of the cell was cleaned to remove all impurities on the sensing area. Next, the IDTs were connected to the network analyser to measure its central resonance frequency and this frequency was used as the reference frequency. The next step is to place a 2μl Protein A solution with a concentration 0.1mg/ml in the cell, then the cell was filled with the redox couple solution. After 120 minutes, the immobilisation state of Protein A molecules reached a steady state. Then the cell was rinsed by buffer solution to remove the molecules of Protein A that were not firmly immobilised on the sensing area. Then the cell was filled with the redox couple solution again and the electrodes were connected to the impedance analyser to measure its impedance. Following this, the IDTs were connected to the network analyser to measure central resonance frequency under the same conditions. The difference between reference frequency and central resonance frequency was calculated as the value of frequency shift. Next, the device was rinsed with buffer solution and dried by nitrogen stream, then treated in the oxygen Plasma Asher (100Watt, 180 seconds) again to remove all Protein A molecules on the surface of the device. According to the above processes, the experiments were repeated but changed the concentration of Protein A solution. The concentrations of Protein A solution I used were 0.1mg/ml, 0.5mg/ml, 1mg/ml, 5mg/ml, and 10mg/ml, respectively. The result of the experiment is displayed in figure 5.13. In this figure, the x-axis represents Protein A concentration in logarithmic (log) scale. It can be seen that increasing Protein A concentration can cause both capacitance and frequency shift rise for these sensors. Besides that, the relationship between capacitance and Protein A concentration (log scale) approximates linear for impedance sensor. However, the relationship between frequency shift and Protein A concentration (log scale) is a little complex. In the lower concentration range (between 0.1mg/ml and 1 mg/ml), the frequency shift only slightly increases when the Protein A concentration ascends. In contrast, for the higher concentration range (between 1mg/ml and 10mg/ml), the frequency shift increases

significantly with the increase of the Protein A concentration.

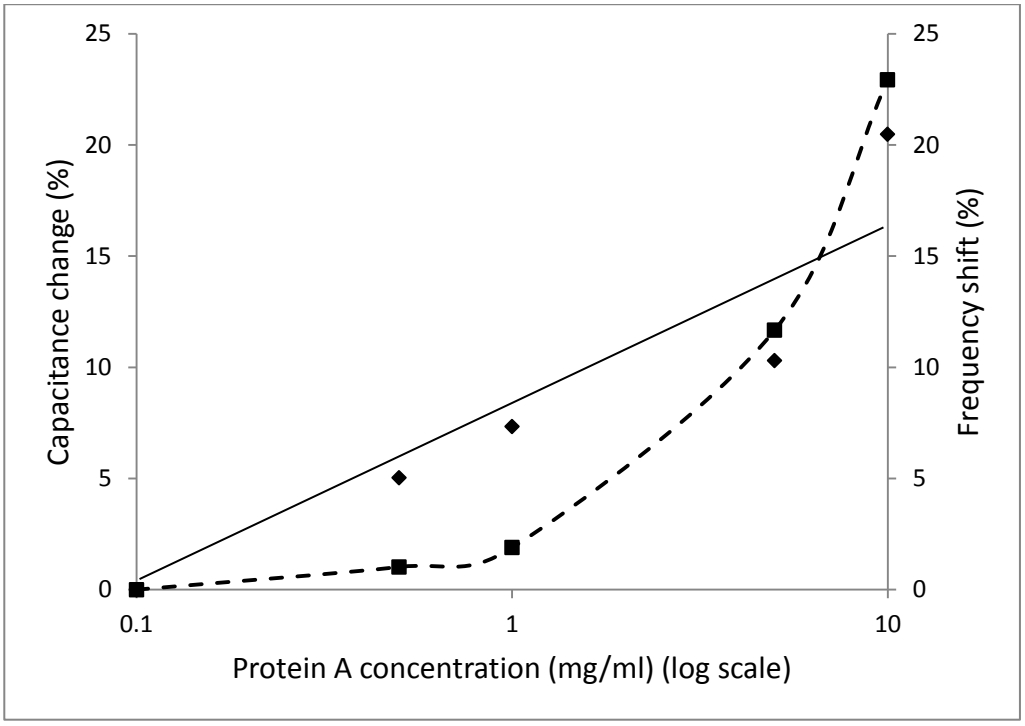

Figure 5.13 The result of measuring different concentrations of Protein A solution by Love wave sensor and impedance sensor at the moment. For Love wave sensor, this figure presents the relationship between frequency shift and Protein A concentration. For impedance sensor, this figure presents the relationship between capacitance and Protein A concentration. The solid line is the trend line of the capacitance change for impedance sensor. The dot line is the trend line of the frequency shift for Love wave sensor.

The following paragraph is the discussion that I tried to find the relation between the frequency shift from Love wave sensor and capacitance change from impedance sensor. First of all, I have known the relation between frequency shift and the mass change on the surface of the Love wave sensor is linear. After I calibrated the sensor, I observed a standard resonance frequency. Next, I immobilised target molecules on the Love wave sensor and measured the resonance frequency of the device. The degree of frequency shift was calculated relative to the standard resonance frequency with no added mass. From figure 3.9, the frequency shift is a function of the mass on the sensing surface as in equation (5.2).

$$\Delta f \propto m \tag{5.2}$$

Where *m* is the mass on the sensing surface. The mass *m* is equal to the density of the immobilised molecules multiplied by the volume of the immobilised layer. The volume of the immobilised layer is equal to the thickness of the immobilised layer multiplied by the area of the immobilised layer. Because the cell in this study is a round, the area can be expressed as the square of the radius of the cell multiplied by pi. The relation of the above description can be expressed in the following equation (5.3).

$$m = \rho_{molec} V_{layer} = \rho_{molec} d_{layer} A = \rho_{molec} d_{layer} r_{cell}^2 \pi \quad (5.3)$$

Where ρ_{molec} is the density of the immobilised molecules. V_{layer} is the volume of the immobilised layer. d_{layer} is the thickness of the immobilised layer. *A* is the area of the immobilised layer, and r_{cell} is the radius of the cell. Then I transfer the equation (5.2) and (5.3) to a logarithm. The result can be expressed in the following equation (5.4).

$$\log(m) = k' + 2\log(r_{cell}) \quad (5.4)$$

$$\log(\Delta f) = k' + 2\log(r_{cell})$$

Where *k'* means the coefficient that is transferred from the density of the immobilised molecules, the thickness of the immobilised layer, and π. There will be a linear relation between frequency (log scale) and the radius of the cell. In addition, I consider the factors that will influence the value of capacitance. It is known that the value of capacitance can be expressed as the following equation:

$$C = \varepsilon_r \frac{\mathrm{A}}{4\pi d_{layer}} \quad (5.5)$$

Where ε_r is the relative permittivity of the immobilised molecules, and A is the effective area between two electrodes. The effective area is related to the coverage ratio of the immobilised molecules on the electrode surface. Here I proposed a hypothesis that the value of capacitance is a function of the coverage ratio in equation (5.6)

$$C = f(c) \quad (5.6)$$

Where *f(c)* is the function of the coverage rate. When I used Love wave sensor to measure Protein A, I obtained that the saturation concentration of Protein A is 14 mg/ml, and it is equal to 14 μg Protein A on the Love wave sensor. I assume that the coverage rate is 100% as 14μg Protein A on the sensing surface. In addition, I also has known the limit of detection (LOD) of the Love wave sensor is 0.022 fg/mm^2, and it can be transferred to the whole LOD of the cell (the area of the cell is about 3.1416mm^2) is 0.069 fg. Consequently, I set the coverage rate is 0% as 0.069 fg Protein A on the sensing surface. Then I transferred the data of frequency shift to the coverage rate, add the coverage rate data with the concentration of Protein A (dotted line) in figure 5.13, and the result is shown as figure 5.14. It can be found that the value of capacitance is proportional to the coverage rate, so the above assumption I made is reasonable. With the higher concentration of Protein A, the coverage rate of immobilised molecules on the sensing surface increase. This is why the higher concentration of Protein A causes the larger value of capacitance. In addition, it can also be explained that the measurement result of Love wave sensor and impedance sensor is correlative.

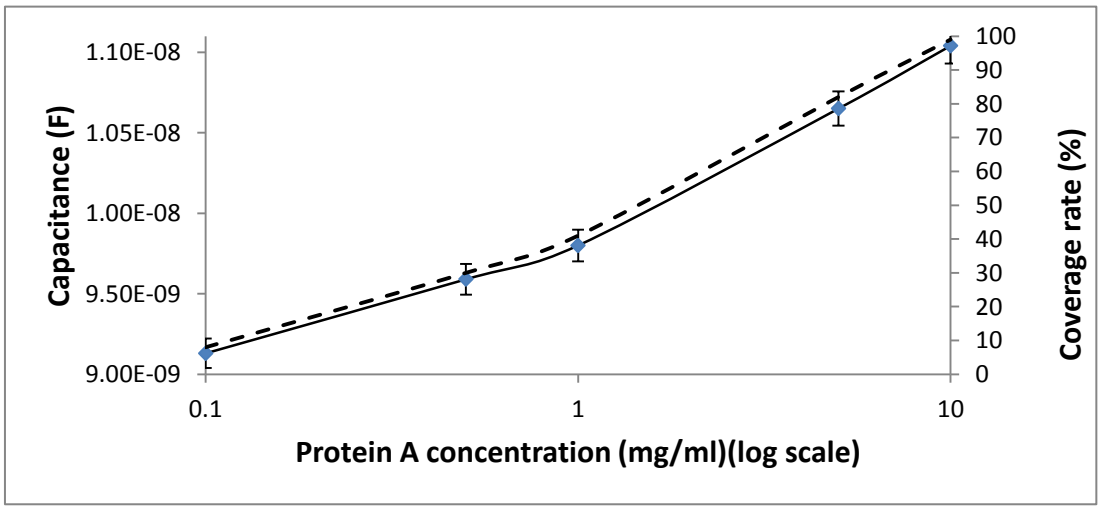

Figure 5.14 The result of measuring different concentrations of Protein A solution and to demonstrate the relationship between capacitance and coverage rate. The coverage rate of immobilised molecules on sensing surface is transferred from frequency shift in figure 5.13.

The next experiment was to investigate whether to arrange an impedance sensor influence the measurement of the Love wave sensor. The experiments of using Love wave sensor to measure different concentrations of Protein A solution were repeated in another Love wave sensor which was also arranged an impedance sensor on it. The Result is displayed in figure 5.15. The LW1_sensor in this figure presents the data from original Love wave sensor, and LW2_sensor in this figure presents the data from another Love wave sensor. In each concentration, the measurements of experiments were repeated 5 times. The error bars in this figure presents the deviations among these measurements. The trends of curves in these two sensors are similar, but the differences on frequency shift between these two sensors are larger than the error deviations in each concentration. This phenomenon can be explained that measurements for each sensor are repeatable, but it is a challenge to be reproducible in another sensor. Because the Love wave sensors are very sensitive to its sensing surface conditions, very small differences on electrodes of the impedance sensor and cell could affect the boundary condition of travelling Love waves and cause changes in the frequency shift. Therefore, if I would like to compare the results from different compound sensors (Love wave sensor and impedance sensor), it is necessary to calibrate these sensors to the same baseline in advance.

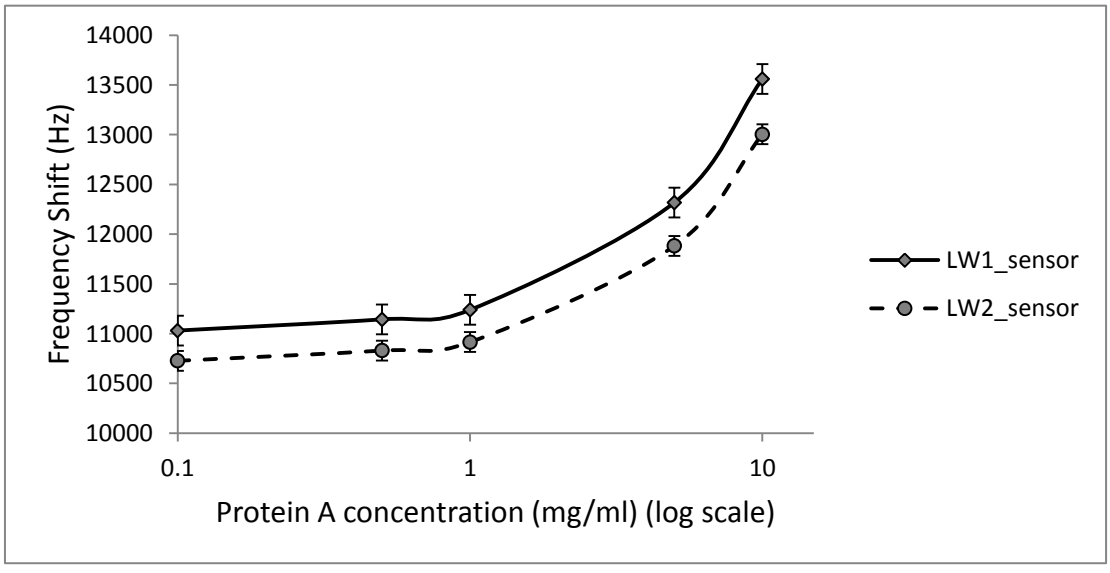

Figure 5.15 The result of measuring different concentrations of Protein A solutions by different Love wave sensors on compound sensors.

The above experiments illustrate a problem in that the linearity of the calibration results from using Love waves to measure analytes under liquid conditions (Figure 5.15) is different to that obtained when the calibration is done using dry samples (Figure 4.2). This might be because the measurement results of Love wave sensors are related to the boundary conditions of sensing surface and the degree to which the molecules are on the sensing surface may vary depending on the liquid conditions surrounding the analyte molecules and the overall amount of analyte that is adsorbed. When the concentration of analyte is low, the molecules may be loosely packed on the surface and so be well solvated by the liquid, resulting in them being weakly bound to the surface. Therefore, this non-rigidity associated with the binding causes the frequency to shift only slightly when small amounts of material are adsorbed (low overall surface coverage). In contrast, when the concentration of analyte is high, the possibility of molecules binding on the surface increases substantially and they may be closely packed together. This compact nature of the adsorbed layer leads to a change of frequency shift that is more significant. In addition, the ideal condition for measurements using a Love wave sensor is that the binding state of molecules is a static state. However, in practical situations, in solution, the process of molecules binding is dynamic. In the beginning, molecules are distributed randomly and uniformly in the liquid. Then, some molecules are immobilised on the surface and the concentration becomes lower in the region near the surface. Other molecules will move from a region of high concentration to a region of low concentration, so that the viscosity of the liquid changes and affects the boundary condition of the sensing surface. Some molecules that are weakly bound with the surface are probable to solve into the liquid and depart from the surface. All these processes are dynamic and result in the uncertainty of measurement with using Love wave sensor under the liquid condition. However these effects would probably only affect dynamic/kinetic Love wave measurements, and not the static, steady state Love wave measurements done here. Notably, when using Love wave sensor under the dry state, the measurement results are stable because the molecules are

rigidly bound with the sensing surface. In contrast, the strength of binding of the analyte molecules to the sensor surface may not influence the measurement results of the impedance sensor. This is because the impedance sensor response is mainly influenced by the coverage area of molecules and the thickness of immobilised layer. That is why I integrate Love wave sensor and impedance sensor into the same device, and can use Love wave sensor under dry condition as well as utilise impedance sensor under liquid condition to measure analytes. Note, the measurements of Figure 5.15 indicate that whilst there is an 'offset' in the frequency shift of the two devices (which may be a consequence of the device fabrication), the variation in frequency shift with Protein A concentration is similar. It is anticipated that optimisation of the fabrication, size, placement and connections associated with the electrochemical impedance electrodes will reduce the device-device offsets seen here.

Chapter 6 Conclusion and discussion

6.1 Major finding

In this study, I developed a biosensor based on the piezoelectric biosensing methods. This biosensor consists of a Love wave sensor and an impedance sensor, and both of them are label-free biosensor. When applying the sensor to measure analytes, it does not need to bind labels (radioactive particles, fluorescence particles, magnetic particles, etc.) or use enzyme to generate some special electrochemically active products. In order to maximize the performance of the sensor, I choose 64°Y–X lithium niobate ($LiNbO_3$) which is a kind of piezoelectric materials as the substrate. On the substrate, there is a pair of interdigital transducers (IDTs) which are composed of 100 Ti/Au (thickness are 10/100nm) split-finger pairs with a periodicity (λ) of 40μm. The acoustic path length, between both IDTs, is 200λ and the IDTs aperture is 100λ. Upon the substrate and IDTs, there is a PMMA guiding layer which has an optimised thickness range from 1000 nm to 1300 nm. Through the experiments, I have known that the thickness of PMMA in this range can have the minimum loss for the travelling Love waves. In addition, a gold layer with thickness 100 nm is deposited on the guiding layer as the sensing area. The width of the area is 2mm and its length is 5mm. Besides that, a 100 μm gap is arranged in the middle of the gold layer to separate the sensing area as two electrodes and these two electrodes can be used as impedance sensor. The Love wave sensor is measured with network analyser and using TRL calibration in advance. All connection with the device had been dealt with impedance matching to reduce reflection noise. The central resonant frequency of the Love wave sensor is 116.466 MHz; the insertion loss and phase at this frequency is -15.67dB, and -84.35 degrees, respectively. The mass sensitivity of this Love wave reaches to 2574 $mm^2/\mu g$. In addition, the limit of detection (LOD) is 0.022 fg/mm^2.

The Love wave sensor can be used to measure Protein A, IgG, Anti-GABA, and GABA. In this study, I have verified that no matter what state Protein A was measured in

(dry state or immersed in liquid); the Love wave sensor is capable of providing response of frequency shift. However, comparison with electrochemical impedance measurements performed on the same samples, at the same time, showed that the Love wave response of immobilised Protein A measured in an aqueous solution is complex due to many factors (mass, viscosity, conductivity, etc.) which could affect the frequency shift of the device. Notably, this complex relation between Love wave frequency shift measured in solution, and the mass of immobilised species does not mean that the Love wave device cannot be used as a mass sensor in solution. It just means that it needs to be calibrated and verified (standardised) using an additional measurement technique (i.e. in this case, electrochemical impedance measurements). Here, I used the dry state analyte measurements of the sensing surface to simplify the relation between the frequency shift and the quantities of the analytes and found these had a close to linear correlation with the capacitance measurements, whereas the solution based Love wave measurements did not.

If there are more quantities of the analytes, the mass on sensing are is heavier and that causes more frequency shift. In addition, the saturation concentration of Protein A solution is 14mg/ml. If the concentration of protein A exceeds this value, it is difficult to immobilise more Protein A molecules on the sensing area of the Love wave. Besides that, experiments in this study also provide evidence that measuring IgG on the Love wave sensor by using Protein A to bind with IgG molecules is feasible. The response of frequency shift is linear when measuring IgG during the concentration range from 0.01 mg/ml to 0.1 mg/ml. I use the similar method to measure Anti-GABA and GABA molecules. The saturation concentration of Anti-GABA solution for the Love wave sensor is 7mg/ml. The result of measuring frequency shift of the different concentration of GABA solution (from 0.01 mg/ml to 0.1 mg/ml) represents that with the increase concentration of GABA solution, frequency shift of the sensor rises linearly.

In this study, I also show that it is feasible to add an impedance sensor on the Love

wave sensor. This impedance sensor was calibrated under the specific condition that the cell on the electrodes filled with 5 mM redox couple solution ($K_3Fe(CN)_6/K_4Fe(CN)_6$). After calibration, this impedance sensor can measure the impedance of analyte under liquid state. In addition, the measured impedance can be transferred to the capacitance value C_t which is related to the interaction between analyte and electrodes. This impedance sensor was used to measure two different materials coating on the electrodes. One is a 52nm thickness PMMA layer. The other is a SAM (self-assembled monolayer) which was formed with hexadecyl mercaptan. This sensor can distinguish these two materials by their impedance values from Nyquist impedance plot. I also used the impedance sensor to measure different concentrations Protein A solutions. I discovered that the time of immobilizing Protein A molecules on the sensing area takes 120 minutes to reach a steady state. In addition, the saturation concentration of Protein A on the sensing area is 14mg/ml, and this result is the same as the measurement of the Love wave sensor. Besides that, I also discovered that the sensitivity of the sensitivity of the sensor with a SAM layer is not much different from that of the sensor without a SAM layer. When I used the impedance sensor with a SAM layer to measure Protein A, the sensitivity of the sensor is 120nF·ml/mg. The limit of detection (LOD) of the impedance sensor for measuring Protein A can be improved by applying a SAM layer on the sensing electrodes. The LOD of the impedance sensor with a SAM layer can reach to 10^{-9}g/ml, but the impedance sensor without a SAM layer is only 10^{-5}g/ml.

6.2 Significance of this study

In this study, I developed biosensors which are based on the interdigital transducers structures and piezoelectric materials. The innovative design of our sensors can combine Love wave sensor with impedance sensor in the same device. This device provides two kinds of conditions (dry state and wet state) to measure analytes. This biosensor can not only measure the mass of the analyte that immobilises on the sensing surface, but it also

detects the capacitance of the analyte when in solution. Besides that, I can calculate the sensing surface coverage rate of the analyte after calibration and data transformation. The sensor in this study has advantages of higher sensitivity and the ease of use on the measurement in comparison with recently previous research. The research group of Matatagui reported a Love wave sensor working in dynamic mode in 2013 [207]. The piezoelectric substrate of this sensor is ST-X Quartz and the material of guiding layer is a 3.5μm thick SiO_2. The working frequency of the device is 163 MHz. The sensitivity of this Love wave sensor is about 380mm^2/μg, which is poorer than the sensor in this study (2574 mm^2/μg). Nanofibers could be arranged on the sensing surface and the Love wave devices could be used as gas sensor [74]. They demonstrated that in the dry state there are good linear correlations between the frequency shifts of the sensor and concentrations of the analyte and the limit of detection is about 0.5fg/mm^2, which is larger than the device in this study (0.022fg/mm^2). Another work about using Love wave sensor to investigate the quantitative correlation of the acoustic wave signal with the molecular weight of surface bound proteins has been implemented by Mitsakakis *et al.* in 2014 [75]. A linear relationship was found to exist between the phase change of the acoustic signal and the molecular weight of the proteins in specific binding. The Love wave sensor in this research was based on a quartz piezoelectric substrate and the guiding layer material is a 700nm thick PMMA film. The operation frequency of this device is 155 MHz and a flow-through microfluidic system was employed on the sensing area. The limit of detection in this device is about 0.5fg/mm^2 and this value is worse than that in this study (0.022fg/mm^2). In 2014, Chowdhury *et al.* designed a biosensing platform by covalent attachment of biomolecules on PAni nano-wire (NW) decorated with gold nanoparticles (AuNP) [208]. They prepared a Pt electrode with a diameter of 2 mm on a mirror surface with Al_2O_3 slurry and formed a structure of Pt||Au-PAni/LAA (antibody) on the electrode. The change in total impedance of the sensor electrode on attachment of the target molecule was monitored. They discovered that with attachment of protein molecules, the double layer

capacitance of the conducting surface was increased with simultaneous lowering of impedance, so they mainly observed in lower frequency region and have the same approach in this study. They also observed that when concentration was greater than 10 mM, the response of the electrode was inclined to saturate. The reason is that all the properly oriented antibody molecules are occupied by the detectable proteins. The saturation concentration of Protein A in this study is 14mg/ml and this value is different from the research of Chowdhury. It is possible that different kinds of proteins on distinct electrodes surface may cause the different conditions of saturation. In 2014, Mok *et al.* reported a digital microfluidic assay for protein detection. They designed three electrodes impedance sensor and used a 300 mV AC signal with a frequency 700 kHz to excite the system [209]. The dynamic range of this sensor is greater than six orders of magnitude and that is similar to the impedance sensor with SAM layer in this study. If I compare the limit of detection (LOD) of the sensor in this study with that in this paper, I observe that LOD in this study (24 pM) is lower than that in previous research (50 pM). In conclusion, the sensor in this study has higher sensitivity and lower limit of detection. These two characteristics are very important to application of sensing.

6.3 Future works

There is still a problem to be solved in this study in the future. In chapter 5, I discussed that the baseline drift of frequency shift on Love wave sensor after combining an impedance sensor on the substrate. The precision of fabricating cell and electrodes of the impedance sensor will still have to improve. If the error of the mass on the guiding layer of the Love wave sensor could be ensured in a fixed range, I could develop a more efficient method to calibrate the sensors to reduce the measurement variances. Furthermore, our target is to explicitly present reproducibility data, such as by giving coefficient of variance of multiple experiments (ideally on different days using different sensors). The methodology for determining the response curve should be stated and reproducibility data

presented clearly along with it.

Because the biosensor in this study can be classified as an affinity biosensor, it will also face a general problem of selectivity in the presence of large concentrations of nontarget material. Traditionally, this problem can be overcome by using labels and/or labeled secondary probes. However, both of these solutions are not suitable for the goal of developing a point-of-care detection device because they require extra time, add extra sample preparation steps, and increase overall system complexity. This challenge is common to all label-free affinity sensors. Therefore, I will pay attention to the nonspecific response of the sensors in the future, as well as demonstrate selectivity to the chosen analyte in the presence of large background concentration of nonspecific interferents [188]. A first step towards this goal is reporting the sensor response to a large concentration of nontarget, testing specificity. The next step is to include a small concentration of target in a background of nontarget. In my opinion, these efforts are as important as to investigate the limit of detection of specific targets. Mechanisms by which the affinity interaction changes the mass and impedance on measuring surface are poorly understood. Therefore, the in-situ measurement with continuous data recording should be conducted. There is need for both experimental and theoretical work in this topic in the future. With an understanding of the molecular mechanisms underlying mass and impedance change, the optimal conditions and an optimal measurement method can be chosen rationally. Although there are hundreds of publications about Love wave sensor and impedance sensor, no product based on Love wave and impedance biosensors has can success in widespread commercial market.

To conclude, this study has commenced a new area of research that combine Love wave sensor and impedance sensor in the same device to proceed label-free biosensing. Future research in the area of label-free piezoelectric biosensing methods should aim at applications that take advantages of small size, low power, simplified sample preparation, and moderate multiplexing capability.

Reference

[1] M. Ngoepe, Y. E. Choonara, C. Tyagi, L. K. Tomar, L. C. d. Toit, P. Kumar, *et al.*, "Integration of Biosensors and Drug Delivery Technologies for Early Detection and Chronic Management of Illness," *Sensors*, vol. 13, pp. 7680-7713, 2013.

[2] J. Wang, "Electrochemical Glucose Biosensors," *Chemical reviews*, vol. 108, pp. 814-825, 2008.

[3] Z. Zhu, L. Garcia-Gancedo, A. J. Flewitt, H. Xie, F. Moussy, and W. I. Milne, "A Critical Review of Glucose Biosensors Based on Carbon Nanomaterials: Carbon Nanotubes and Graphene," *Sensors*, vol. 12, pp. 5996-6022, 2012.

[4] L. C. Clark Jr. and C. Lyons, "ELECTRODE SYSTEMS FOR CONTINUOUS MONITORING IN CARDIOVASCULAR SURGERY," *Automated and Semi-Automated Systems in Clinical Chemistry*, vol. 102, pp. 29-45, 1962.

[5] G. G. Guilbault and G. J. Lubrano, "Amperometric enzyme electrodes: Part II. Amino acid oxidase," *Analytica chimica acta*, vol. 69, 1974.

[6] J. Tang and T. S. Kern, "Inflammation in diabetic retinopathy," *Progress in Retinal and Eye Research*, vol. 30, pp. 343-358, 2011.

[7] S. F. Clarke and J. R. Foster, "A history of blood glucose meters and their role in self-monitoring of diabetes mellitus.," *Br J Biomed Sci.*, vol. 69, pp. 83-93, 2012.

[8] P. J. Stout, J. R. Racchini, M. E. Hilgers, and S. E. Noujaim, "Continuous glucose monitoring: key challenges to replacing episodic SMBG," *Diabetes Research and Clinical Practice*, vol. 74, pp. 97-100, 2006.

[9] W. INSULL, "The problem of compliance to cholesterol altering therapy," *Journal of Internal Medicine*, vol. 241, pp. 317-325, 1997.

[10] B. C. Özer, H. Özyörük, S. S. Çelebi, and A. Yıldıza, "Amperometric enzyme electrode for free cholesterol determination prepared with cholesterol oxidase immobilized in poly(vinylferrocenium) film," *Enzyme and Microbial Technology*, vol. 40, pp. 262-265, 2007.

[11] Z. Zhao, W. Lei, X. Zhang, B. Wang, and H. Jiang, "ZnO based amperometric enzyme biosensor," *Sensors*, vol. 10, pp. 1216-1231, 2010.

[12] S. Singh, P. R. Solanki, M. K. Pandey, and B. D. Malhotra, "Covalent immobilization of cholesterol esterase and cholesterol oxidase on polyaniline films for application to cholesterol biosensor," *Analytica Chimica Acta*, vol. 568, pp. 126-132, 2006.

[13] B. G. Stone, T. J. Besse, W. C. Duane, C. D. Evans, and E. G. DeMaster, "Effect of regulating cholesterol biosynthesis on breath isoprene excretion in men," *Lipids*, vol. 28, pp. 705-708, 1993.

[14] B. Leboulanger, R. H. Guy, and M. B. Delgado-Charro, "Reverse iontophoresis for non-invasive transdermal monitoring," *Physiological Measurement*, vol. 25, pp. 35-50, 2004.

[15] A. Sieg, R. H. Guy, and M. B. Delgado-Charro, "Noninvasive and Minimally Invasive Methods for Transdermal Glucose Monitoring," *Diabetes Technology & Therapeutics,* vol. 7, pp. 174-197, 2005.

[16] N. S. Oliver, C. Toumazou, A. E. Cass, and D. G. Johnston, "Glucose sensors: A review of current and emerging technology," *DIABETIC Medicine,* vol. 26, pp. 197-210, 2009.

[17] A. Berna, "Metal Oxide Sensors for Electronic Noses and Their Application to Food Analysis," *Sensors,* vol. 10, pp. 3882-3910, 2010.

[18] D. Ivnitski, I. Abdel-Hamid, P. Atanasov, and E. Wilkins, "Biosensors for detection of pathogenic bacteria," *Biosensors and Bioelectronics,* vol. 14, pp. 599-624, 1999.

[19] S. H. Ou, M. C. Wu, T. C. Chou, and C. C. Liu, "Polyacrylamide gels with electrostatic functional groups for the molecular imprinting of lysozyme," *Analytica Chimica Acta,* vol. 504, pp. 163-166, 2004.

[20] D. R. Thévenot, K. Toth, R. A. Durst, and G. S. Wilsond, "Electrochemical biosensor: Recommended definitions and classification," *Biosensors and Bioelectronics,* vol. 16, pp. 121-131, 2001.

[21] B. Byrne, E. Stackl, N. Gilmartin, and R. O'Kennedy, "Antibody-based sensors: Principles, problems and potential for detection of pathogens and associated toxins," *Sensors,* vol. 9, pp. 4407-4445, 2009.

[22] D. Wei, O. A. Oyarzabal, T. S. Huang, S. Balasubramanian, S. Sista, A. L. Simonian, "Development of a surface plasmon resonance biosensor for the identification of *Campylobacter jejuni*," *Journal of Microbiology Methods,* vol. 69, pp. 78-85, 2007.

[23] B. Barlen, S. D. Mazumdar, O. Lezrich, P. Kämpfer, M. Keugsen, "Detection of Salmonella by surface plasmon resonance," *Sensors,* vol. 7, pp. 2040-2046, 2007.

[24] S. D. Mazumdar, M. Hartmann, P. Kämpfer, M. Keugsen, "Rapid method for detection of *Salmonella* in milk by surface plasmon resonance," *Biosensors Bioelectronics,* vol. 22, pp. 1427-1446, 2007.

[25] B. K. Oh, W. Lee, B. S. Chun, Y. M. Bae, W. H. Lee, J. W. Choi, "The fabrication of protein chip based on surface plasmon resonance for detection of pathogens," *Biosensors Bioelectronics,* vol. 20, pp. 1847-1850, 2005.

[26] R. Kumaran and D. Bengt, "Principles and applications of thermal biosensors," *Biosensors Bioelectronics,* vol. 16, pp. 417-423, 2001.

[27] P. Gemeiner, V. Stefuca, A. Welwardova, E. Michalkova, L. Welward, L. Kurillova, "Direct determination of the cephalosporin transforming activity of immobilized cells with use of an enzyme thermistor," *Enzymol. Microb. Technology,* vol. 15, pp. 50-56, 1993.

[28] S. Birnbaum, L. Bülow, K. Hardy, B. Danielsson, K. Mosbach, "Rapid automated analysis of human proinsulin produced by *Escherichia coli*," *Analytical Biochemistry,* vol. 158, pp. 12-19, 1986.

[29] N. J. Ronkainen, H. B. Halsall, and W. R. Heineman, "Electrochemical biosensors,"

Chemical Society Reviews, vol. 39, pp. 1747-1763, 2010.

[30] M. Mecklenburg, C. Lindbladh, H. Li, K. Mosbach, B. Danielsson, "Enzymatic amplification of a flow-injected thermometric enzyme-linked immunoassay for human insulin," *Analytical Biochemistry,* vol. 212, pp. 388-393, 1993.

[31] B. Danielsson, P-O. Larsson, "Specific monitoring of chromatographic procedures," *Trends in Analytical Chemistry,* vol. 9, pp. 223-227, 1990.

[32] D. T. Hoa, T. N. Suresh Kumar, N. S. Pnuekar, R. S. Srinivasa, R. Lal, A. Q. Contractor, "A biosensor based on conducting polymers," *Analytical chemistry,* vol. 64, pp. 2645-2646, 1992.

[33] N. Bojorge Ramírez, A. M. Salgado, and B. Valdman, "A conductimetric biosensor for biosecurity," *Biosensors Bioelectronics ,* vol. 18, pp. 813-819, 2003.

[34] F. Vollmer and S. Arnold, "Whispering-gallery-mode biosensing: Label-free detection down to single molecules," *Nature Methods,* vol. 7, pp. 591-596, 2008.

[35] N. Backmann, C. Zahnd, F. Huber, A. Bietsch, A. Plückthun, H.-P. Lang, *et al.,* "A label free immunosensor array using single-chain antibody fragments," *Proceedings of the National Academy of Sciences of the United States of America,* vol. 102, pp. 14587-14592, 2005.

[36] Y. Wu, C. Gupta, and M. A. Shannon, "Effect of solution concentration, surface bias and protonation on the dynamic response of amplitude-modulated atomic force microscopy in water," *Langmuir,* vol. 24, pp. 10817-10824, 2008.

[37] M. Hnaiein, W. M. Hassen, A. Abdelghani, C. Fournier-Wirth, J. Coste, F. Bessueille, D. Leonard, N. Jaffrezic-Renault, "A conductometric immunosensor based on functionalised magnetite nanoparticles for *E. coli* detection," *Electrochemistry Communications,*vol. 10, pp. 1152-1154, 2008.

[38] M. Alvarez and L. M. Lechuga, "Microcantilever-based platforms as biosensing tools," *Analyst,* vol. 135, pp. 827-836, 2010.

[39] D. Ivnitski, I. Abdel-Hamid, P. Atanasov, E. Wilkins, S. Striker, "Application of electrochemical biosensors for detection of food pathogenic bacteria," *Electroanalysis,* vol. 12, pp. 317-325, 2000.

[40] S. Ripp, P. Jegier, C. Johnson, S. Moser, S. Islam, and G. Sayler, "Bioluminescent bioreporter assays for targeted detection of chemical and biological agents," *Proceedings SPIE,* vol. 6945, pp. 1-6, 2008.

[41] S. M. Radke and E. C. Alocilja, " A high density microelectrode array biosensor for detection of *E. coli* O157:H7," *Biosensors Bioelectronics,* vol. 20, pp. 1662-1667, 2005.

[42] E. Tully, S. P. Higson, R. O'Kennedy, " The development of a 'labeless' immunosensor for the detection of Listeria monocytogenes cell surface protein, *Internalin B,*" *Biosensors Bioelectronics,* vol. 23, pp. 906-912, 2008.

[43] K. Länge, B. E. Rapp, M. Rapp, "Surface acoustic wave biosensors: a review," *Analytical Bioanalytical Chemistry,* vol. 391, pp. 1509-1519, 2008.

[44] M. Rocha-Gaso, C. March-Iborra, Á. Montoya-Baides, A. Arnau-Vives, "Surface

Generated Acoustic Wave Biosensors for the Detection of Pathogens: A Review," *Sensors,* vol. 9, pp. 5740-5769, 2009.

[45] J. W. Grate, G. C. Frye, *Acoustic wave sensors*, Weinheim, 1996.

[46] J. Du, G. L. Harding, J. A. Ogilvy, P. R. Dencher, M. Lake, " A study of Love-wave acoustic sensors," *Sensors and Actuators A: Physical,* vol. 56, pp. 211-219, 1996.

[47] W. Shih, M. Yang, and M. Li, "Development of disposable lipid biosensor for the determination of total cholesterol," *Biosensors and Bioelectronics,* vol. 24, pp. 1679-1684, 2009.

[48] S. Jiang, M. K. Gnanasammandhan, and Y. Zhang, "Optical imaging-guided cancer therapy with fluorescent nanoparticles," *Journal Royal Society Interface,* vol. 7, pp. 3-18, 2010.

[49] D. Theodorescu, S. Wittke, M. M. Ross, M. Walden, M. Conaway, I. Just, *et al.*, "Discovery and validation of new protein biomarkers for urothelial cancer: A prospective analysis," *Lancet Oncology,* vol. 7, pp. 230-240, 2006.

[50] B. Drafts, "Acoustic Wave Technology Sensors," *IEEE TRANSACTIONS ON MICROWAVE THEORY AND TECHNIQUES,* vol. 49, pp. 795-802, 2001.

[51] M. I. R. Gaso, Y. Jiménez, L. A. Francis, and A. Arnau, *Love Wave Biosensors: A Review*: Intech, 2013.

[52] G. Kovacs, G. W. Lubking, M. J. Vellekoop, and A. Venema, "Love waves for (bio)chemical sensing in liquids," in *Ultrasonics Symposium, Proceedings., IEEE*, Tucson, USA, 1992.

[53] E. Gizeli, N. J. Goddard, and C. R. Lowe, "A Love plate biosensor utilising a polymer layer," *Sensors and Actuators B: Chemical,* vol. 6, pp. 131-137, 1992.

[54] G. L. Harding, J. Du, P. R. Dencher, D. Barnett, and E. Howe, "Love wave acoustic immunosensor operation in liquid," *Sensors and Actuators A: Physical,* vol. 61, pp. 279-286, 1997.

[55] J. Freudenberg, S. Schelle, K. Beck, M. von Schickfus, and S. Hunklinger, "A contactless surface acoustic wave biosensor," *Biosensors and Bioelectronics,* vol. 14, pp. 423-425, 1999.

[56] E. Howe and G. Harding, "A comparison of protocols for the optimisation of detection of bacteria using a surface acoustic wave (SAW) biosensor," *Biosensors and Bioelectronics,* vol. 15, pp. 641-649, 2000.

[57] O. Tamarin, S. Comeau, C. Déjous, D. Moynet, D. Rebière, J. Bezian, *et al.*, "Real time device for biosensing: design of a bacteriophage model using love acoustic wave," *Biosensors and Bioelectronics,* vol. 18, pp. 755-763, 2003.

[58] K. Kalantar-Zadeh, W. Wlodarski, Y. Y. Chen, B. N. Fry, and K. Galatsis, "Novel Love mode surface acoustic wave based immunosensors," *Sensors and Actuators B: Chemical,* vol. 91, pp. 143-147, 2003.

[59] M. D. Schlensog, T. M. A. Gronewold, M. Tewes, M. Famulok, and E. Quandt, "A Love-wave biosensor using nucleic acids as ligands," *Sensors and Actuators B: Chemical,* vol. 101, pp. 308-315, 2004.

[60] D. W. Branch and S. M. Brozik, "Low-level detection of a Bacillus anthracis simulant using Love-wave biosensors on 36° YX $LiTaO_3$," *Biosensors and Bioelectronics,* vol. 19, pp. 849-859, 2004.

[61] N. Moll, E. Pascal, D. H. Dinh, J.-P. Pillot, B. Bennetau, D. Rebiere, *et al.*, "A Love wave immunosensor for whole E. coli bacteria detection using an innovative two-step immobilisation approach," *Biosensors and Bioelectronics,* vol. 22, pp. 2145-2150, 2007.

[62] N. Moll, E. Pascal, D. H. Dinh, J.-L. Lachaud, L. Vellutini, J.-P. Pillot, *et al.*, "Multipurpose Love acoustic wave immunosensor for bacteria, virus or proteins detection," *IRBM,* vol. 29, pp. 155-161, 2008.

[63] J. Andrä, A. Böhling, T. M. A. Gronewold, U. Schlecht, M. Perpeet, and T. Gutsmann, "Surface acoustic wave biosensor as a tool to study the interactions of antimicrobial peptides with phospholipid and lipopolysaccharide model membranes," *Langmuir,* vol. 24, pp. 9148-9153, 2008.

[64] M. Bisoffi, B. Hjelle, D. C. Brown, D. W. Branch, T. L. Edwards, S. M. Brozik, *et al.*, "Detection of viral bioagents using a shear horizontal surface acoustic wave biosensor," *Biosensors and Bioelectronics,* vol. 23, pp. 1397-1403, 2008.

[65] L. El Fissi, J.-M. Friedt, V. Luzet, F. Chérioux, G. Martin, and S. Ballandras, "A Love-wave sensor for direct detection of biofunctionalized nanoparticles," presented at the Frequency Control Symposium, 2009 Joint with the 22nd European Frequency and Time forum. IEEE International, Besancon, 2009.

[66] O. Tigli, L. Binova, P. Berg, and M. Zaghloul, "Fabrication and characterization of a Surface-Acoustic-Wave biosensor in CMOS Technology for cancer biomarker detection," *Biomedical Circuits and Systems, IEEE Transactions on,* vol. 4, pp. 62-73, 2010.

[67] F. Fournel, E. Baco, M. Mamani-Matsuda, M. Degueil, B. Bennetau, D. Moynet, *et al.*, "Love wave biosensor for real-time detection of okadaic acid as DSP phycotoxin," in *Proceedings, Eurosensors XXIV,* Linz, Austria, 2010.

[68] I. Gammoudi, H. Tarbague, J. L. Lachaud, S. Destor, A. Othmane, D. Moyenet, *et al.*, "Love Wave Bacterial Biosensors and Microfluidic Network for Detection of Heavy Metal Toxicity," *Sensor Letters,* vol. 9, pp. 816-819, 2011.

[69] T. Song, S. Y. Song, H. C. Yoon, and K. Lee, "Development of a wireless Love wave biosensor platform for multi-functional detection," *Japanese Journal of Applied Physics,* vol. 50, pp. 1-6, 2011.

[70] F. Kardous, L. El Fissi, J.-M. Friedt, F. Bastien, W. Boireau, R. Yahiaoui, *et al.*, "Integrated active mixing and biosensing using low frequency vibration mixer and Love-wave sensor for real time detection of antibody binding event," *Journal of Applied Physics,* vol. 109, pp. 1-8, 2011.

[71] K. Saha, F. Bender, A. Rasmusson, and E. Gizeli, "Probing the viscoelasticity and mass of a surface-bound protein layer with an Acoustic Waveguide Device," *Langmuir,* vol. 19, pp. 1304-1311, 2003.

[72] G. Papadakis, A. Tsortos, and E. Gizeli, "Triple-helix DNA structural studies using a Love wave acoustic biosensor," *Biosensors and Bioelectronics*, vol. 25, pp. 702-707, 2009.

[73] E. Gizeli, C. R. Lowe, M. Liley, and H. Vogel, "Detection of supported lipid layers with the acoustic Love waveguidedevice: application to biosensors," *Sensors and Actuators B: Chemical,* vol. 34, pp. 295-300, 1996.

[74] D. Matatagui, M. J. Fernández, J. Fontecha, I. Sayago, I. Gràcia, C. Cané, *et al.*, "CharacterizationofanarrayofLove-wavegassensorsdevelopedusing electrospinningtechniquetodepositnanofibers assensitivelayers," *Talanta,* vol. 120, pp. 408-412, 2013.

[75] K. Mitsakakis, A. Tsortos, and E. Gizeli, "Quantitative determination of protein molecular weight with an acoustic sensor; significance of specific versus non-specific binding," *Analyst,* vol. 139, pp. 3918-3925, 2014.

[76] T. M. Gronewold, "Surface acoustic wave sensors in the bioanalytical field: recent trends and challenges," *Analytica Chimica Acta,* vol. 603, pp. 119-128, 2007.

[77] J. Tichý, J. Erhart, E. Kittinger, and J. Přívratská, *Fundamentals of Piezoelectric Sensorics*. London: Springer, 2010.

[78] D. Morgan, *Acoustic waves in elastic solids*: Academic Press, 2007.

[79] D. Morgan, *Surface Acoustic Wave Filters With Applications to Electronic Communications and Signal Processing*. London: Academic Press, 2007.

[80] A. E. H. Love, *Some Problems of Geodynamics*: Cambridge University Press; Dover, 1911; 1967.

[81] D. Royer and E. Dieulesaint, *Elastic Waves in Solids I: Free and Guided Propagation*. London: Springer, 2000.

[82] D. Morgan, *Basic survey*: Academic Press, 2007.

[83] D. Morgan, *Resonators and resonator filters*: Academic Press, 2007.

[84] M. Lewis, "Surface-skimming bulk waves, SSBW," presented at the IEEE Ultrasonics Symposium, Phoenix, USA, 1977.

[85] K.-Y. Hashimoto, *Surface Acoustic Wave Devices in Telecommunications: Modelling and Simulation*. Tokyo: Springer, 2000.

[86] K.-Y. Hashimoto and M. Yamaguchi, "Excitation and propagation of shear-horizontal-type surface and bulk acoustic waves," *IEEE Transactions on Ultrasonics, Ferroelectrics and Frequency Control,* vol. 48, pp. 1181-1188, 2001.

[87] B. A. Auld and J. J. Gagnepain, "Horizontal shear surface waves on corrugated surfaces," *Electronics Letters* vol. 12, pp. 650-651, 1976.

[88] I. D. Avramov, F. L. Walls, T. E. Parker, and G. K. Montress, "Extremely low thermal noise floor high power oscillators using surface transverse wave devices," *IEEE Transactions on Ultrasonics, Ferroelectrics and Frequency Control,* vol. 43, pp. 20-29, 1996.

[89] K. Yamanouchi and M. Takeuchi, "Applications for piezoelectric leaky surface waves," in *IEEE Ultrasonics Symposium Proceedings*, Honolulu, USA, 1990, pp.

11-19.
[90] B. Q. Li, "Solidification processing of materials in magnetic fields," *The Member Journal of the Minerals, Metals & Materials Society,* vol. 50, 1998.
[91] (2014). *http://www.smm.co.jp/E/business/material/product/lithium/*.
[92] K. K. Wong, *Properties of Lithium Niobate*. London: INSPEC, 2002.
[93] G. Malovichko, V. Grachev, and E. Kokanyan, "Optimization of lithium niobate for advanced applications by variation of extrinsic and intrinsic defect subsystems," *Ferroelectrics,* vol. 258, pp. 131-140, 2001.
[94] R. S. Weis and T. K. Gaylord, "Lithium niobate: Summary of physical properties and crystal structure," *Applied Physics A* vol. 37, pp. 191-203, 1985.
[95] S. C. Abrahams, J. M. Reddy, and J. L. Bernstein, "Ferroelectric lithium niobate. 3. Single crystal X-ray diffraction study at 24℃," *Journal of Physics and Chemistry of Solids,* vol. 27, pp. 997-1012, 1966.
[96] B. K. Vainshtein, *Fundamentals of Crystals: Symmetry, and Methods of structural Crystallography*. Berlin: Springer 1994.
[97] I. S. Board, "IEEE Standard on Piezoelectricity," vol. 176, ed, 1987.
[98] Y. N. Korkishko and V. A. Fedorov, *Ion exchange in single crystal for integrated optics and optoelectronics*. Cambridge: Cambridge International Science Publishing, 1999.
[99] D. Morgan, *Electrical excitation at a plane surface*: Academic Press, 2007.
[100] K. A. Ingebrigtsen, "Surface Waves in Piezoelectrics," *Journal of Applied Physics,* vol. 40, pp. 2681-2686, 1969.
[101] C. A. A. J. Greebe, P. A. van Dalen, T. J. B. Swanenburg, and J. Wolter, "Electric coupling properties of acoustic and electric surface waves," *Physics Reports,* vol. 1, pp. 235-268, 1971.
[102] R. F. MILSOM, N. H. C. REILLY, and M. REDWOOD, "Analysis of generation and detection of surface and bulk acoustic waves by interdigital transducers," *IEEE TRANSACTIONS ON SONICS AND ULTRASONICS,* vol. SU-24, pp. 147-166, 1977.
[103] K. M. Lakin, "Perturbation theory for electromagnetic coupling to elastic surface waves on piezoelectric substrates," *Journal of Applied Physics,* vol. 42, pp. 899-906, 1971.
[104] B. A. Auld and G. S. Kino, "Normal mode theory for acoustic waves and its application to the interdigital transducer," *IEEE Transactions on Electron Devices,* vol. 18, pp. 898-908, 1971.
[105] M. S. Nieuwenhuizen and A. Venema, "Surface acoustic wave chemical sensors," *Sensors Materials,* vol. 5, pp. 261-300, 1989.
[106] R. M. White, "Surface elastic waves," *Proceedings of the IEEE,* vol. 58, pp. 1238-1276, 1970.
[107] D. S. Ballantine, *Fundamentals of Acoustic Waves*: ACADEMIC PRESS, 2007.
[108] (2014). *http://en.wikipedia.org/wiki/RCA_clean*.

[109] W. Kern, *Handbook of Semiconductor Wafer Cleaning Technology*. Park Ridge, New Jersey, USA: Noyes Publications, 1993.

[110] Z. Hu, A. Glidle, C. N. Ironside, M. Sorel, M. Strain, J. M. Cooper, *et al.*, "Integrated microfluidic spectroscopic sensor using arrayed waveguide grating," in *International Symposium on Photoelectronic Detection and Imaging 2013: Micro/Nano Optical Imaging Technologies and Applications*, Beijing, China, 2013.

[111] M. Hatzakis, B. J. Canavello, and J. M. Shaw, "Single-Step Optical Lift-Off Process," *IBM Journal of Research and Development,* vol. 24, pp. 452-460, 1980.

[112] R. Redd, M. A. Spak, J. P. Sagan, O. P. Lehar, and R. R. Dammel, "Lithographic process for high-resolution metal lift-off," in *Advances in Resist Technology and Processing XVI*, Santa Clara, United State, 1999, p. 1341.

[113] M.-I. Rocha-Gaso, C. March-Iborra, Á. Montoya-Baides, and A. Arnau-Vives, "Surface Generated Acoustic Wave Biosensors for the Detection of Pathogens: A Review," *Sensors,* vol. 9, pp. 5740-5769, 2009.

[114] J. W. Grate , S. J. Martin, and R. M. White, "Acoustic wave microsensors," *Analytical Chemistry,* vol. 65, pp. 940-948, 1993.

[115] J. Weber, M. Link, R. Primig, D. Pitzer, W. Wersing, and M. Schreiter, "Investigation of the scaling rules determining the performance of film bulk acoustic resonators operating as mass sensors," *IEEE Trans Ultrason Ferroelectr Freq Control,* vol. 54, pp. 405-412, 2007.

[116] B. Zimmermann, R. Luckluma, P. Hauptmanna, J. Rabeb, and S. Büttgenbachb, "Electrical characterisation of high-frequency thickness-shear-mode resonators by impedance analysis," *Sensors and Actuators B: Chemical,* vol. 76, pp. 47-57, 2001.

[117] A. D. Helfrick, *Electrical spectrum and network analyzers : a practical approach*. London: Academic Press, 1991.

[118] (2014). *http://cp.literature.agilent.com/litweb/pdf/5965-7917E.pdf*. Available: http://cp.literature.agilent.com/litweb/pdf/5965-7917E.pdf

[119] "http://www.coursehero.com/file/5701742/networkanalyzer/," 2014.

[120] G. F. Engen and C. A. Hoer, "Thru-Reflect-Line: An Improved Technique for Calibrating the Dual Six-Port Automatic Network Analyzer," *IEEE Trans. Microwave Theory and Techniques,* vol. MTT-22, pp. 48-52, 1974.

[121] D. M. Pozar, *Microwave Engineering*. Hoboken, N.J.: John Wiley & Sons, 2005.

[122] L. A. Francis, "Thin film acoustic waveguides and resonators for gravimetric sensing applications in liquid," PhD Thesis, Université Catholique de Louvain, 2006.

[123] J. Du, G. L. Harding, J. A. Ogilvy, P. R. Dencher, and M. Lake, "A study of Love-wave acoustic sensors," *Sensors and Actuators A: Physical,* vol. 56, pp. 211-219, 1996.

[124] G. McHale, M. I. Newton, and F. Martin, "Theoretical mass, liquid, and polymer sensitivity of acoustic wave sensors with viscoelastic guiding layers," *Journal of Applied Physics,* vol. 93, pp. 675-690, 2003.

[125] F. Herrmann and S. Büttgenbach, "Temperature-Compensated Shear-Horizontal Surface Acoustic Waves in Layered Quartz/SiO2-Structures," *physica status solidi*, vol. 170, pp. R3-R4, 1998.

[126] E. Gizeli, F. Bender, A. Rasmusson, K. Saha, F. Josse, and R. Cernosek, "Sensitivity of the acoustic waveguide biosensor to protein binding as a function of the waveguide properties," *Biosensors and Bioelectronics*, vol. 18, pp. 1399-1406, 2003.

[127] N. Barié, T. Wessa, M. Bruns, and M. Rapp, "Love waves in SiO2 layers on STW-resonators based on LiTaO3," *Talanta*, vol. 62, pp. 71-79, 2004.

[128] F. Herrmann, M. Weihnacht, and S. Buttgenbach, "Properties of sensors based on shear-horizontal surface acoustic waves in LiTaO3/SiO2 and quartz/SiO2 structures," *IEEE Transactions on Ultrasonics, Ferroelectrics, and Frequency Control*, vol. 48, pp. 268-273, 2001.

[129] K. Kalantar-Zadeh, A. Trinchi, W. Wlodarski, and A. Holland, "A novel Love-mode device based on a ZnO/ST-cut quartz crystal structure for sensing applications," *Sensors and Actuators A: Physical*, vol. 100, pp. 135-143, 2002.

[130] E. Gizeli, A. C. Stevenson, N. J. Goddard, and C. R. Lowe, "A novel Love-plate acoustic sensor utilizing polymer overlayers," *IEEE Trans Ultrason Ferroelectr Freq Control*, vol. 39, pp. 657-659, 1992.

[131] D. A. Powell, K. Kalantar-zadeh, and W. Wlodarski, "Numerical calculation of SAW sensitivity: application to ZnO/LiTaO3 transducers," *Sensors and Actuators A: Physical*, vol. 115, pp. 456-461, 2004.

[132] D. Matatagui, J. Fontecha, M. J. Fernández, M. Aleixandre, I. Gracia, C. Cané, *et al.*, "Array of Love-wave sensors based on quartz/Novolac to detect CWA simulants," *Talanta*, vol. 85, pp. 1442-1447, 2011.

[133] W. F. Mousa, M. Kobayashi, S. Shinzato, M. Kamimura, M. Neo, S. Yoshihara, *et al.*, "Biological and mechanical properties of PMMA-based bioactive bone cements," *Biomaterials*, vol. 21, pp. 2137-2146, 2000.

[134] W. R. Zeng, S. F. Li, and W. K. Chow, "Preliminary Studies on Burning Behavior of Polymethylmethacrylate (PMMA)," *Journal of Fire Sciences*, vol. 20, pp. 297-317, 2002.

[135] M. Ezrin, *Plastics Failure Guide: Cause and Prevention*, 2 ed. Munich: Hanser Verlag, 2013.

[136] R. Q. Frazer, R. T. Byron, P. B. Osborne, and K. P. West, "PMMA: An Essential Material in Medicine and Dentistry," *Journal of Long-Term Effects of Medical Implants*, vol. 15, pp. 629-639, 2005.

[137] R. V. Lapshin, A. P. Alekhin, A. G. Kirilenko, S. L. Odintsov, and V. A. Krotkov, "Vacuum ultraviolet smoothing of nanometer-scale asperities of Poly(methyl methacrylate) surface," *Journal of Surface Investigation. X-ray, Synchrotron and Neutron Techniques*, vol. 4, pp. 1-11, 2010.

[138] E. Gizeli, A. C. Stevenson, N. J. Goddard, and C. R. Lowe, "Acoustic Love plate

sensors: comparison with other acoustic devices utilizing surface SH waves," *Sensors and Acruotors B,* vol. 14, pp. 638-639, 1993.

[139] A. C. Stevenson, E. Gizeli, N. J. Goddard, and C. R. Lowe, "Acoustic Love plate sensors: a theoretical model for the optimization of the surface mass sensitivity," *Sensors and Actuators B: Chemical,* vol. 14, pp. 635-637, 1993.

[140] K. K. Zadeh, A. Trinchi, W. Wlodarski, and A. Holland, "A novel Love-mode device based on a ZnO/ST-cut quartz crystal structure for sensing applications," *Sensors and Actuators A: Physical,* vol. 100, pp. 135-143, 2002.

[141] G. McHale, M. I. Newton, and F. Matin, "Layer guided shear horizontally polarized acoustic plate modes," *Journal of Applied Physics,* vol. 91, p. 5735, 2002.

[142] Z. Wang, J. D. N. Cheeke, and C. K. Jen, "Sensitivity analysis for Love mode acoustic gravimetric sensors," *Applied Physics Letters,* vol. 64, pp. 2940-2942, 1994.

[143] A. A. Oliner, "Microwave network methods for guided elastic waves," *IEEE Transactions on Microwave Theory and Techniques,* vol. 17, pp. 812-826, 1969.

[144] B. A. Auld, *Acoustic fields and waves in solids*: Krieger, 1990.

[145] D. MacDougall and W. B. Crummett, "Guidelines for data acquisition and data quality evaluation in environmental chemistry," *Analytical Chemistry,* vol. 52, pp. 2242-2249, 1980.

[146] J. Du, D. R. Harding, A. F. Collings, and P. R. Dencher, "An experimental study of Love-wave acoustic sensors operating in liquids," *Sensors and Actuators A: Physical,* vol. 60, pp. 54-61, 1997.

[147] B. Jakoby, J. Bastemeijer, and Michael J Vellekoop, "Temperature-compensated Love-wave sensors on quartz substrates," *Sensors and Actuators A: Physical,* vol. 82, pp. 83-88, 2000.

[148] (2013). *http://en.wikipedia.org/wiki/Protein_A*.

[149] M. Graille, E. A. Stura, A. L. Corper, B. J. Sutton, M. J. Taussig, J. B. Charbonnier, *et al.,* "Crystal structure of a Staphylococcus aureus protein A domain complexed with the Fab fragment of a human IgM antibody: structural basis for recognition of B-cell receptors and superantigen activity.," *Proceedings of the National Academy of Sciences of the United States of America,* vol. 97, pp. 5399-5404, 2000.

[150] C. S. Goodyear and G. J. Silverman, "Death by a B cell superantigen: In vivo VH-targeted apoptotic supraclonal B cell deletion by a Staphylococcal Toxin," *The Journal of Experimental Medicine,* vol. 197, pp. 1125-1139, 2003.

[151] (2014). *http://www.bionity.com/en/encyclopedia/Protein_A.html*.

[152] G. Muthukrishnan, G. A. Quinn, R. P. Lamers, C. Diaz, A. L. Cole, S. Chen, *et al.*, "Exoproteome of Staphylococcus aureus reveals putative determinants of nasal carriage," *Journal of Proteome Research,* vol. 10, pp. 2064-2078, 2011.

[153] (2014). *http://en.wikipedia.org/wiki/Immunoglobulin_G*.

[154] (2011). *http://medlibrary.org/medwiki/IgG2*.

[155] J. Stadlmann, M. Pabst, D. Kolarich, R. Kunert, and F. Altmann, "Analysis of

immunoglobulin glycosylation by LC-ESI-MS of glycopeptides and oligosaccharides," *Journal of Proteomics,* vol. 8, pp. 2858-2871, 2008.

[156] L. C. Junqueira and J. Carneiro, *Basic Histology*. Rio de Janeiro: McGraw-Hill, 2003.

[157] D. L. Mallery, W. A. McEwan, S. R. Bidgood, G. J. Towers, C. M. Johnson, and L. C. James, "Antibodies mediate intracellular immunity through tripartite motif-containing 21 (TRIM21)," *Proceedings of the National Academy of Sciences of the United States of America,* vol. 107, pp. 19985-19990, 2010.

[158] (2013). *http://www.medikon.ge/eng/lab/aller/aller3.html*.

[159] A. J. Meulenbroek, *Human IgG subclasses: useful diagnostic markers for immunocompetence : useful diagnostic markers for immunocompetence*. Amsterdam: Sanquin, 2008.

[160] G. Lakos, L. Soós, A. Fekete, Z. Szabó, M. Zeher, I. F. Horváth, *et al.*, "Anti-cyclic citrullinated peptide antibody isotypes in rheumatoid arthritis: association with disease duration, rheumatoid factor production and the presence of shared epitope," *Journal of Clinical and Experimental Rheumatology,* vol. 26, pp. 253-260, 2008.

[161] (2011). *http://medlibrary.org/medwiki/GABA*.

[162] D. Majumdar and S. Guha, "Conformation, electrostatic potential and pharmacophoric pattern of GABA (gamma-aminobutyric acid) and several GABA inhibitors," *Journal of Molecular Structure: THEOCHEM,* vol. 180, pp. 125-140, 1988.

[163] A.-M. Sapse, *Molecular Orbital Calculations for Amino Acids and Peptides*. Boston: Birkhäuser Boston, 1999.

[164] J. R. Cooper, F. E. Bloom, and R. H. Roth, *The Biochemical Basis of Neuropharmacology*. London: Oxford University Press, 1996.

[165] O. A. Petroff, "GABA and glutamate in the human brain," *Neuroscientist,* vol. 8, pp. 562-573, 2002.

[166] A. Schousboe and H. S. Waagepetersen, "GABA: homeostatic and pharmacological aspects," *Progress in Brain Research,* vol. 160, pp. 9-19, 2007.

[167] (2014). *http://en.wikipedia.org/wiki/Gamma-Aminobutyric_acid*.

[168] M. Watanabe, K. Maemura, K. Kanbara, T. Tamayama, and H. Hayasaki, "GABA and GABA Receptors in the Central Nervous System and Other Organs," *International Review of Cytology,* vol. 213, pp. 1-47, 2002.

[169] K. Li and E. Xu, "The role and the mechanism of γ-aminobutyric acid during central nervous system development," *Neuroscience Bulletin,* vol. 24, pp. 195-200, 2008.

[170] J. Szabadics, C. Varga, G. Molnár, S. Oláh, P. Barzó, and G. Tamás, "Excitatory Effect of GABAergic Axo-Axonic Cells in Cortical Microcircuits," *Science,* vol. 311, pp. 233-235, 2006.

[171] H. M. Emrich, v. D. Zerssen, W. Kissling, H. J. Möller, and A. Windorfer, "Effect of sodium valproate on mania. The GABA-hypothesis of affective disorders.,"

Archives of Psychiatry and Neurological Sciences, vol. 229, pp. 1-16, 1980.

[172] F. Borsinia, A. Mancinelli, V. D'Aranno, S. Evangelista, and A. Meli, "On the role of endogenous GABA in the forced swimming test in rats," *Pharmacology Biochemistry and Behavior,* vol. 29, pp. 275-279, 1988.

[173] G. Tunnicliff and E. Malatynska, "Central GABAergic Systems and Depressive Illness," *Neurochemical Research,* vol. 28, pp. 965-976, 2003.

[174] J. W. C. Leung and H. Xue, "GABAergic Functions and Depression: From Classical Therapies to Herbal Medicine," *Current Drug Targets - CNS & Neurological Disorders,* vol. 2, pp. 363-374, 2003.

[175] A. V. Kalueff and D. J. Nutt, "ROLE OF GABA IN ANXIETY AND DEPRESSION," *DEPRESSION AND ANXIETY,* vol. 24, pp. 495-517, 2007.

[176] F. Petty, G. L. Kramer, M. Fulton, F. G. Moeller, and A. J. Rush, "Low Plasma GABA Is a Trait-Like Marker for Bipolar Illness," *Neuropsychopharmacology,* vol. 9, pp. 125-132, 1993.

[177] C. N. Epperson, R. Gueorguieva, K. A. Czarkowski, S. Stiklus, E. Sellers, J. H. Krystal, *et al.*, "Preliminary evidence of reduced occipital GABA concentrations in puerperal women: a 1H-MRS study," *Psychopharmacology,* vol. 186, pp. 425-433, 2006.

[178] S. Murai, H. Saito, H. Nagahama, H. Miyate, Y. Masuda, and T. Itoh, "Ultra-rapid assay of brain gamma-aminobutyric acid by liquid chromatography with electrochemical detection," *Journal of Chromatography,* vol. 497, pp. 363-366, 1989.

[179] P. Gamache, E. Ryan, C. Svendsen, K. Murayama, and I. N. Acworth, "Simultaneous measurement of monoamines, metabolites and amino acids in brain tissue and microdialysis perfusates," *Journal of Chromatography,* vol. 614, pp. 213-220, 1993.

[180] S. Smith and T. Sharp, "Measurement of GABA in rat brain microdialysates using o-phthaldialdehyde-sulphite derivatization and high-performance liquid chromatography with electrochemical detection," *Journal of Chromatography,* vol. 652, pp. 228-233, 1994.

[181] Y. Qu, L. Arckens, E. Vandenbussche, S Geeraerts, and F Vandesande, "Simultaneous determination of total and extracellular concentrations of the amino acid neurotransmitters in cat visual cortex by microbore liquid chromatography and electrochemical detection," *Journal of Chromatography A,* vol. 798, pp. 19-26, 1998.

[182] G. D. Frye and G. R. Breese, "GABAergic modulation of ethanol-induced motor impairment," *Journal of Pharmacology and Experimental Therapeutics,* vol. 223, pp. 750-756, 1982.

[183] L. A. Allison, G. S. Mayer, and R. E. Shoup, "The o-phthalaldehyde derivatives of amines for high-speed liquid chromatography/electrochemistry," *Analytical Chemistry,* vol. 56, pp. 1089-1096, 1984.

[184] P. Rada, S. Tucci, L. Teneud, X. Paez, J. Perez, G. Alba, *et al.*, "Monitoring γ-aminobutyric acid in human brain and plasma microdialysates using micellar electrokinetic chromatography and laser-induced fluorescence detection," *Journal of Chromatography B., Biomedical Sciences and Applications,* vol. 735, pp. 1-10, 1999.

[185] A. Zhou and J. Muthuswamy, "Acoustic biosensor for monitoring antibody immobilization and neurotransmitter GABA in real-time," *Sensors and Actuators B: Chemical,* vol. 101, pp. 8-19, 2004.

[186] A. J. Bard and L. R. Faulkner, *Electrochemical Methods: Fundamentals and Applications, 2nd Edition*. Oxford: Wiley, 2001.

[187] M. E. Orazem and B. Tribollet, *Electrochemical Impedance Spectroscopy*. Maitland: Wiley, 2011.

[188] J. S. Daniels and N. Pourmand, "Label-free impedance biosensors: opportunities and challenges," *Electroanalysis,* vol. 19, pp. 1239-1257, 2007.

[189] E. Katz and I. Willner, "Probing Biomolecular Interactions at Conductive and Semiconductive Surfaces by Impedance Spectroscopy: Routes to Impedimetric Immunosensors, DNA-Sensors, and Enzyme Biosensors," *Electroanalysis,* vol. 15, pp. 913-947, 2003.

[190] J. E. B. RANDLES, "KINETICS OF RAPID ELECTRODE REACTIONS," *Transactions of the Faraday Society,* vol. 1, pp. 11-19, 1947.

[191] B. Ershler, "Investigation of electrode reactions by the method of charging-curves and with the aid of alternating currents," *Discussions of the Faraday Society,* vol. 1, pp. 269-277, 1947.

[192] G. S. Wilson and R. Gifford, "Biosensors for real-time in vivo measurements," *Biosensors and Bioelectronics,* vol. 20, pp. 2388-2403, 2005.

[193] R. M. Wightman, P. Runnels, and K. Troyer, "Analysis of chemical dynamics in microenvironments," *Analytica Chimica Acta,* vol. 400, pp. 5-12, 1999.

[194] T. P. BOTHWELL and H. P. SCHWAN, "Electrical Properties of the Plasma Membrane of Erythrocytes at Low Frequencies," *Nature,* vol. 178, pp. 265-266, 1956.

[195] T. B. Jones, "Basic theory of dielectrophoresis and electrorotation," *Engineering in Medicine and Biology Magazine, IEEE,* vol. 22, pp. 33-42, 2003.

[196] K. Asami, T. Yonezawa, H. Wakamatsu, and N. Koyanagi, "Dielectric spectroscopy of biological cells," *Bioelectrochemistry and Bioenergetics,* vol. 40, pp. 141-145, 1996.

[197] L. L. Sohn, O. A. Saleh, G. R. Facer, A. J. Beavis, R. S. Allan, and D. A. Notterman, "Capacitance cytometry: measuring biological cells one by one," *Proceedings of the National Academy of Sciences of the United States of America,* vol. 20, pp. 10687-10690, 2000.

[198] Y. Qiu, R. Liao, and X. Zhang, "Impedance-Based Monitoring of Ongoing Cardiomyocyte Death Induced by Tumor Necrosis Factor-α," *Biophysical Journal,*

vol. 96, pp. 1985-1991, 2009.

[199] A. Caduff, F. Dewarrat, M. Talary, G. Stalder, L. Heinemann, and Y. Feldman, "Non-invasive glucose monitoring in patients with diabetes: A novel system based on impedance spectroscopy," *Biosensors and Bioelectronics,* vol. 22, pp. 598-604, 2006.

[200] C. M. A. Brett and A. M. O. Brett, *Electrochemistry: principles, methods and applications.* New York: Oxford University Press, 1993.

[201] M. Varshney, L. Yang, X.-L. Su, and Y. Li, "Magnetic Nanoparticle-Antibody Conjugates for the Separation of Escherichia coli O157:H7 in Ground Beef," *Journal of Food Protection,* vol. 68, pp. 1804-1811, 2005.

[202] M. Varshney, Y. Li, B. Srinivasan, and S. Tung, "A label-free, microfluidics and interdigitated array microelectrode-based impedance biosensor in combination with nanoparticles immunoseparation for detection of Escherichia coli O157:H7 in food samples," *Sensors and Actuators B: Chemical,* vol. 128, pp. 99-107, 2007.

[203] M. Sluyters-Rehbach, "Impedances of electrochemical systems: Terminology, nomenclature and representation - Part I: Cells with metal electrodes and liquid solutions (IUPAC Recommendations 1994)," *Pure and Applied Chemistry,* vol. 66, pp. 1831-1891, 1994.

[204] F. P. Zamborini and R. M. Crooks, "In-Situ Electrochemical Scanning Tunneling Microscopy (ECSTM) Study of Cyanide-Induced Corrosion of Naked and Hexadecyl Mercaptan-Passivated Au (111)," *Langmuir,* vol. 13, pp. 122-126, 1997.

[205] S. A. Piletsky, E. V. Piletskaya, T. A. Sergeyeva, T. L. Panasyuk, and A. V. El'skaya, "Molecularly imprinted self-assembled films with specificity to cholesterol," *Sensors and Actuators B: Chemical,* vol. 60, pp. 216-220, 1999.

[206] D. Graham and S. Dingman, "A Step-by-Step Guide for Solution Based Self-Assembly," *Material Matters,* vol. 1, pp. 18-19, 2006.

[207] D. Matatagui, J. Fontecha, M. J. Fernández, M. J. Oliver, J. Hernando-García, J. L. Sánchez-Rojas, *et al.*, "Comparison of two types of acoustic biosensors to detect immunoreactions:Love-wave sensor working in dynamic mode and QCM working in static mode," *Sensors and Actuators B: Chemical,* vol. 189, pp. 123-129, 2013.

[208] A. D. Chowdhury, R. Gangopadhyay, and A. De, "Highly sensitive electrochemical biosensor for glucose, DNA and protein using gold-polyaniline nanocomposites as a common matrix," *Sensors and Actuators B: Chemical,* vol. 190, pp. 348-356, 2014.

[209] J. Mok, M. N. Mindrinos, R. W. Davis, and M. Javanmard, "Digital microfluidic assay for protein detection," *Proceedings of the National Academy of Sciences of the United States of America,* vol. 111, pp. 2110-2115, 2014.